ABRASION-CORROSION AND STRESS CORROSION RESISTANCE OF A 9Cr-2Ni-0.7Mo STEEL IN SIMULATED MINE WATER

By

Gustav Ernest Gatzanis

A thesis submitted to the Faculty of Engineering, University of Cape Town in fulfilment of the degree of Master of Science in Engineering

Department of Materials Engineering
University of Cape Town

May 1991

ACKNOWLEDGEMENTS

I wish to express my appreciation to the following people who have assisted me during this research project:

My supervisor, Prof. A. Ball, for his advice and support.

Mrs. Helgard Böhm, Mrs. Sue Betz and Mrs. Penny Park-Ross for their assistance and co-operation in the laboratory and Miss Esmé Bergh for her typing assistance and moral support.

Mr. Nick Dreze and Mr. Glen Newins for their technical assistance. Mr. Bernard Greeves and Mr. James Peterson for the photographic work.

The CSIR and the Iron and Steel Corporation of South Africa are greatfully acknowledged for the provision of research bursaries and project support.

ABSTRACT

The locally (RSA) developed 9Cr-2Ni-0.7Mo steel designated 927 formed the subject of this study. Its abrasion-corrosion and stress corrosion performances were assessed in laboratory tests simulating the underground environment in South African gold mines. The results indicate that the alloy performs favourably in abrasive-corrosive applications, outperforming several other higher chromium containing steels which have been designed for the purpose. The alloy is also highly resistant to SCC at free corrosion potential in simulated mine water.

The good abrasion-corrosion resistance is attributed to the adequate corrosion resistance of the alloy acting in conjunction with the favourable combination of strength and toughness afforded the alloy by its fine grain size and microduplex microstructure of martensite and interlath retained austenite. The production variables of plate thickness and prior cold working were found to exert negligible influence on corrosion-abrasion resistance. This is ascribed to the small influence of these processes on the hardness and associated mechanical properties due the inherent low work hardening ability of the alloy.

Slow strain rate (SSR) stress corrosion cracking tests were performed on the alloy in four microstructural conditions viz. as-rolled, tempered, welded and post weld heat treated. The material showed an immunity to SCC in all the microstructural conditions for tests conducted at open circuit potential. This apparent immunity is attributed to the difficulty in initiating SCC by pitting on the plain specimens over the relatively short test durations.

Polarisation to extreme cathodic potentials (-1200mV) resulted in hydrogen embrittlement of this high strength alloy with failure predominantly along prior austenite grain boundaries. Anodic potentials in the excess of 0mV induced tunnel-like corrosion pitting attack. Fractographical evidence of SCC at the base of these pits indicates the development of the conditions necessary for SCC within the pit confines. This is cited as evidence in support of the hypothesis of SCC initiation difficulty.

NOTATION AND ABBREVIATIONS

AR	As-rolled
AR&T	As-rolled and tempered
AW	As-welded
bcc	body centered cubic
EAC	Environmentally assisted cracking
Ecorr	Free corrosion potential
HAC	Hydrogen assisted cracking
HAZ	Heat affected zone
HE	Hydrogen embrittlement
HV_{30}	Vickers hardness number (30kg load)
K_{ISCC}	Threshold stress intensity for SCC
MMA	Manual metal arc welding
ppm	parts per million
PWHT	Post weld heat treated
SCC	Stress corrosion cracking
SCE	Saturated calomel electrode
SEM	Scanning electron microscope
SSR	Slow strain rate testing
UTS	Ultimate tensile strength

CONTENTS

CHAPTER 1

GENERAL INTRODUCTION

1.1 BACKGROUND

The high cost associated with the deterioration of equipment under the action of the harsh abrasive-corrosive conditions prevalent in South African gold mines[1] together with the realisation of the lack of suitable corrosion-abrasion resistant alloys[2,3] prompted several alloy development programmes. The mechanisation of operations and handling systems in mines resulted in the increased demand for more reliable and durable materials of construction.

The requirements for a general purpose steel were defined as: resistance to corrosion and abrasion, sufficient toughness for structural applications, formability, weldability, machineability and flame cuttability[3]. The ideal material which fulfills these criteria must also be cost effective. Several different approaches were adopted by independent parties in an attempt to achieve these desired properties. These approaches included the development of a metastable austenitic[4,5], low carbon lath martensites[6,7] and modification of the duplex ferritic-martensitic 3CR12[8].

1.2 DEVELOPMENT OF 927

In order to ensure the cost competitiveness of the envisaged alloy, the developers adopted at the outset the rationale of reducing the manufacturing costs by producing an as-rolled steel requiring no further heat treatment[9]. The alloy formulation is similar to that proposed by Thomas et al[10-12], which consists of a micro-duplex microstructure of dislocated, fine lath martensite with thin films of interlath retained austenite, the essential difference being higher chromium content for increased corrosion resistance.

Initially a range of vacuum melts containing 0.1-0.3%C and 4-12%Cr together with a variety of elemental additions were produced. Four basic alloy classes were identified viz Cr-Ni, Cr-Mo, Cr-Mo-Cu and Cr-Ni-Mo. The results of corrosion and abrasion-corrosion tests performed on the four classes of laboratory vacuum melts yielded results comparing favourably with steels generally in use in the mines[9]. The test results also indicated that the 8-10% Cr-Ni-Mo group offered the best properties. On the basis of the abrasion and abrasion-corrosion performance and compromising as regards cost and the requirements for a steel for general use, a micro-alloyed 9Cr-2Ni-0.7Mo steel was produced in a 160 ton arc furnace melt, rolled and air cooled. The chemical composition of this alloy, designated 927, is given in Table 1.1. Typical mechanical

properties include a yield strength of 1000MPa, UTS of 1500MPa, elongation of 14%, hardness of $500HV_{30}$ and a Charpy impact toughness value (TL) of 60-80J at 20°C[9].

C	Cr	Ni	Mn	Mo	S	Al
0.16	8.88	2.01	0.62	0.68	0.002	0.019

TABLE 2.1 : The chemical composition of the alloy designated 927

1.3 THE OBJECTIVES AND STRUCTURE OF THE PROJECT

The acceptance and use of this newly developed alloy 927 by the mining industry demands :

i) characterisation and verification of the properties important to its application

ii) comparison of these with the properties of other alloys already in use.

These include mechanical, corrosion, abrasion-corrosion, fatigue, corrosion-fatigue and stress corrosion (K_{ISCC}) properties.

This thesis firstly establishes the good abrasion-corrosion characteristics and compares it to those of other alloys currently in use or intended for application in mining operations. The thesis then goes on to examine in detail the stress corrosion properties of the alloy in a typical mine water solution with a view to establishing:

i) The resistance of the as-rolled material to SCC in the mine water and the effect of individual ions identified as being aggressive.

ii) The influence of a tempering and a welding procedure on SCC resistance.

iii) The potential range of SCC susceptibility of the as rolled material in the simulated mine water solution.

iv) Insight into the SCC mechanisms operative at the various applied potentials.

CHAPTER 2

ABRASION-CORROSION PROPERTIES OF 927

2.1 INTRODUCTION

It was intended to assess the performance of 927 relative to that of alloys already in use or intended for application in the highly abrasive-corrosive conditions prevalent in South African gold mines. In addition to this, a need was identified to establish the effect of production variables i.e. plate thickness and degree of cold work as well as differing carbon and sulphur content on the corrosion and abrasion-corrosion properties.

2.2 MATERIALS

The chemical compositions of the variations of the 927 alloy used to investigate the effects of differing sulphur and carbon content on corrosion-abrasion properties are listed in Table 2.1. Also included in Table 2.1 for comparison purposes are the chemical compositions of several other corrosion-abrasion resistant development alloys intended for application in South African gold mines.

CHEMICAL COMPOSITION (WT%)							
STEEL	C	Cr	Ni	Mn	Mo	S	Al
927-A	0.15	9.05	2.36	0.70	0.83	0.0024	0.026
927-B	0.15	9.04	2.36	0.74	0.85	0.0170	0.095
927-C	0.17	9.18	2.32	0.69	0.84	0.0023	0.059
927-D	0.17	9.18	2.39	0.72	0.84	0.0110	0.066
12/10*	0.05	12.00	-	10.00	-	-	-
3CR12*	0.02	11.33	0.62	1.14	-	-	-
304L*	0.04	18.80	8.40	1.38	0.11	-	-
Abrasalloy*	0.39	0.34	0.60	0.85	0.16	0.0180	0.040
Wearalloy 400*	0.21	0.02	0.03	0.97	0.01	-	-

Table 2.1: Composition of the standard 927 alloy and the alloy variants used to investigate the effects of differing carbon and sulphur content on the corrosion-abrasion properties. Also shown in the Table are the chemical compositions of several other corrosion-abrasion resistant alloys intended for application in SA gold mines. These are demarcated with an * and are quoted from Reference 13.

2.3 EXPERIMENTAL METHODS

A laboratory dry abrasion and an intermittent abrasion plus corrosion test have been developed which rank materials in the same order and produce similar wear morphlogy to an in situ test conducted on a rock conveyor[14]. The dry abrasion test is performed on a pin-on-belt abrasion testing machine. The specimens (10×10×25mm) are abraded end-on on a bonded 80 grit abrasive belt under a load of 32.1N and a velocity of 0.260 ms^{-1}. The test rig is so designed that the specimen always abrades against unworn particles. The specimens are initially run in, cleaned ultrasonically, dried and weighed to an accuracy of 0.01mg. The specimens are then abraded, cleaned and weighed at the end of each 3m abrasion cycle for a total path length of 12m. The relative dry abrasion resistance or RAR is then computed as the ratio of material loss between normalised mild steel 070M20 and the material.

For the abrasion-corrosion test identical specimens are run in on the abrasion rig, weighed to 0.01mg, coated on the five unabraded sides with a lacquer and mounted with the abraded surface flush with a perspex test plate. The plate is set at an angle of 30° and synthetic mine water maintained at 30°C, is circulated over it. The simulated mine water comprises of 345ppm sulphate and 175ppm chloride at a pH of 6.8. At intervals the specimens are removed from the rig, cleaned of lacquer and oxide product by ultrasonic agitation in a buffered mild acid solution and the corrosion weight loss determined. The specimens are then abraded a short distance, cleaned, re-weighed and replaced into the corrosion rig. This corrosion-abrasion procedure is repeated for four cycles. The Relative Wear Resistance Laboratory (RWRL) is then computed as the ratio of total volume loss of mild steel to that of the material under investigation.

Two versions of the test have been devised which differ in terms of the duration and extent of corrosion and abrasion cycles of the test. The RWRL#1 test involves four cycles of 0.25m abrasion and 46 hours corrosion whereas the RWRL#2 test involves four cycles of 1m abrasion and 22 hours corrosion. The two tests thus place different emphasis on the abrasion and corrosion properties of a material. The RWRL#1 test with its longer corrosion time and shorter abrasion path length places more emphasis on the corrosion properties of a material. The converse is true for the RWRL#2 test.

In addition to the above-mentioned standard test, another test was conducted in which several identical specimens were prepared as for the corrosion-abrasion tests and placed in the corrosion rig. At intervals over a period of two weeks, a specimen was removed and the volume loss determined.

MATERIAL	HARDNESS (HV_{30})	RAR	RWRL#1	RWRL#2	MICROSTRUCTURE
927	490	1.55	10.45	2.59	M + A
12/10	225	1.71	12.00	5.00	A
3CR12	153	1.03	7.4	2.00	F + M
304L	206	1.29	11.00	2.90	A
Abrasalloy	436	1.36	1.06	1.21	M
Wearalloy 400	406	1.34	1.36	-	M

Table 2.2: Abrasion and abrasion-corrosion wear indices of 927 and other prospective corrosion-abrasion resistant alloys[13]. The chemical composition the alloys are given in Table 2.1.

M = martensite ; A = austenite ; F = ferrite

2.4 RESULTS

The average of the test results for the dry abrasion tests (RAR), low frequency laboratory corrosion-abrasion tests (RWRL#1) and the high frequency (RWRL#2) tests are shown in Table 2.2. Also shown in the Table for comparison purposes are the wear indices for several other alloys intended for corrosive-abrasive applications.

Both the relative dry abrasion performance (RAR) and the corrosion-abrasion performance (RWRL#1 and 2) compare extremely favourably with the other development alloys included in the corrosion-abrasion test programme as illustrated by Figures 2.1 and 2.2.

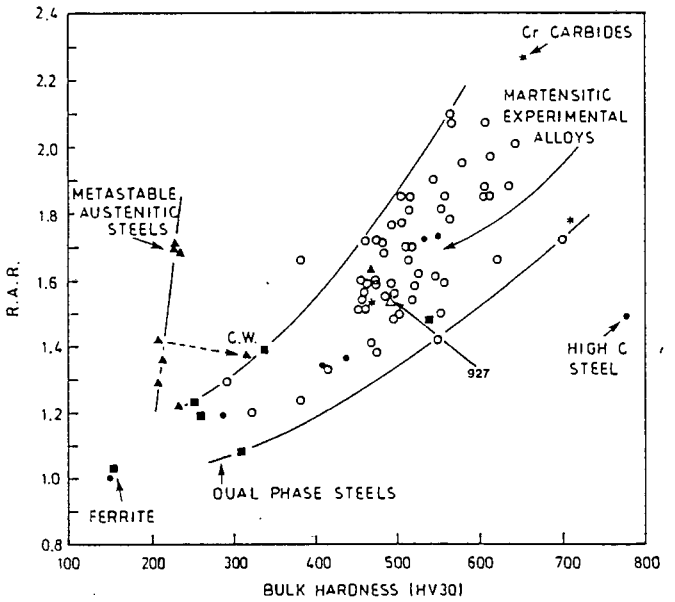

Figure 2.1: Relationship between the relative dry abrasion resistance (RAR) and bulk hardness[13]. The position of 927 is indicated.

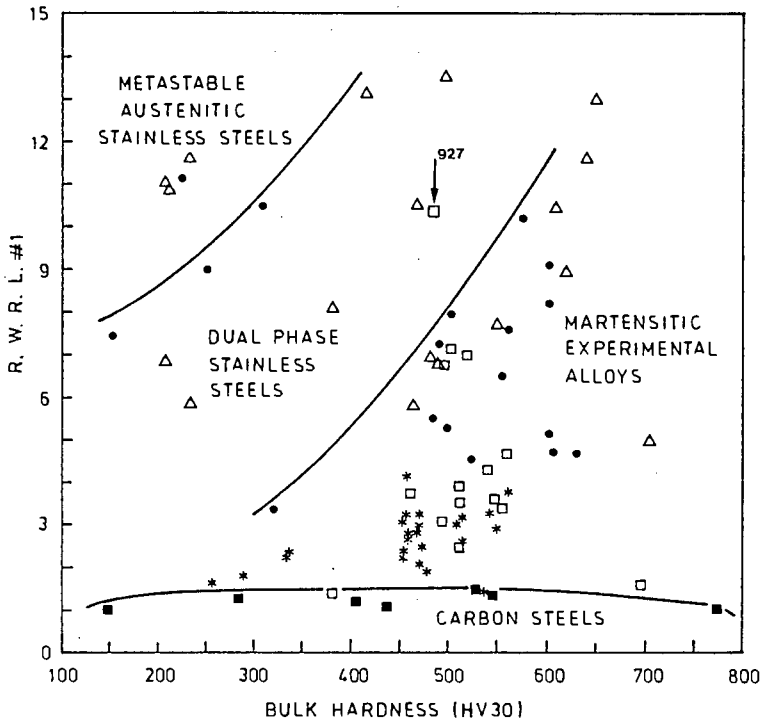

Figure 2.2: Relative wear resistance (RWRL#1) as a function of bulk hardness for the four groups of steels containing increasing amounts of chromium [13]. The position of 927 is indicated.

2.4.1 Dry Abrasion

Scanning electron microscopy of the dry abraded 927 surfaces revealed very shallow, thin, straight and clean wear tracks with very thin side ridges relative to the mild steel reference as illustrated by Figure 2.3. The thinness of the side ridges is related to the limited ductility of the material and is symptomatic of the dominance of the cutting process in the abrasion of these type of materials.

Tapered sections through the abraded surface revealed a small (2 - 5%) difference in hardness between the bulk and the abraded surface. This is a reflection of the low work hardening ability and limited ductility of the material.

2.4.2 Corrosion-abrasion Testing

Corrosion-abrasion indices compare well with those of higher (12%) chromium containing steels like 12/10 and 3CR12. The alloy undergoes small corrosion volume losses in both the RWRL#1 and RWRL#2 tests, being in the range 4 - 10% and 2 - 5% of the total volume loss respectively. In the plot of Figure 2.4 comparing the corrosion volume loss as a function of chromium content for the different development alloys, 927 can be seen to have experienced a small but similar corrosion

volume loss to that of some of the higher chromium containing alloys. However, with its chromium content of 9%, the alloy is in the critical region with respect to the chromium content for sustained passivity in the simulated mine water solution. It is of course recognised that the rate of corrosion volume loss will not be influenced by the chromium content alone, but also by other alloying additions. In the case of 927, by the positive influence of the 0.7% molybdenum and 2% nickel additions on pitting resistance.

(a) (b)

Figure 2.3: The wear surfaces after dry abrasion; (a) - mild steel 070M20; (b) - alloy 927. Alloy 927 exhibits clean, shallow wear tracks with thin side ridges relative to the mild steel standard.

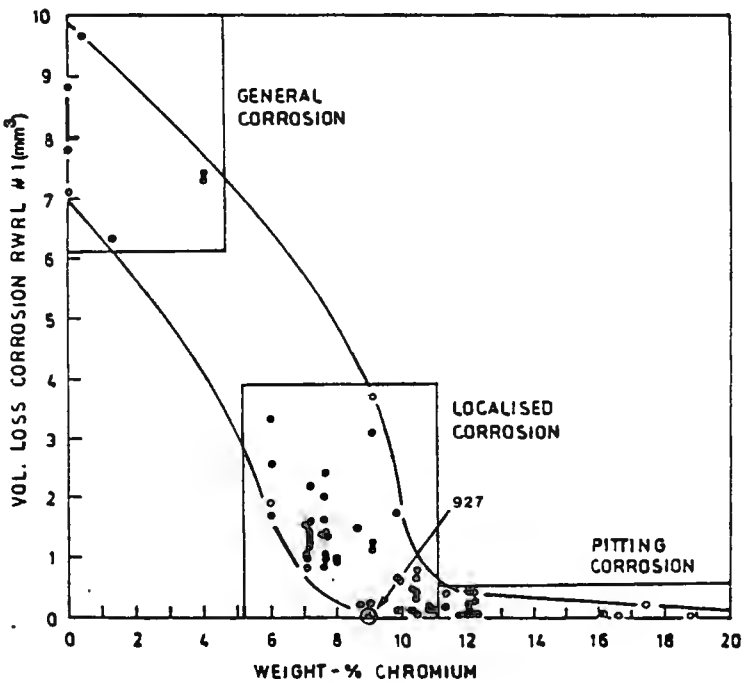

Figure 2.4: Volume loss by corrosion of an abraded surface under (RWRL#1) test conditions as a function of chromium content [13]. Three types of corrosion are indicated. The position of 927 on the plot is indicated.

Figure 2.5: The alloy on the verge of breaking down with very small corrosion pits forming in wear tracks.

Visual examination of the abraded-corroded surface after 46 hours corrosion revealed trails of a reddish-brown corrosion product on the surface eminating largely from several well developed pits. Subsequent SEM examination of the abraded-corroded surface showed that the corrosion product was randomly distributed on the abraded surface, occurring both in the bottom of wear tracks and along ridges. Removal of this corrosion product by ultrasonic agitation in a buffered mild acid solution and subsequent examination with the SEM disclosed the existence of numerous small corrosion pits in the bottom of wear tracks (Figure 2.5) and the occasional well developed pit (Figure 2.6). The inherent chemical stability and mechanical strength of the oxide film became apparent by the difficulty in removing the film by ultrasonic agitation in the mild acid solution. In comparison, the removal of the oxide film on steels containing 9% chromium but no nickel or molybdenum was relatively easy.

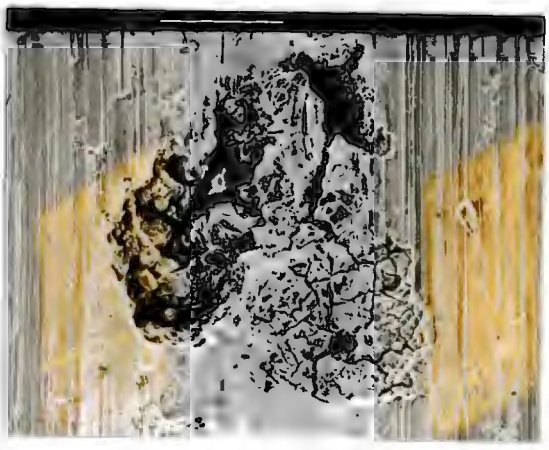

Figure 2.6: Typical example of a well developed pit which was randomly found on the surfaces of several specimens.

2.4.3 The Effect of Production Variables on Abrasion and Abrasion-Corrosion Properties

Once initial tests had proved the feasibility of 927 for corrosive-abrasive applications, a need was identified for investigating the effect of production variables like plate thickness and prior cold working (caused by subsequent forming operations) on abrasive and abrasive-corrosive properties.

2.4.3.1 Plate Thickness

The results of the RAR, RWRL#1 and RWRL#2 tests as a function of plate thickness are presented in Table 2.3 together with the bulk hardness values (Vickers 30kg) measured on the rolled plate surfaces. The results of the tests are presented graphically in Figure 2.7 together with a hardness plot.

There is no significant influence of production plate thickness on either the dry abrasion or corrosion-abrasion performance. It is also evident from Figure 2.7 that the hardness decreases only marginally with increasing plate thickness, exhibiting a 10% decrease in hardness from the thinnest to the thickest plate. SEM examination also failed to highlight any difference between the appearance of the abraded and abraded-corroded surfaces of the various plate thickness samples.

PLT. THK (mm)	HARDNESS (HV_{30})	RAR	RWRL#1	WT % CORR.	RWRL#2	WT % CORR.
M.S.	194	1.00	1.00	90.0	1.00	42.7
6	487	1.56	15.23	3.8	2.71	1.6
8	478	1.50	14.92	4.5	2.56	6.8
10	467	1.50	14.67	9.1	2.70	2.4
17	449	1.58	13.45	0.0	3.08	3.2
25	441	1.57	13.23	6.6	2.78	2.1

Table 2.3: The abrasion and abrasion-corrosion wear indices as a function of plate thickness. Also shown in the Table is the percentage of total volume loss attributed to corrosion in the RWRL#1 and RWRL#2 tests.

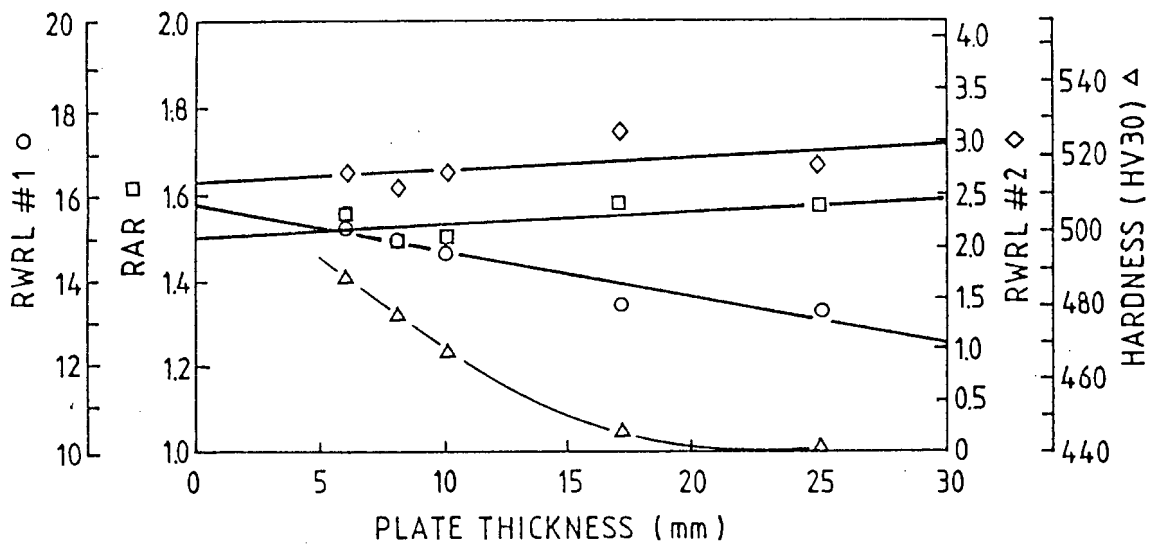

Figure 2.7: A plot of the abrasion and abrasion-corrosion wear indices and hardness as a function of plate thickness.

2.4.3.2 Cold work

Strain hardening can be defined as an increase in the hardness and strength caused by plastic deformation at temperatures below the recrystallisation temperature. Cold work is the operation of producing such deformation and resulting permanent strain. The different degrees of cold working were achieved by cold reducing of the 25mm plate.

The RAR, RWRL#1 and RWRL#2 wear indices are presented in Table 2.4 together with the hardness values and are represented graphically in Figure 2.8. Although there is a $100HV_{30}$ (20%) hardness difference between undeformed and maximum deformed (57%) samples, the degree of prior cold work is seen to exert negligible influence on dry abrasion and abrasion-corrosion properties. Cold working is reputed to increase the corrosion kinetics but no detectable influence was found in this examination either by difference in corrosion volume losses or appearance of the corrosion surface under the SEM (ie. morphology and distribition of pits).

% COLD WK	HARDNESS (HV_{30})	RAR	RWRL#1	WT % CORR.	RWRL#2	WT % CORR.
M.S.	194	1.00	1.00	88.3	1.00	41.1
0	490	1.63	10.44	10.7	2.45	2.0
7	473	1.59	10.21	9.6	2.34	2.7
20	511	1.52	10.82	7.4	2.44	1.6
21	-	1.56	10.63	5.5	2.73	2.0
29	550	1.56	10.63	9.1	2.73	2.0
43	558	1.52	9.74	10.0	2.75	1.5
48	583	1.48	11.03	5.7	2.80	1.6
57	585	1.64	10.08	3.5	2.75	1.2

Table 2.4: The abrasion and abrasion-corrosion wear indices as a function of prior cold working. Also shown in the Table are the percentage volume losses attributed to corrosion in the RWRL#1 and RWRL#2 tests.

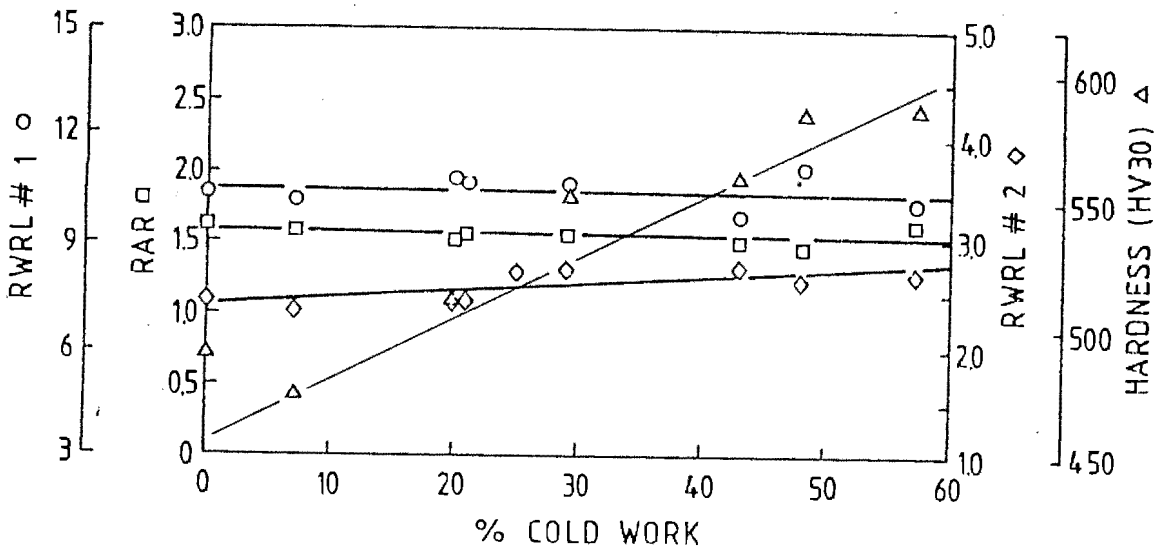

Figure 2.8: Abrasion and abrasion-corrosion indices as a function of prior cold working.

2.4.3.3 Influence of Carbon and Sulphur Content

Four different 927 samples containing variations in carbon and sulphur content (Table 2.1) were tested for the influence of these constituents on the wear performance. These experimental alloys were produced as 2kg vacuum induction melts. The detrimental effect of sulphur on corrosion resistance by the preferred initiation of pits at manganese sulphide inclusions is well documented. Consequently, one might anticipate poorer abrasion-corrosion performance by the higher sulphur containing alloys, especially in the RWRL#1 test with its longer corrosion period. This expectation was not borne out by the test results as corrosion volume losses in the RWRL#1 and RWRL#2 tests did not differ significantly between the lower and higher sulphur containing samples as shown in Table 2.5. This was confirmed by SEM examination of the abraded-corroded surfaces which failed to reveal any higher incidence of corrosion pits in the higher sulphur containing samples.

ALLOY	CARBON (WT %)	SULPHUR (WT %)	RAR	RWRL#1	WT % CORR.	RWRL#2	WT % CORR.
927-5	0.15	0.0024	1.48	6.84	15.22	2.05	9.46
927-6	0.15	0.0170	1.37	6.00	10.48	2.29	8.02
927-7	0.17	0.0023	1.44	7.07	11.24	2.49	4.35
927-8	0.17	0.0110	1.51	8.28	11.84	2.26	6.21

Table 2.5: The abrasion-corrosion indices of the 927 alloys with differing carbon and sulphur contents.

2.5 DISCUSSION

Zum-Gahr[15] identified the properties of a material influencing abrasive wear as yield strength under restraint or hardness, work hardening, ductility, crystal anisotropy and mechanical instability. This is because resistance to elastic/plastic strain or hardness together with work hardening determine the contact area between an abrasive particle and the material.

It is important to realise that during abrasion, material deformation and eventually fracture occurs at very localised areas under conditions of high hydrostatic pressure (leading to high surface strains) and high strain rates. Thus material properties that can delay the early satisfaction of fracture criteria e.g. increased ductility or strain accommodating ability (as often described by the strain hardening exponent), increased macro and micro toughness or properties that reduce the amount of material removed or cold worked e.g. high hardness, will improve the abrasion performance of a material.

One would expect 927 with its almost exclusively martensitic microstructure with thin film of retained austenite around laths[9] and its associated high dislocation densities (Honeycombe[16] reports initial dislocation densities for lath martensite of 10^{11} to 10^{12} cm^{-2}) are likely to afford the material little strain hardening ability. The strain hardening exponent derived from a tensile test is given in Table 2.6 together with those of other development alloys. Although 927 has a low strain hardening exponent and hence low fracture strain, this detrimental influence is offset by the high yield and tensile strengths. This coupled with the reduction in abrasive penetration owing to the high hardness means that less material will be removed during abrasion. Also the thin layer of inter lath retained austenite is thought to be a major contributor to high toughness of the alloy (Charpy (TL) = 80-90J at 20°C) and is thus likely to play an important role in reducing the frequency of surface fracture events in comparison with a fully martensitic structure.

MATERIAL	STRAIN HARDENING EXPONENT	MICROSTRUCTURE
927	0.13	Martensitic
AISI 304*	0.50	Austenitic
3CR12*	0.17	Ferritic/Martensitic

* = Reference 17

Table 2.6: Strain hardening exponent of 927 and two other alloys intended for abrasion-corrosion applications.

The alloy passivates in the simulated mine water solution and exhibits similarly small corrosion volume losses to the higher 12% chromium containing steels like 3CR12 and 12/10, despite its nominal chromium content of 9%. These good corrosion properties are linked to the effect of the 2% Ni and especially the 0.7% Mo on suppressing pitting tendencies[9,18]. The good dry abrasion properties coupled with the low corrosion volume losses in the RWRL#1 and RWRL#2 (46 hours and 22 hours corrosion respectively) yields very good corrosion-abrasion indices. These indices are comparable with those of the higher chromium containing steels and in some instances better. Tests performed on the alloy using a more aggressive mine water solution and corrosion periods of five days resulted in the production of a thin, black oxide layer. This oxide layer was found to be chemically stable and robust, properties which are highly desirable for corrosive-abrasive applications.

The existence of numerous small pits in the bottom of wear tracks after 46 hours exposure in the RWRL#1 test (Figure 2.5) indicates that the passivity is in the process of breaking down. The plot of corrosion rate versus time of Figure 2.9 shows that the corrosion rate virtually doubles after 80 hours. This serves to illustrate that corrosion exposure in the excess of the period used in the RWRL#1 test will lead to a significant corrosion contribution to volume loss and considerably poorer abrasion-corrosion performance relative to the higher chromium containing steels. Barker and Ball[18] illustrated that steels with 8-10% chromium are borderline with respect to adequate corrosion protection in mining environments.

Three categories of corrosion behaviour at an abraded surface were identified as illustrated in Figure 2.11[19]. The first is displayed by low alloy steels which exhibit general corrosion immediately after abrasion and have no induction period (Type I). Type II steels have a short induction period prior to localised corrosion. The highly alloyed stainless steels occupy Type III behaviour and passivate rapidly, exhibiting a long induction period and lose little material other than by pitting corrosion. It is argued that if the frequency of corrosive-abrasive cycles is such that the corrosive activity is interrupted before the induction period of breakdown, then the material will perform well in abrasive-corrosive conditions.

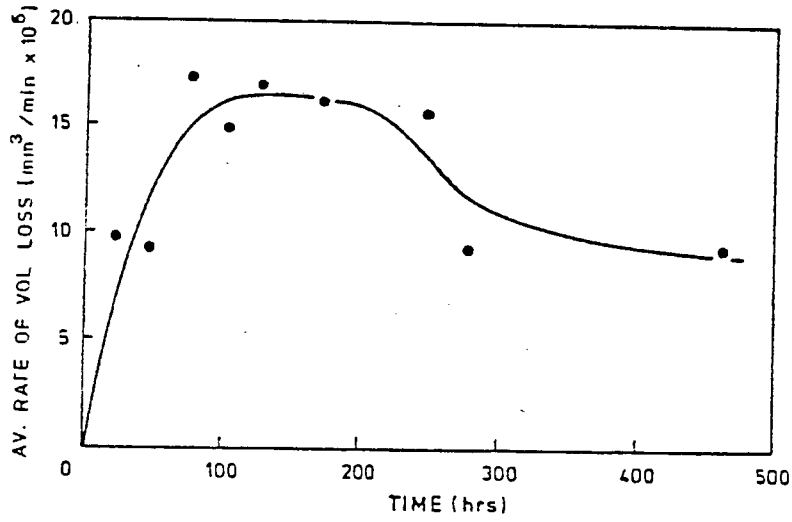

Figure 2.9: Rate of corrosion volume loss as a function of time for 927.

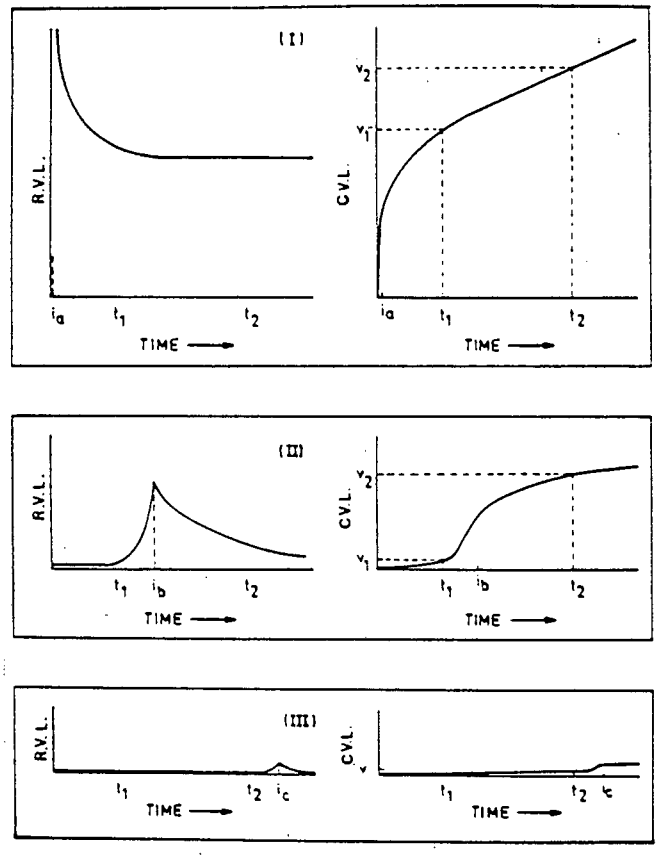

Figure 2.10: Schematic representation of the rate of volume loss (RVL) by corrosion and cumulative volume loss (CVL) as a function of time for the three types of steel in the abraded condition[13].

The alloy 927 falls into category II and evidence is such that the time period of the RWRL#1 test (46 hours corrosion) is marginally short of the induction period for breakdown. If the corrosion-abrasion frequency was further reduced, the performance of alloy 927 relative to the higher chromium containing abrasive-corrosive resistant alloys would depreciate.

The apparent non-effect of plate thickness on dry abrasion properties is linked to the negligible influence of as-finished plate thickness on mechanical properties. This is reflected by the small (10% change) in bulk hardness between the 6 and 25mm plate. The abrasion-corrosion trend essentially follows that of the dry abrasion because of the small contribution of corrosion to volume loss in both the RWRL#1 and RWRL#2 corrosion-abrasion tests.

Intuitively one would expect prior cold work to exert an influence on dry abrasion resistance because the work hardening of the surface is inherent in the abrasion process. The effect of cold work is to increase the hardness and decrease the ductility of the material. The dilemma is essentially whether the positive effects of increased hardness and strength on the abrasion resisting properties of the material are offset by the decrease in ductility and associated macro and micro toughness.

Barker and Ball[19] report that a 30% increase in hardness produced a 10% decrease in the RAR of mild steel. This is related to the marked effect of cold work on the macro and micro mechanical properties of mild steel and hence on abrasion resistance. In the case of the 927 alloy, the RAR remains essentially uneffected by cold work, although there is a 20% hardness difference between underformed and 57% deformed material. This is again explained in terms of the limited work hardening ability of the martensitic microstructure of the alloy and the associated small influence of prior cold working on the micro and macro properties of the material relevant to abrasion. Again, minimal corrosion volume loss in the corrosion-abrasion test means that these trends essentially follow the dry abrasion trends.

Overall, the differences in carbon and sulphur content as shown in Table 2.1 are not large enough to exert a significant influence on corrosion-abrasion behaviour. If one corroded for longer periods than 46 hours, differences in sulphur content may become significant. Barker[13] reports that although increasing the carbon content leads to an increase in hardness (interstitial hardening) and a general increase in RAR, the relationship between RAR and percentage carbon is not very strong for the alloyed martensitic steels. High levels of carbon also result in the increased likelihood of an adverse affect on the corrosion resistance via sensitisation and hence on abrasion-corrosion performance.

In conclusion it can be said that since during abrasion-corrosion, a corrosion effect is superimposed on a mechanical abrasion process, the resistance to this form of attack is determined by a balance

by a balance of properties that enhance resistance to corrosion and ones which enhance resistance to abrasion. In the case of 927, the former is provided by the chromium, nickel and molybdenum additions which result in a mechanically robust and chemically stable oxide film on the alloy surface. The latter is provided by the favourable combination of high hardness and toughness afforded the alloy by its microduplex martensitic/ferritic microstructure.

CHAPTER 3

LITERATURE REVIEW - STRESS CORROSION CRACKING

3.1 INTRODUCTION

Stress corrosion cracking (SCC) is a time-dependent process in which a metallurgically susceptible material fractures due to the synergistic interaction of a corrosive environment and sustained tensile stresses at the metal surfaces. SCC is one of the generic names of several environment-load synergistic failures which are collectively described under the name Environmental Assisted Cracking (EAC). The essential difference between the various components lies in the differences in the two contributing factors to the process viz. load and environment. EAC is usually separated into stress corrosion cracking when the stresses are nominally static and corrosion fatigue when the stresses fluctuate. If the embrittling species happens to be hydrogen, then it is often referred to as hydrogen embrittlement (HE) or hydrogen assisted cracking (HAC), depending on the degree of contribution of the hydrogen to the cracking process.

The disturbing factor of this phenomenom to designers in the engineering community is that the fracture occurs after slow, often insidious crack growth at stress intensities markedly below those associated with fast fracture in the absence of the environmental influence. All SCC failures have in common a macroscopic appearance of brittleness; in the engineering sense the ductility is impaired, but the degree to which they involve microscopic cleavage or inherent brittleness remains unclear. The provision of a valid environmental parameter for design purposes is virtually impossible because of the compositional, mechanical and metallurgical synergism and the consequent need to consider a range of environmental variables as well as their variations with time and their interactions with loading and metallurgical variables[21].

3.2 INITIATION

Stress corrosion crack initiation processes usually involve the development of an occluded cell with the associated acidification and concentration of the causative species[21,22] The principle factors involved in the initiation and propagation of SCC cracks are illustrated schematically for an austenitic stainless steel in Figure 3.1. The development of an occluded cell is assured in materials that undergo localized corrosion in the form of pitting.

Film rupture by slip is an alternative mechanical means for initiating localized corrosion that takes the form of corrosion trenches. This then leads to the occluded cell arrangement[21].

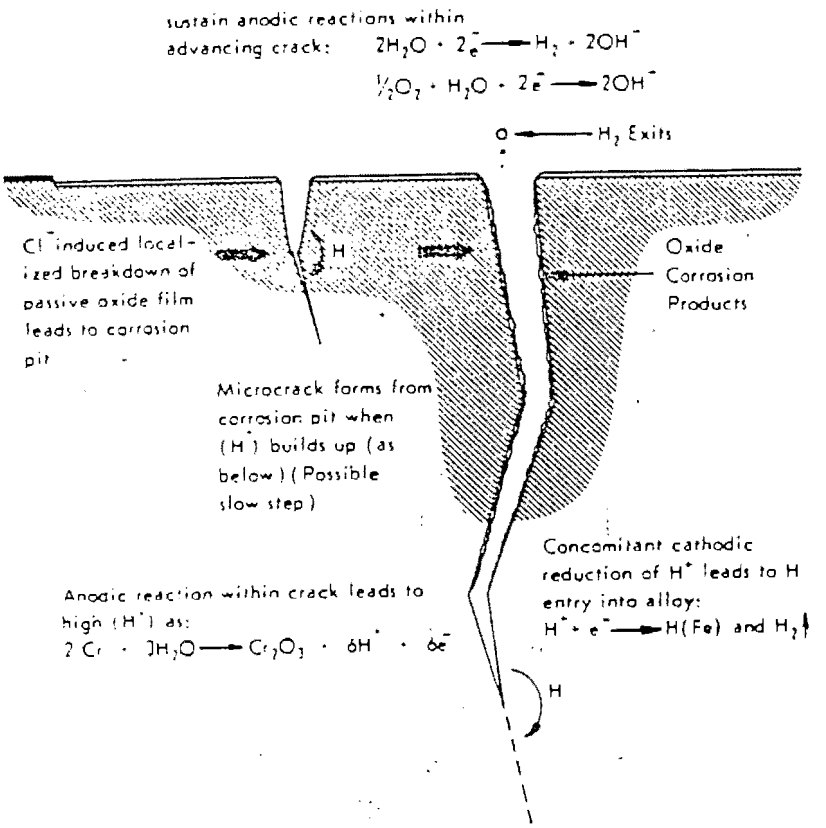

Figure 3.1: Schematic representation of the principal factors involved in the initiation and propagation of stress corrosion cracks in austenitic stainless steels[22].

Another instance where EAC is not initiated at pits is related to the ingress of hydrogen into the metal. This often occurs at potentials below the pitting potential or when crack growth occurs by a dissolution-controlled process involving a metal and an environment that do not display pitting[23]. When a crevice or some other geometrical discontinuity exists in a structure exposed to a potent environment, a local breakdown of surface film followed by reactions that promote the formation of a pit are no longer necessary precursors of changes in environmental composition. Consequently those components of pitting reactions associated with localized changes in environment will occur at lower potentials in the presence of pre-existing surface defects than are required for the pitting of initially plain surfaces[23].

3.3 PROPAGATION

When stress corrosion crack propagation rate is determined and plotted as a function of stress intensity (K_I), the test results of a highly susceptible material exhibit a general trend as shown in Figure 3.2(a). The response to the conjoint actions of stress intensity and chemical driving forces is given by the steady state crack growth rate da/dt. The shape of the curve and the absolute growth rates are a complex function of several mechanical and environmental parameters[24].

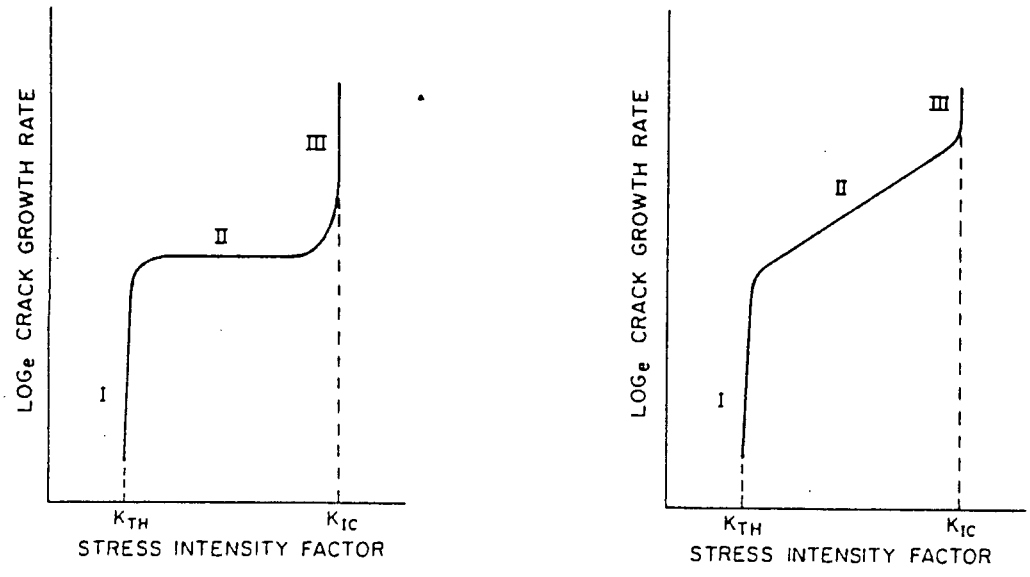

Figure 3.2: Generalised kinetics of stress corrosion cracking; (a) K_1-independent stage II; (b) K_1-dependent stage II behaviour[21].

The steady-state crack growth has been characterised into three distinct regions. The three regions consist of two strongly K_I-dependent stages (stages I and III) joined by a K_I-independent (Figure 3.2(a)) or K_I-dependent (Figure 3.2(b)) intermediate stage (stage II).

Two aspects of the stress corrosion velocity curve exert a major influence on the time to failure i.e. the crack velocity in region II and the slope of the curve in region I. The position of K_{ISCC} or K_{TH} (threshold stress intensity for the onset of SCC) on this curve will determine the duration of Region I and hence the onset of Region II crack velocity and thereby exert a strong influence on the time to failure. It is possible for Region I to be absent and K_{ISCC} to be situated in Region II and thus once K_{ISCC} is exceeded, cracking will proceed at a rate determined by a velocity of crack growth in Region II. Thus is typical for low alloy steels[25].

3.4 ENVIRONMENT

3.4.1 Mechanical

3.4.1.1 Load

Two schools of thought exist on the role of load or stress in stress corrosion cracks[26]:

i) rupture of films at crack tips

ii) opening of cracks to allow fresh solution to the crack tip where anodic dissolution is concentrated.

The influence of stress on SCC is usually portrayed in terms of either time to failure against initial stress or of crack velocity against stress intensity, whereby threshold stresses or stress intensities below which failure does not occur can be defined[27]. The implication that stress or stress intensity factor, quantities useful in engineering design, are of direct significance to EAC modes of failure may not be correct. There is an increasing amount of evidence that mechanistically it is the strain rate or creep in the crack tip region that is important rather than the stress intensity, although clearly strain rate derives from the presence of the stress[28]. Thus the effect of load on SCC is not directly as a result of the stress it generates but rather as a result of the strain or creep that is produces at the crack tip.

This phenomenology of strain rate effects in environment sensitive fracture has been demonstrated for a wide variety of combinations of metals and environments[29]. It is important both in systems which involve dissolution and film rupture and in systems which involve hydrogen entry into the steel. In the former it influences activity at the crack by providing the exposure of metal at the emerging slip steps to sustain dissolution while in the latter it causes disruption of films to allow hydrogen entry into the metal. There are also indications that the creep at the crack tip assists with the transportation of hydrogen once it is absorbed into the lattice via dislocations involving Cotterell atmospheres[28]. Parkins has produced a comprehensive review of strain rate effects in SCC[30].

3.4.1.2 Load Pattern and Form

There is increasing evidence that cyclic loading superimposed on a high statically loaded SCC specimen greatly accelerates SCC. This has been attributed to the effect of cyclic load on the crack tip strain or creep. Evans and Parkins[31] observed that cyclic loading in air extends the ambient temperature plastic deformation in manganese steel beyond the primary creep stage observed under constant load. Figure 3.3 shows that after primary creep had been exhausted under constant load, the strain (creep) rates increased markedly when a cyclic load was superimposed. Thus for many systems it is now recognised that SCC and corrosion fatigue are a continuum, with crack tip strain rate as the underlying mechanical variable[32].

It is also found that the severity of corrosion fatigue (or creep at the crack tip) is influenced by wave-shape of the applied load[33]. It is found than any waveform involving finite rise time of stress i.e. slow-fast, triangular or sinusoidal, accelerates corrosion fatigue. The effect must be metallurgical since the degrading effect of a slow-fast waveform is observed even in a vacuum.

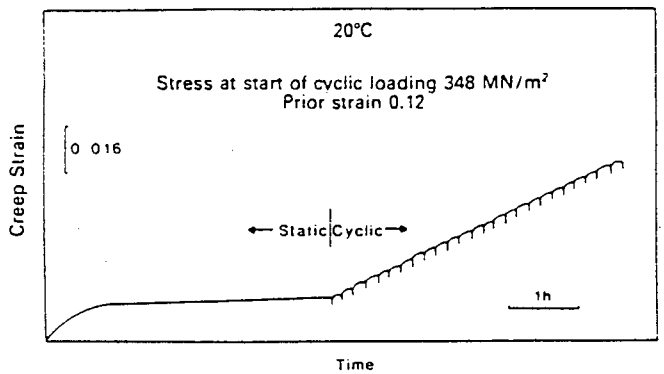

Figure 3.3: The effect of cylic load on the creep of C-Mn steel[31].

3.4.2 Chemical

3.4.2.1 Introduction

Whilst the concept of solution specifity remains, in the sense that not all environments corrosive towards a particular metal will promote SCC, nevertheless the number of environments that are potent towards a particular alloy continue to increase with time as research sheds more light[34]. Procter and Newman[26], in their review of stress corrosion cracking from 1965 - 1990, cite the recognition of the lack of specifity of SCC environments as one of the major developments over this period. The highly specific nature of solution composition requirements for crack growth by dissolution-controlled mechanisms are not so rigid in relation to crack growth resulting from the ingress of hydrogen into the metal. In the latter case the primary requirement is that the environment provides a source of hydrogen that is released by appropriate electrochemical conditions.

The physical aspects of environment e.g. flow are probably significant only to the extent that they influence the transport of species to and from the surface. Geometry, like flow is a secondary variable since it influences environmental composition and stress on a local scale[35].

3.4.2.2 Electrochemical Considerations

Much of the evidence in literature indicates that SCC only occurs within a finite range of potentials, which is typically of the order of a few hundred millivolts in most systems[28]. Staehle[36] proposed a diagram (Figure 3.4) which illustrates the SCC susceptibility as a function of potential and its attendant affect on film stability. The range of potentials may be determined in some systems by filming reactions, but in others it may be related to local galvanic effects associated with segregates or precipitation in grain boundaries. Stress corrosion cracking requires

a critical balance between active and passive behaviour, since gross activity is likely to promote general, rather than localised dissolution and passivity will by definition not be associated with any corrosion[34].

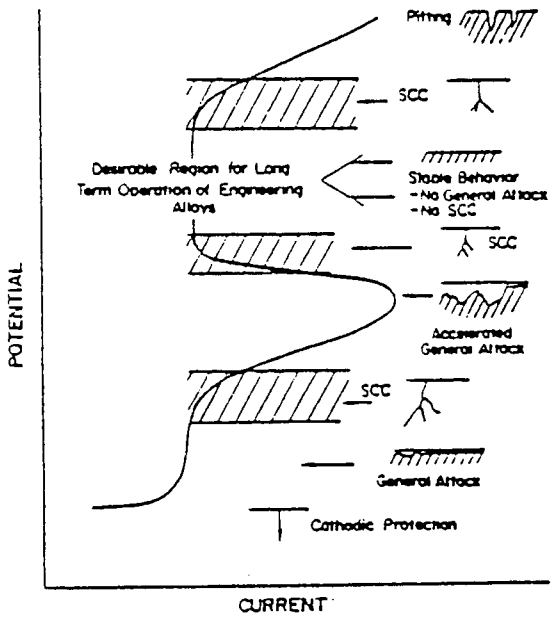

Figure 3.4: Schematic array of corrosion morphologies associated with various electrochemical potentials. This correlation does not occur in all cases but is widely enough observed to be generally regarded as an indication of trends[36].

At potentials noble to Ecorr metal dissolution is dominant, whilst at more active potentials dissolution is suppressed and it is necessary to consider possible cathodic reactions. Two competing reactions are of interest viz. hydrogen discharge and oxygen reduction. The former is favoured by low pH and relatively active potentials and the latter by neutral and higher pH's, high oxygen concentrations in solution and relatively noble potentials. At intermediate potentials for both systems ambiguity exists as to which mechanism of crack growth is operative and Parkins[38] draws the conclusion that both hydrogen induced and dissolution controlled cracking can occur in these circumstances. The possible reactions at the crack tip are summarised in Figure 3.5.

Correlation of SCC with steady state and transient electrochemistry has been a major area of research, especially amongst workers convinced of the dominance of anodic reactions in crack propagation. Experimental approaches to the definition of potential cracking conditions can be by potentiodynamic polarisation curves[28,38], current decay measurements at constant potential or especially where surface films are difficult to reduce electrolytically by straining or scraping

electrode experiments devised by Hoar and co-workers[39]. Hoar[40] demonstrated a reasonable correlation of anodic dissolution kinetics in rapidly strained electrodes with crack velocities using Faradays second law for austenitic stainless steels in hot $MgCl_2$ solutions.

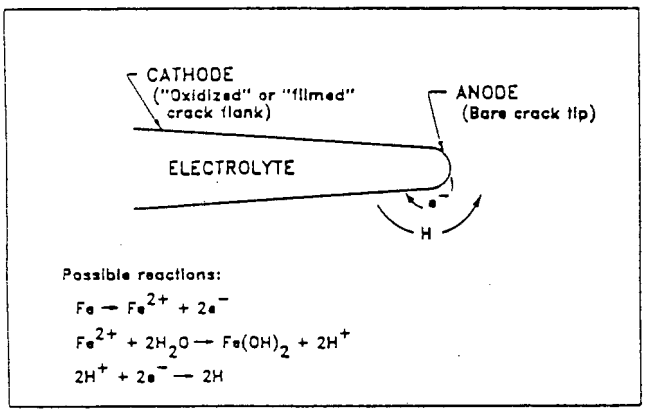

Figure 3.5: Possible electrochemical reactions at the crack tip[37].

3.4.2.3 Compositional and Electrochemical Changes within Cracks

The geometry of a pit, crevice or crack restricts mass transport between solutions in the cavity and that in the bulk resulting in changes in solution composition and electrode potential in the cavity and subsequently in rates of chemical reactions. The extent of these changes for a given metal depend on the geometry and dimensions of the cavity, mass transport processes, time and bulk solution composition and potential. In addition, the application of mechanical stress leading to the exposure of bare metal can also have an important influence on local chemistry in cracks[41].

Thus geometrical discontinuities, whether in the form of pre-cracks or corrosion pits, will be as important for electrochemical reasons as for those concerned with their influence upon stress distribution[42]. The success of pre-cracked tests over plain tensile specimens in inducing stress corrosion cracking suggests that potential and pH conditions can develop within the confines of the discontinuity associated with the pre-cracking which are significantly removed from those existing on the outer surfaces. The recognition of the interactions between local chemistry (established by localised corrosion) and the crack propagation mechanism is considered a major achievement of the last two decades by Procter and Newman[26].

3.4.2.4 Potential in a crack

Vermilyea and Tedmon[43] analyzed the problem of potential drop in a crack assuming inert crack sides and an active tip, while Ateya and Pickering[52] performed similar calculations for a crack undergoing hydrogen charging in acid solutions with current drainage to the sides. More recently Doig and Flewitt[44] achieved essentially the same result viz. drops of the order of 100mV can occur along cracks upto 1cm in length. The potential drop in cracks and crevices of stainless steel was found to be generally ≤150mV under the free corrosion conditions for the conducting environments used in the investigations[44,46] but can be much more significant at more positive potentials as a consequence of high currents. The variation of potential with distance along an artificial crevice in type 304 stainless steel as recorded by Alvali and Cottis[47] is illustrated in Figure 3.6.

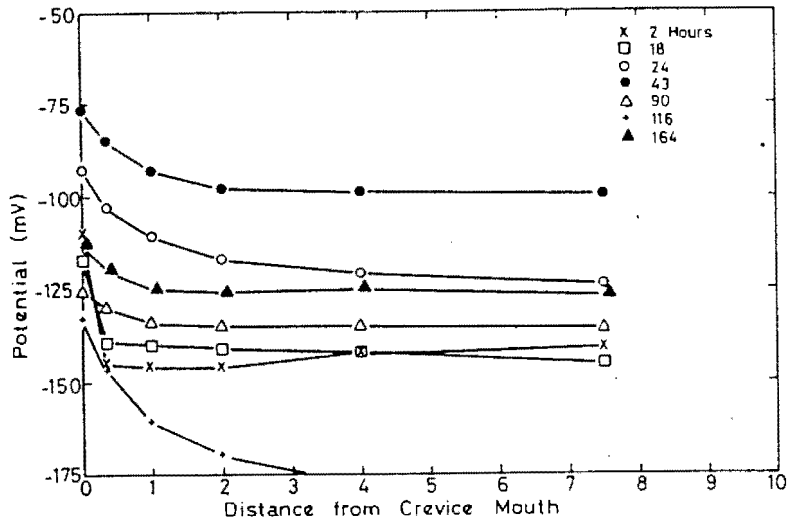

Figure 3.6: The variation of potential with distance from the crevice mouth as measured on type 304 stainless steel[47].

3.4.2.5 Effect of Bulk Solution Polarisation on Crack Tip Potential

Experimental evidence indicates the existence of limiting values of potential in cracks and crevices if the applied potential is moved to sufficiently anodic and cathodic values[48]. At anodic potentials this is associated with high anodic current densities and the formation of precipitated salt films on the metal surface or hydrogen gas bubbles in the crack. The formation or gas bubbles may also account for the large potential drops with cathodic polarisation below -1V SCE.

Brown[49] measured pH values and potentials at the tip of propagating cracks in medium strength steel immersed in 0.6 M NaCl at various bulk pH values and subjected to a variety of applied currents. The findings showed that irrespective of bulk solution pH or sign of the applied current, the crack tip pH and potential fall below the line at which hydrogen discharge is possible. These results are important in that it points to the environmental requirements for cracking in those materials that suffer from some form of hydrogen embrittlement as being less specific than those required for dissolution controlled mechanisms. Turnbull[41,50] did subsequently demonstrate that Brown's measurements of crack pH were probably affected by interactions with atmospheric oxygen, which would have oxidised ferrous ions to the ferric state, with consequent lowering of pH.

Parkins[24] found when measuring pH changes along a simulated crack that the crack tip potential was only significantly different from the applied potential at the crack mouth when these were markedly removed from the open circuit value. It is anticipated that at more passive potentials and also for systems in passive states that the potential drop is more significantly affected by crack depth and is smaller for shallower cracks[48,49].

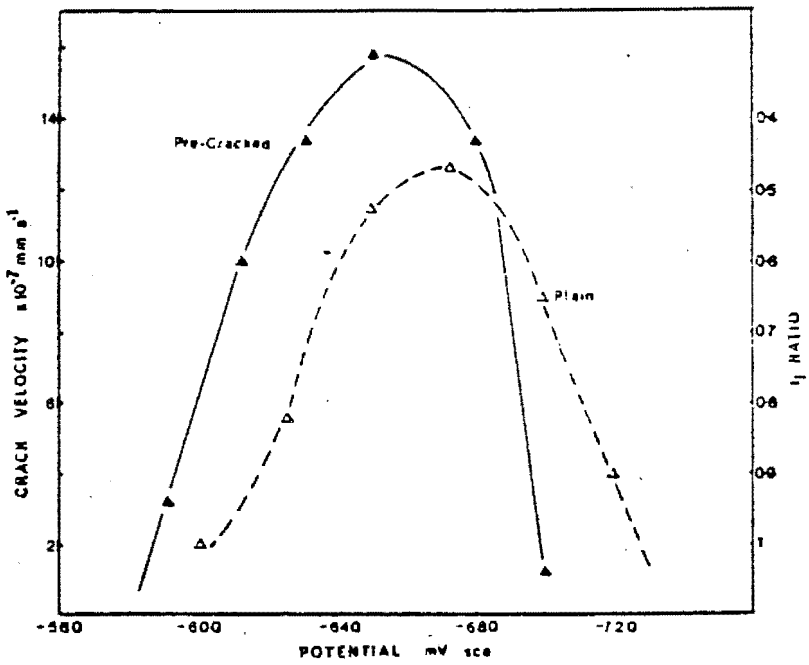

Figure 3.7: Potential ranges for cracking of pre-cracked and plain specimens of C-Mn steel subjected to slow strain rate stress corrosion tests in 1N Na_2CO_3 + 1N $NaHCO_3$ at 75°C (Cracking suseptibility measured in the pre-cracked specimen tests as crack velocity and plain specimen tests as time to failure ratio)[112].

Ford[51] considers the crack tip potential to vary little with changes in external potential, but rather that the crack tip chemistry becomes more concentrated in anions from the bulk solution. The solution chemistry is thus considered as a variable rather than potential.

Finally it may be deduced that if the potential drop along a crack is relatively large, then the potential range for cracking of initially plain specimens should be appreciably different from specimens with narrow pre-cracks as shown in Figure 3.7.

3.4.2.6 pH in Cracks/Crevices

Both the models of Ateya and Pickering[52] and Vermilyea and Tedmon[43] lead to the conclusion that there should be marked concentration changes within the environment contained in a crack. Ateya and Pickering predict that hydrolysis causes the crack tip pH to equilibriate at ≈3.5, while Vermilyea and Tedmon indicate M^+ concentration in the excess of 1M unless precipitation of dissolved cations occurs. The variation of pH along an artificial crevice in AISI 304 stainless steel with time as established by Alvali et al[47] is illustrated in Figure 3.8. The pH was measured to be in the range 1.7 - 2.7.

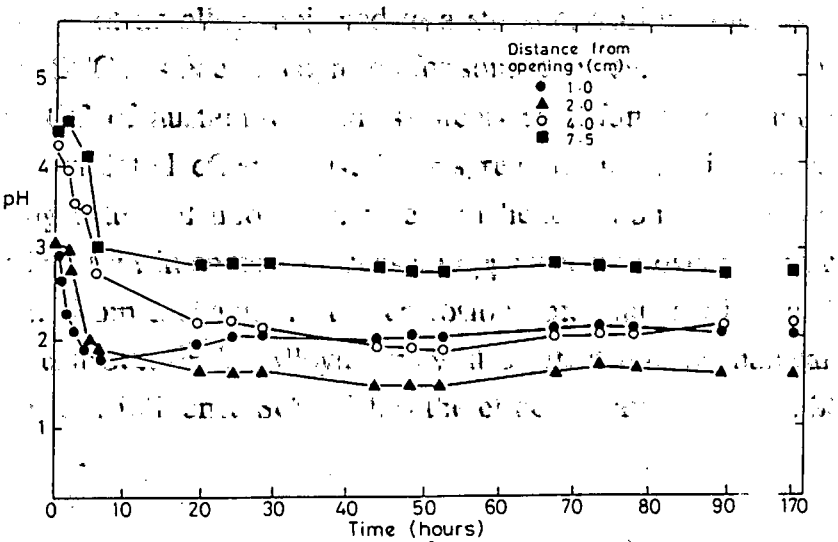

Figure 3.8: The variation of pH along the artificial crevice of type 304 stainless steel with time at open circuit potential[47].

Alvali and Cottis[54] also measured the pH in a simulated crevice in a high strength steel as a function of applied potential in sodium chloride solution. The authors reported that more positive potentials (relative to the "crevice rest potential") gave rise to anodic currents in the crevice with an attendant acidic pH. The converse occurred with the application of a negative potential. In free corrosion the pH is considered to be controlled by the potential of the external steel.

As regards stainless steels, the presence of Mo, chromium or ferric ions in solution can have significant influence on pH and hydrolysis of the chromium is sufficient to explain low pH values that have been measured at Ecorr[48] as illustrated in the chemical reactions below. Chromium can be dissolved from the appropriate chromium-bearing alloy but ferric ions are only present in a cavity if some oxygen is present and this is unlikely in SCC cracks. Several investigations of the pH in crevices of stainless steels[55] suggest that the pH will be in the region of 0 to 3.

$$2Cr + 3H_2O = Cr_2O_3 + 6H^+ + 6\acute{e}$$

$$Cr = Cr^{3+} + 3\acute{e}$$

$$Cr^{3+} + H_2O = Cr(OH)^{2+} + H^+$$

3.5 METALLURGICAL ASPECTS OF SCC

3.5.1 Composition

Alloying in particular but also structural variations to some extent may be expected to influence the electrochemical responses of an alloy subjected to a stress corrosion cracking environment. The influence of alloying on SCC has been recognised for some time eg. the well known "Copson curve" for chloride induced SCC of austenitic stainless steels as a function of nickel content[56]. A number of possible interrelated effects exist in this regard viz. the influence of alloying upon dissolution rate, filming rate and upon structure and hence upon the distribution of local cell action. It is thus possible that in some instances an apparent improvement in cracking resistance from alloying can result from a change in the corrosion potential relative to the potential range within which cracking can occur[30]. Alloying may also affect the mechanical properties of the material and in this manner influence SCC. Thus the effects of alloying upon SCC resistance may be expected to be complex.

Susceptibility to hydrogen is a marked function of both composition and microstructure[57]. Steel composition has a marked influence on the extent of trapping and hence on hydrogen adsorption. Integranular cracking in iron and steel is promoted by the presence of phosphorous, sulphur and other metalloids and impurities[58-60]. These effects of the impurities are considered to be primarily electrochemical and not metallurgical[61].

3.5.2 Microstructure

An obvious microstructural dependency of EAC exists, especially when intergranular with implications for chemical heterogeneity at grain boundaries. An alloy may exhibit structural

features, either as segregate or precipitate, usually at grain boundaries that cause a local galvanic cell to be established. This forms the basis of the so called pre-existing active path mechanism[42]. In line with this, phosphorous segregation has been shown to promote intergranular SCC of low alloy steels (Cr-Mo or Ni-Cr-Mo-V) in caustic or water environments at relatively oxidising potentials[62]. Molybdenum segregation appears to be damaging in caustic environments[63].

Associated with metalloid adsorption to prior austenite and ferrite grain boundaries, conditions favouring temper embrittlement also favour hydrogen embrittlement[64,65]. It has been shown[66,67] that carbides can act as a trap for hydrogen in bcc Fe-Cr alloys. Since the majority of chromium carbides in thermally treated samples lie on the grain boundary, hydrogen trapping by carbides will increase the grain boundry hydrogen concentration. It has also been demonstrated that sensitised steels only behave adversely when carbides are continuous at grain boundaries.

As the microstructure becomes more complex, with an inevitable strength increase, the hydrogen behaviour of an alloy becomes even more dominated by microstructure[68]. Microstructural effects can be ranked if strength and grain size are kept reasonable constant. Most studies have found that quenched and tempered martensite (or bainite) is most resistant to hydrogen, followed by spheriodized structures having intermediate resistance, followed by pearlitic/ferritice normalised structures usually with somewhat less resistance and finally by untempered martensite with much the least resistance[69].

It is frequently reported that coarse grained material is more susceptible to cracking than a fine-grained material, detailed analysis showing a Petch type relationship between grain diameter l, and stress $\acute{I}_i$ to initiate a stress corrosion crack ie. $\acute{I}_i = \acute{I}_0 + Kl^{-0.5}$ where $\acute{I}_0$ and K are constants of which K may be related to the surface energy associated with the formation of new surfaces. Besides the surface energy approach, the effect of grain size can be explained in terms of plastic flow characteristics of materials as influenced by grain size. The grain size term arises from the resistance to the formation of slip bands at the grain boundary. It follows that the grain size dependence of SCC simply reflects the fact that the latter is related to the plastic flow in the material[57]. Grain coarsening heat treatments are also postulated to induce crack initiation by increasing the slip step height as larger slip steps are more likely to rupture protective films. Proctor and Paxton[70] reported that reducing the grain size of 4340 results in a decrease in the crack velocity without affecting K_{ISCC}. The relationship between direction of stressing and grain directions of the metal influences SCC. Transverse testing is considerable more detrimental than longitudinial stressing, and short-transverse stressing is more detrimental than long-transverse stressing.

Grain orientation has a pronounced influence on stress corrosion crack morphology in high strength steels. If a crack propogates in a grain direction that is very stress corrosion susceptible, it

will remain in the same plane, and branching will be unlikely when the velocity and stress intensity criteria are fulfilled. On the other hand, if a crack propogates normal to the sensitive direction, then 90° bifurcation may be expected[25].

3.6. FRACTURE MODES

EAC may often lead to a change in the mode of cracking from the prevalent mode to a lower energy mechanism such as intergranular cracking, cleavage, quasi-cleavage and enhanced microvoid coalescence. The change in the mode of cracking is often accompanied by an increase in the crack growth rate.

Four classical failure modes prevail in SCC:

i) ductile failure i.e. microvoid coalescence
ii) poorly defined transgranular mode e.g. quasi-clevage
iii) relevatively brittle intergranular fracture (this depends on the relative strength of grain boundaries and lattice and the distribution of precipitates.
iv) cleavage.

Frequently the brittle macro appearance of SCC failures has led many to assume that a state of total brittleness exists during SCC. Lynch[71,72] carried out fractographic studies in numerous alloy systems including aluminium, iron-silicon, high strength steels and titanium alloys in liquid-metal, aqueous hydrogen and inert environments. These observations led to the conclusion that the microvoid coalescence process can sometimes occur on a much more localised scale in EAC than that which occurs in inert environments. This conclusion was first made by Beachem[73] for HAC in steels. Fractographical studies using SEM have been carried out to determine the crystallography of cracking[74,75] and to study the plastic processes involved in crack propagation, including crack arrest markings and the mechanisms of ledge formation in transgranular SCC[76].

3.7 MECHANISMS OF SCC

Procter and Newman[26] define an SCC mechanism as a combination of physical and chemical processes that accomplishes the separation of bonds at the tip, thereby advancing the crack.

Widely accepted mechanisms of SCC under static tensile loads have eluded experimentalists and theoroticians for decades. The simple explanation for this state of affairs is that atomic-scale events at crack tips in bulk specimens cannot be directly observed[33]. Arguments on the mechanistics of EAC have been directed from side to side concerning the role of slip, coplanarity,

criteria.

3.7.1 Energy Balance for SCC Fracture

An energy balance for fracture taking into account the chemical energy released during environmental fracture can be written as follows[42] :

Surface energy change	+	Plastic work done	=	Change in initial stored energy	+	Electrochemical energy released

.....(Equation 1)

The surface energy term is negligible by comparison with the plastic work term in the SCC of ductile materials and therefore may be neglected. West[78], using fracture mechanics and conventional electrochemical considerations together with various boundary conditions used the remaining terms from the equation to arrive at the much simplified equation of:

$$K_{ISCC} = \{k_1(P - k_2\eta)\}^{1/2}$$

.....(Equation 2)

where:

P = Appropriate plastic work term
K_I = Stress intensity
η = Anodic overpotential

Thus the two variables that affect K_{ISCC} or susceptibility to SCC are the plastic work term (P) and the anodic overpotential (η).

3.7.2 Stress Corrosion Crack Propagation Models

The implication of the above equations is that SCC will occur if a mechanism exists for concentrating the electrochemical energy release rate at the crack tip or the environment in some way serves to embrittle the material. These deductions form the basis of the SCC crack propagation models[57].

Historically the proposed models for SCC have fallen into two groups[27] viz.
i) those which consider that the crack propagation proceeds by preferential anodic dissolution
ii) those which propose that cracking occurs by mechanical fracture.

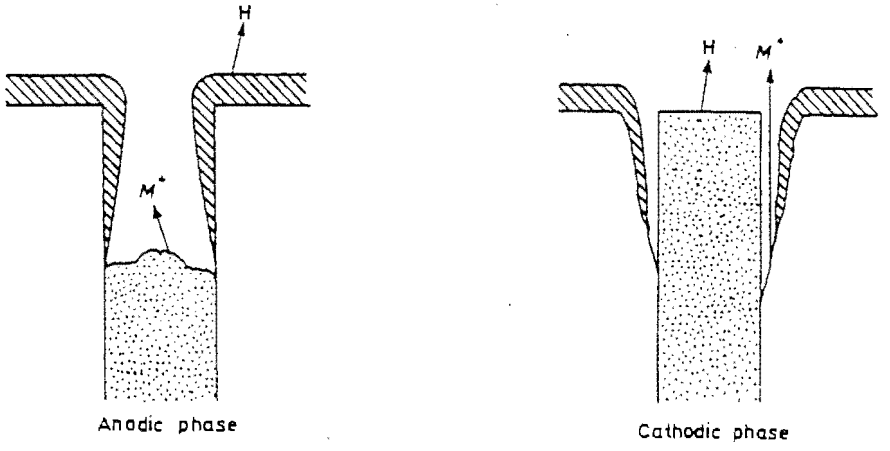

Figure 3.9: Pre-existing active path mechanisms, in which H represents cathodic hydrogen[79].

3.7.2.1 Anodic Dissolution Models

3.7.2.1.1 Pre-existing Active Path

Dix[79] suggests that an alloy may exhibit structural features, either as segregate or precipitate, usually at grain boundaries, that cause a local galvanic cell to be established. The precipitate or segregate may act as an anode in a local cell, or by acting as an efficient cathode, may cause dissolution to be localised upon immediately adjacent matrix as illustrated in Figure 3.9. Grain boundaries are particular sites for the heterogeneities that give rise to this form of attack and thus the pre-existing active path mechanism is likely to lead to intergranular SCC.

3.7.2.1.2 Strain Generated Active Path

This proposed model has several alternative names viz. slip-dissolution or film-rupture model. The basic hypothesis is that a protective film is ruptured by localised plastic deformation (strain) at the crack tip, permitting rapid anodic dissolution of the exposed substrate while the non-deforming crack walls remain protected by the film[80]. The active path along which the crack propagates is cyclically generated as disruptive strain and film build up alternate. This mechanism is illustrated in Figure 3.10. Propagation characteristics are thus related to the slip characteristics of the underlying metal as well as to the characteristics of the film[57]. The protective film is generally regarded to be a passive film and the rate of repassivation of the exposed surface is considered to be an important factor in determining the susceptibility to SCC. The strain generated active path mechanism is expected to result in transgranular cracking.

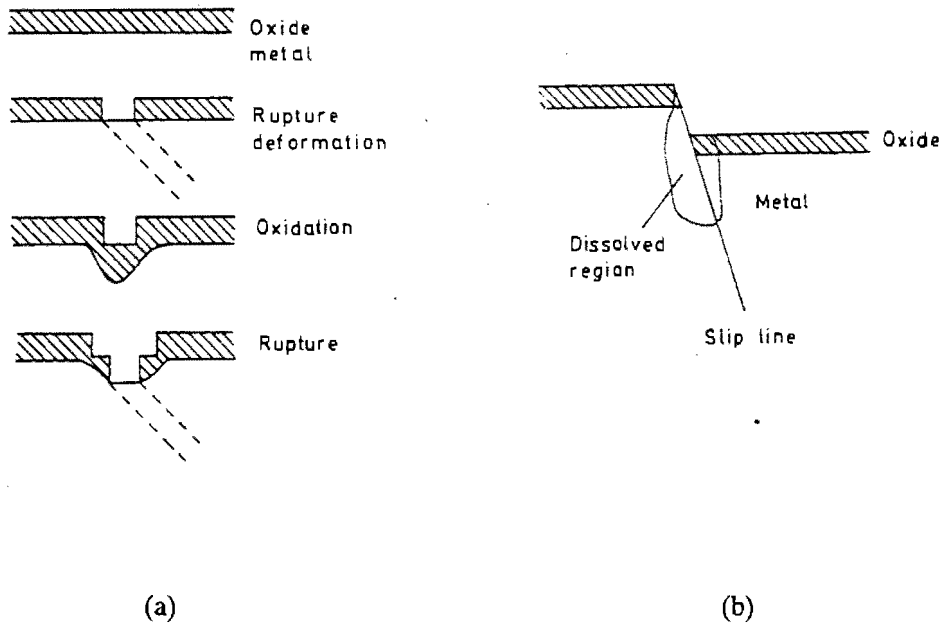

Figure 3.10: Strain-generated active path mechanisms. (a) Film rupture model and (b) slip step dissolution model[80].

Jones[81] outlines a mechanism of SCC in which anodic dissolution at film rupture sites relieves strain hardening and reduces fracture stress at the crack tip. Experimental evidence is cited to suggest that the relief of strain hardening occurs by the interaction of subsurface dislocations with divacancies created by anodic dissolution.

Varying amounts of criticism have been offered against the model. Bursle and Pugh[82] consider the slip-dissolution model not to reconcile easily with the fractographic observations of transgranular SCC viz. crystallographic nature of transgranular features. The film rupture model advocates a blunt crack since it offers no provision for restricting local plastic deformation at the crack tip. In addition, the matching of the opposing fracture surfaces is not consistent with the slip-dissolution model. Finally, the model has difficulty in explaining the existence of what has been identified as crack arrest markings on transgranular fracture surfaces. In general, the crack front would be expected to be intersected by a large number of active slip planes, therefore a large number of independent dissolution events will occur at any instant, causing the crack to advance unevenly.

3.7.2.2 Mechanical Fracture Models:

3.7.2.2.1 Ductile Fracture

i) The Tunnel Model

Hoar and West[39] showed that currents associated with straining electrodes may be very much greater than those observed at static surfaces. This observation forms the basis of the tunnel model proposed by Swann and co-workers[84] which was devised after the observation of corrosion tunnels in certain stress-corrosion systems. The theory is explained in terms of the potential remaining constant when slip occurs exposing fresh metal, this fresh metal being anodically

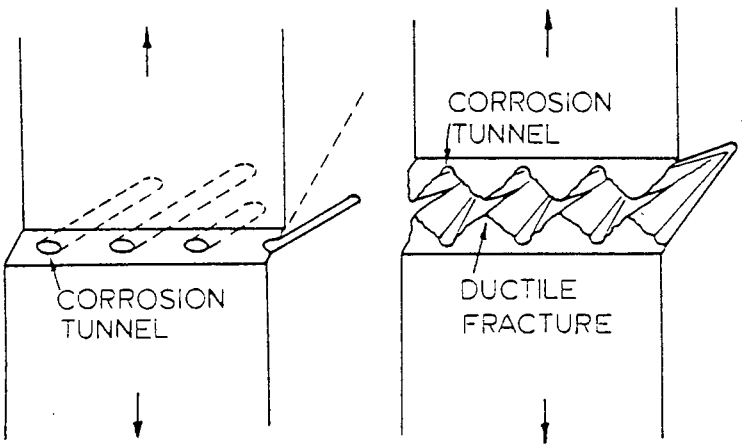

Figure 3.11: Schematic of the tunnel model, showing the initiation of a crack by the formation of corrosion tunnels at a slip step and the subsequent rupture of the metal ligaments. Propagation occurs by the repetition of this process[84].

polarised with respect to the rest of the crack tip. This then results in a sharp increase in the corrosion current resulting in the formation of a network of fine corrosion tunnels which grow in length and diameter until the remaining ligaments fail by ductile rupture. This is illustrated in Figure 3.11. This model only applies to transgranular SCC and fracture surfaces would be expected to exhibit a series of grooves extending in the direction of crack propagation, with walls between neighbouring grooves matching peak to peak on opposite faces. This has only been observed in an isolated case and does not comply with the general transgranular cleavage-like fracture which is prevalent in transgranular SCC.

ii) Film Induced Cleavage

In an extension of the film rupture model, Sieradski and Newman[57,85] introduced the concept that the films at the crack tip can induce microscopically brittle (cleavage-like) behaviour in intrinsically ductile metals via a series of discontinuous microcleavage events. A crack, once

initiated in the brittle film, is hypothesised to progress into the normally ductile substrate for an appreciable distance before being arrested by plastic deformation in the matrix.

According to Sieradski and Newman[85], the film induced cleavage concept has unified many disparate pieces of information in the literature on transgranular SCC. Previously it was thought that anodic processes could account for the rate of cracking without fracture, but in order to do so it was necessary to postulate unrealistically high reaction rates and crack tip strain rates. Also the explanation of the brittle fractography presented a problem. However, with this model improbable reaction rates and strain rates are no longer required because anodic processes are only responsible for ≈1% of the total crack advance and the fractography arises from the micro-cleavage process.

3.7.2.2.2 Brittle Fracture

The energy balance equation (Equation 1) reveals that with negligible contribution from dissolution, crack extension is facilitated by a reduction in the surface energy required to form crack faces or a reduction in the plastic work term by embrittlement in the crack tip region. The latter forms the basis of a number of postulated SCC mechanisms.

This embrittlement in the crack tip region is hypothesised to arise in a number of ways:

i) The environment provides species that are adsorbed at the crack tip to reduce the effective bond strength thereby permitting brittle fracture at low stresses. In criticism of the model it has been suggested that it cannot be reconciled with the discontinuous crack advance over distances indicated by crack arrest markings[27].
ii) The species may diffuse into the metal forming a brittle phase e.g. a hydride at the crack tip.
iii) Adsorption may occur at some region in advance of the crack tip where stress and/or strain conditions are particularly appropriate for the nucleation of a crack. In this instance hydrogen is usually regarded as the only species that can diffuse with sufficient speed to account for the observed crack propogation rates[57].

3.7.2.2.3 Overview of Hydrogen Embrittlement

The basic processes which occur during hydrogen embrittlement can be summarised under the following headings[69].

i) Hydrogen Sources

Hydrogen may be derived from hydrogen gas molecules which adsorb onto the metal surface and dissociate, by recombination of hydrated protons with electrons at the metal surface or by reaction between hydrogen containing molecules e.g. alcohols and the metal surface to release hydrogen.

ii) Hydrogen Transport

Hydrogen transport is largely by diffusion but it has also been shown to be carried by Cotterell atmospheres accompanying moving dislocations. The latter method is several orders of magnitude faster than diffusion. Mobile hydrogen can be rapidly transported to local stress centres, while strongly trapped hydrogen is immobilised at the original trapping site[68].

iii) Hydrogen Destinations

Traps that have been suggested for hydrogen embrittlement include a number of microstructural heterogeneities viz vacancies, dislocations, stacking faults, microcracks, grain boundaries, non metallic inclusions, phase boundaries and micropores[57,86]. Bernstein and Thompson[68] demonstrated a complex interplay of weak and strong traps affecting the distribution of hydrogen. In pre-charged specimens, weak traps (such as solute atoms) act as sources of hydrogen for dislocations, which can then carry hydrogen to a strong trap (interface), which is a potential site for crack nucleation.

iv) Fracture

Hydrogen may induce a more brittle mode of fracture than the usual mode but it does not induce some characteristic hydrogen mode[69]. Pronounced hydrogen embrittlement can occur without any change in fracture mode, although when a change of mode occurs, it usually corresponds to marked brittleness. There is not even complete correlation between the severity of embrittlement and the occurrence of a brittle fracture mode[68].

Fractographically, crack surfaces of iron and steel degraded by hydrogen include ductile dimple rupture, ductile tearing, intergranular separation, quasi-cleavage and cleavage forms[87,88]. The fracture mode in the presence of hydrogen depends on the stress intensity (K) value, because as K decreases, the associated plastic level at the crack tip decreases and it is only able to drive less plastic fracture modes. Intergranular hydrogen cracking in iron and steel is promoted by the presence of P,S and other metalloids and impurities[60].

These processes contributing to hydrogen embrittlement are summarised in Figure 3.12.

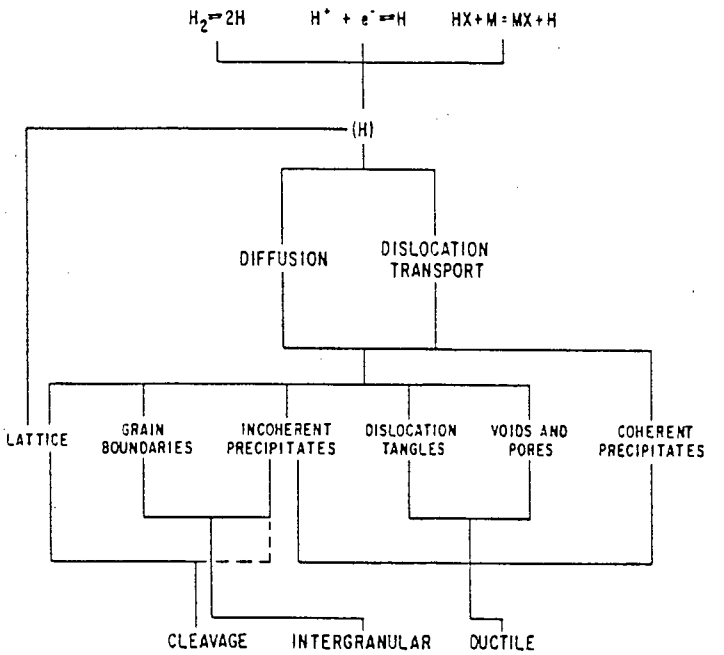

Figure 3.12: Possible interaction paths for the transport of hydrogen atoms produced at the crack tip to regions in the matrix where atom-atom rupture occurs[68].

3.7.2.2.4 Proposed Hydrogen Embrittlement Models

The different forms of hydrogen in the lattice form the basis of the various proposed mechanisms.

i) Pressure Theory

The basis of this theory is the localised generation of internal stresses due to the pressure developed when hydrogen recombination occurs at heterogeneities[89,90]. This additive stress then simply lowers the critical stress for crack propagation.

This theory became questionable when it was found that brittle crack extension was possible at hydrogen partial pressures considerably less than one atmosphere[91]. Fracture processes dominated by void growth rather than void nucleation are postulated to be more susceptible[86].

ii) Surface Energy

The fundamental idea of this theory is that hydrogen is adsorbed preferentially on an interface or

Arguments against this model include that it underestimates the work of fracture, it cannot account for the reversibility of degradation, for example in delayed failure; it cannot account for discontinuous crack propagation and finally it is inconsistent with the finding that oxygen, which has a greater heat of adsorption than hydrogen, suppresses cracking in the presence of hydrogen[86].

iii) Cohesion Model

This mechanism was originally proposed by Troiano[92] and was later resumed by Oriani[93]. According to this theory, hydrogen accumulates within a few atomic distances from the crack tip in response to the lowering of its chemical potential by elastic stress, thereby lowering the cohesive force of the lattice. Troiano considers the hydrogen to collect in zones of maximum triaxiality whereas Oriani considers it to accumulate at the crack tip in the zone where deformation does not obey Hookes Law. Rice[94] suggests that such an accumulation could well occur preferentially along grain or carbide boundaries, in agreement with the observed tendency of cracks to follow microstructural heterogeneities.

iv) Enhanced Plastic Flow

Beachem[95] proposed a hydrogen assisted-cracking theory in which the effect of hydrogen is to enhance dislocation motion in the presence of low stresses. In his hydrogen-assisted cracking theory he claims that hydrogen penetration softens the matrix, favouring plastic strain, which in its turn enhances hydrogen entry. The self acceleration of this mechanism then induces localised rupture.

Lynch[71,72] proposed an adsorption induced localised slip model. After observing the dislocation processes occurring during ductile and brittle fracture it was concluded that EAC occurs because adsorption facilitates the injection of dislocations from crack tips and thereby promotes the coalescence of cracks with voids ahead of cracks. Lynch concludes that the proportion of dislocations injected from crack tips relative to those activated from near-crack tip sources i.e. the degree of embrittlement, will depend on the adsorbed species.

3.7.3 Conclusions

The demonstration that SCC occurs in a wide range of environments has weakened models that postulate a high degree of specifity e.g. the stress-sorption model, while strengthening the electrochemical dissolution models. It has been suggested[42,69,86] that these different mechanisms of EAC occur within a continuous spectrum, with gradual transition from the one to the other as

of EAC occur within a continuous spectrum, with gradual transition from the one to the other as the dominance of corrosive processes is replaced by stress or strain. This leads readily to the concept that alloy composition and structure, electrochemistry and stress may interact in a variety of ways and the transformation from one mechanism to another may result from a change in either alloy characteristics or environmental conditions.

3.8 HIGH STRENGTH STEELS

The higher strength steels are generally more susceptible to SCC and to a greater degree hydrogen damage, than the lower strength steels. Furthermore, in the higher strength range, the higher the strength of the steel, the greater its susceptibility to cracking[57,96]. Decreasing the strength level of carbon hardened, low alloy steels has a significant effect on crack growth kinetics. Studies on 4340 steels at high tensile strength levels (1930-2070 MPa) have revealed that crack velocity is proportional to stress intensity in Region II[97]. At lower strength levels however, crack velocity in Region II is constant and decreases with strength level.

Chu and Wei[98] used a combined fracture mechanics and electrochemical study to identify the rate-controlling process for crack growth in high strength steels in aqueous environments. The SCC behaviour of 4130 and 4340 steels was studied as a function of temperature in deaerated 0.6 N NaCl solution. Chu and Wei hypothesise that crack growth in high strength steel in aqueous environments is controlled by the rate of electrochemical/chemical reactions with water. The results are also consistent with a hydrogen embrittlement mechanism for enhancement of crack growth rates.

It has been postulated that hydrogen embrittlement is responsible for most cases of embrittlement of high strength steels, even at applied anodic potentials. This is explained in terms of the environmental conditions within a crack being far more acidic than in the bulk solution (see "Crack tip chemistry") and therefore conducive to hydrogen evolution and adsorption. Raising the potential in order to stimulate anodic dissolution can decrease the pH at the crack tip so that a decrease in time to failure under these conditions maybe diagnostic of hydrogen embrittlement rather than active path cracking[57]. A correlation of SCC with localised corrosion does not distinguish between hydrogen embrittlement and anodic dissolution as crack propagation mechanisms, since either may be favoured by passivity breakdown as shown by Figure 3.13[53]. This view is supported by Troiano, Steigerwald and Barth[99] who demonstrated that it is possible to absorb hydrogen under anodic polarization in a high strength steel and furthermore that this hydrogen behaviour is directly related to failure behaviour. This is illustrated in Figure 3.14.

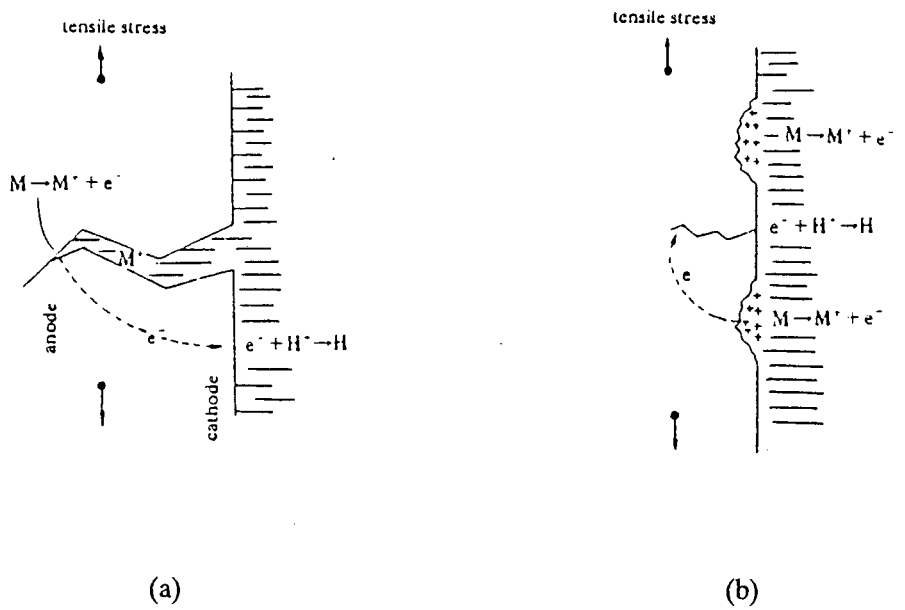

Figure 3.13: Localised corrosion reactions; (a) - stress corrosion cracking; (b) - hydrogen embrittlement[53].

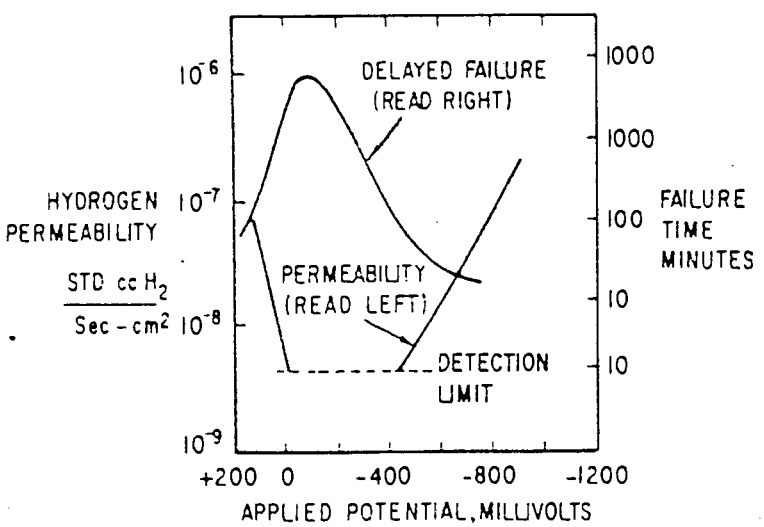

Figure 3.14: Comparison of delayed failure data at an applied stress of 50ksi and hydrogen permeability results for doubly activated 9-4-45 steel[99].

3.8.1 Effect of Tempering on EAC

In low alloy steels, the process of temper embrittlement occurs by the segregation of residual impurities such as phosphorous to prior austenite grain boundaries in what is otherwise a relatively stable microstructure[100,101]. Hydrogen and temper embrittlement interactions have been observed in several low alloy steels[58,102-105]. This temper embrittlement-hydrogen embrittlement synergism has been attributed to several mechanisms.

i) Segregated impurities inhibit the recombination of hydrogen atoms, increasing the concentration of atomic hydrogen at the grain boundaries[106].
ii) A positive thermodynamic interaction between segregated impurities and hydrogen encourages the migration of hydrogen to interfaces under stress[107].
iii) Hydrogen itself acts as an embrittling agent and its effect is simply added to that of other segregate species[108].

The results of numerous tests on 13% Cr alloys led Truman et al[109] to suggest that the relative importance of the two postulated mechanisms depends on the tempering temperature being used; with higher temperatures the active path mechanism is favoured and with lower temperatures hydrogen embrittlement.

As regards fracture mode, Lynch[110] after testing a tempered martensitic steel in a gaseous hydrogen atomosphere, found that crack growth occurs predominantly along prior-austenite and martensite lath boundaries, rather than along crystallographic planes. This observation was reasoned as follows:
i) adsorption occurs preferentially at boundary/surface intersections
ii) voids form preferentially along boundaries
iii) impurities are segregated at prior austenite boundaries.

3.9 STRESS CORROSION TEST METHODS

3.9.1 Constant Total Strain Tests

The constant strain (fixed-displacement) tests form by far the most popular test group. This is by virtue of the fact that they usually involve bend tests in a variety of forms utilising simple, cheap restraining jigs[111].

The constant strain tests are sometimes called the decreasing-load tests because after the onset of SCC, the gross section exposure stress and the average stress on the remaining cross-section begin to decrease. This results from the opening of the crack (or cracks) under the high stress

concentrated at the crack tips, thus causing some of the applied elastic strain to change to plastic strain.

The problems associated with these constant strain tests are usually related to the poor reproduceability of the stress level (if a quantitative measure of it is available). Also the limitations of simple bending theory, usually used to calculate the stress level, can lead to appreciable errors in anticipated stress.

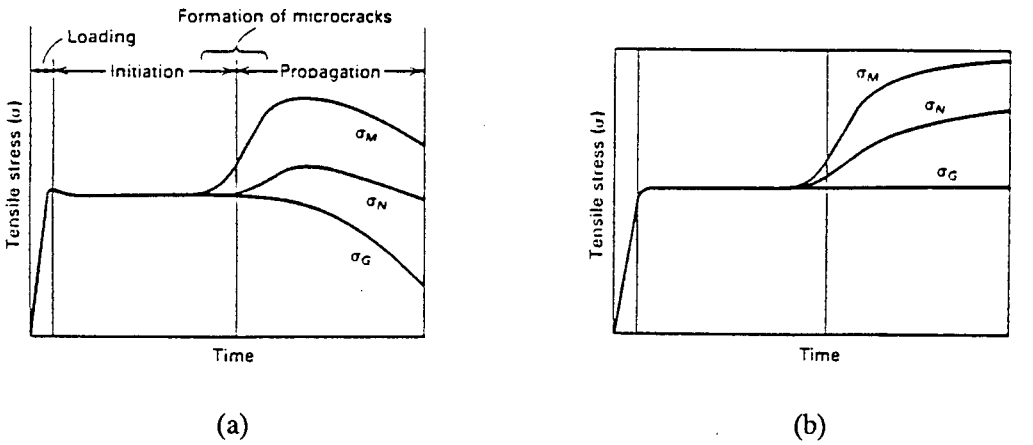

Figure 3.15: Schematic comparison of the changing stress during initiation and growth of isolated stress-corrosion cracking in constant-strain and constant-load tests of a uniaxially loaded tension specimen; (a) Constant strain test; (b) Constant-load test. σ_M is the maximum stress at the crack tip, σ_N is the average stress in the net section, and σ_G is the applied stress to the gross section[21].

3.9.2 Constant Load Tests

The constant load test, as the name implies, involves the maintenance of a predetermined constant load for the duration of the test. Since the effective cross-section of the test piece is reduced by crack propagation, the constant load test involves an increasing stress situation. The stress versus time curve for the constant strain and constant load tests are compared in Figure 3.15. Consequently the constant load tests are more likely to lead to earlier failure than the constant strain tests, with complete fracture. The latter, because of the associated relaxation, can produce cracks that eventually stop propagating and so total failure may not be observed. As a consequence of the above it is found that constant load tests generally yield lower estimates of K_{ISCC} than constant strain tests. In both the constant load and constant displacement test, the stiffness of the test frame exerts a marked influence on results and this often hinders the comparison between the results of independent laboratories[21,111].

3.9.3 Slow Strain Rate Testing

The main feature of this test method is the use of dynamic strain to stress the specimen in contrast to the conventional SCC tests (constant load and constant strain) which are conducted under a static stress condition. In essence the slow strain rate (SSR) test comprises straining a specimen at a slow, constant strain rate under controlled environmental conditions[112]. Typical strain rates range from 10^{-4} to $10^{-8}s^{-1}$. The strain rates are in the critical range to maintain the delicate balance at the crack tip between deformation, dissolution, film formation and diffusion. The mode of cracking found after SSR testing is characteristic for the material/environment under investigation[113].

The slow dynamic strain at the crack tip makes the SSR test a more severe test than the conventional static SCC tests. The importance of slip at the crack tip in SCC has been recognised in a number of the proposed mechanisms e.g. slip dissolution model, hydrogen embrittlement etc. During a static test, the driving force for slip relaxes with time and the rate of slip step emergence decreases accordingly whereas with the SSR test with its continual dynamic strain, slip-step emergence is induced artificially at a relatively constant rate[113,114].

The advantages and disadvantages of the SSR test method over the conventional test methods have been summarised as follows by Kim and Wilde[113].

1. The primary advantage of the dynamic slow strain test procedure is that it is much more aggressive in producing SCC than the conventional constant strain or constant-load tests so that testing time is considerably reduced.

2. Acceleration of the SCC process is achieved through imposing a slow strain rate on the metal without adjusting solution composition, concentration or temperature beyond the range of interest.

3. The SSR procedure reduces the incubation period for crack nucleation by virtue of continuous straining above the elastic limit on smooth surfaces and thereby avoids the pitfalls associated with reducing incubation times by means of pre-cracking etc.

4. The SSR test is ideally suited for rapid identification of environment/metal combinations which will produce SCC.

5. The SSR test can be used for quantitative ranking of the SCC properties of steels having similar microstructures and strength levels.

6. The SSR test can produce SCC on materials that have performed satisfactorily in the field owing to the aggressiveness of the tests. Thus discretion must be exercised in translating SCC susceptibility observed in the laboratory to anticipated service performance.

7. The results of the SSR test are positive in that failure either occurs prematurely in a brittle fashion if SCC occurs otherwise in a ductile manner.

3.9.4 Correlation Between SSR and Conventional Tests

It is worth noting that because of the fundamental difference between the expressions for SCC susceptibility of conventional tests (time of failure) and those of SSR tests (UTS, fracture stress, percentage reductions in area or fracture energy), a comparison of the results of the different testing techniques can only be of a qualitative nature. The main features of such a comparison usually involve the estimation of the degree of susceptibility to SCC of different materials in the same environment or the determination of the critical potential for SCC in a given environment[115].

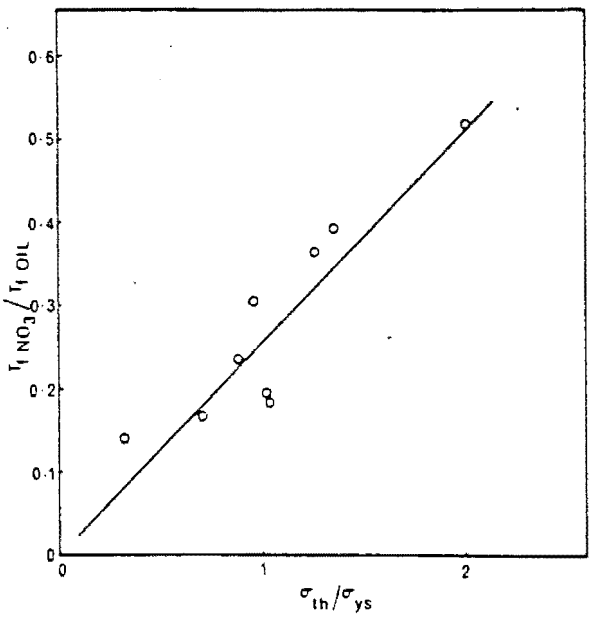

Figure 3.16: Relationship between time to failure ratio from slow strain-rate tests and the normalized threshold stress from constant strain tests on low alloy ferritic steels in boiling 4N NH_4NO_3[112].

Parkins[112] reports reasonable correlation between appropriate strain rate and constant load tests. Figure 3.16 shows the comparison between the results of SSR tests and constant load tests performed on some low alloy ferritic steels in boiling 4N ammonium nitrate. An allowance for the influence of alloying on the mechanical properties of the steels has been made by normalising the SCC results by dividing the threshold stress for each steel by its yield strength. Buhl[115] reports that for aluminium alloys the results of SSR tests are not in complete agreement. However, the

results with titanium alloys and high alloyed chromium and chromium-nickel stainless steels obtained with the different testing techniques are reported by Daniels[116] to be in good agreement with each other.

CHAPTER 4

MATERIALS AND EXPERIMENTAL METHODS

4.1 MATERIALS

The SCC susceptibility of 927 was assessed in four material conditions viz. as-rolled, as rolled and tempered, as welded and welded followed by post weld heat treatment. The four material conditions together with the associated thermal treatment procedures are summarised in Table 4.1.

Condition	Thermal Treatment	Nomenclature
As rolled	Hot rolled at 1250°C and air cooled	AR
As rolled and tempered	Tempered at 700 °C for 1 hour	AR & T
As welded	As rolled material welded with 309L electrodes at an input of 2kJ/mm.	W
As welded and post weld heat treated	Welded as above followed by heating to 1050°C for 1 hour and air cooling	PWHT

Table 4.1: The four material conditions used in the SCC programme and the thermal procedure adopted in obtaining the various microstructures.

4.2 MICROSTRUCTURES

Microstructures were characterised using conventional metallographic techniques, the final surface finish obtained by mechanical polishing with a 0.25μm diamond paste. The microstructures were revealed by dip etching. The subsequent microstructural examination was carried out on a REICHERT MeF_2 metallograph in the bright field mode. Oblique lighting, polarised light and the Nomarski interference technique were adopted where necessary to enhance surface relief.

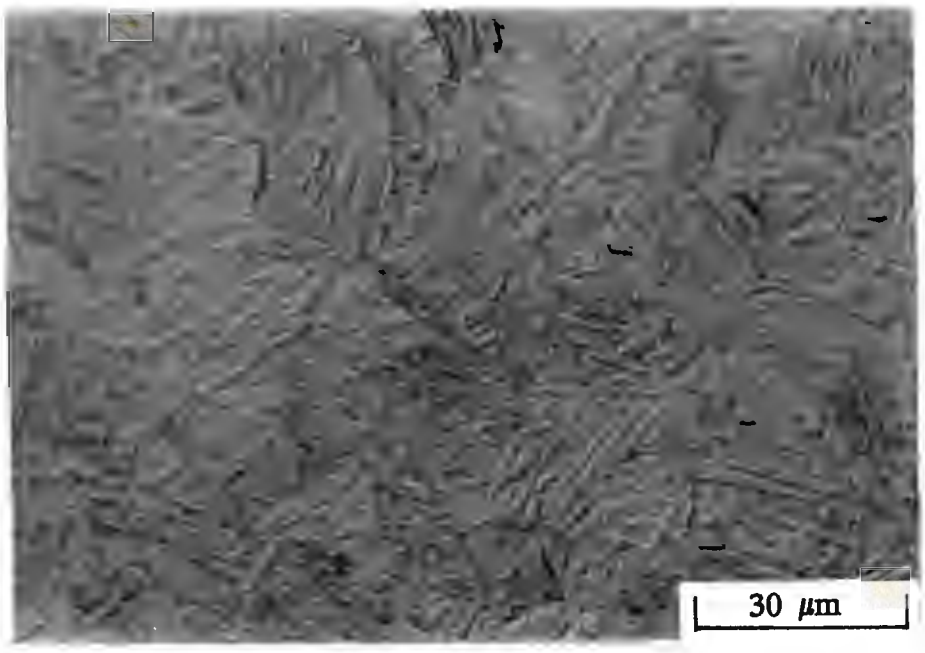

Figure 4.1: Optical micrograph of the as-rolled 927. Microstructure consists of a relatively high carbon, fine lath martensite.

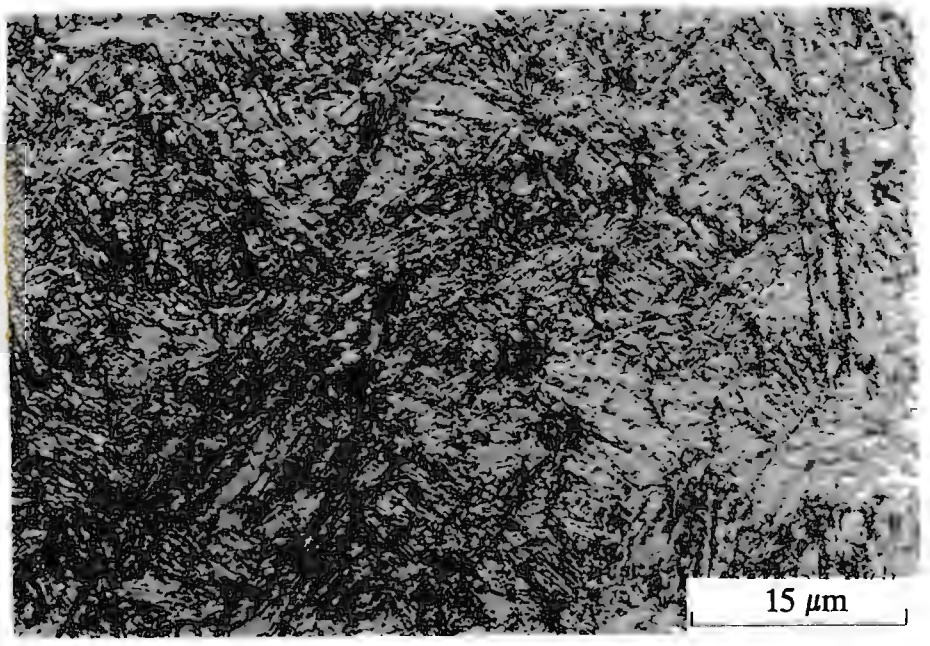

Figure 4.2: The microstructure of the as-rolled material tempered at 700°C for 1 hour. This treatment has resulted in an increase in the size and volume of the carbide precipitates in the microstructure.

Figure 4.3: The fusion zone of the as-welded material. The weld metal is fully austenitic while the parent metal in the vicinity of the weld exhibits a similar microstructure to the tempered material.

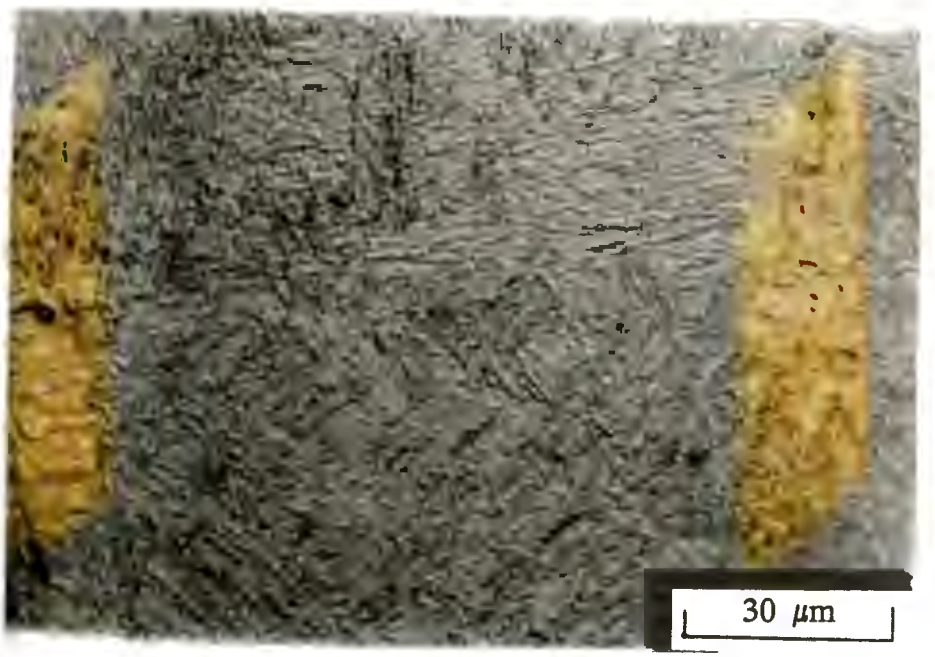

Figure 4.4: The parent material in the vicinity of the weld of the post weld heat treated sample. The microstructure consists of tempered lath martensite with a dispersion of carbides.

The microstructures of the four material conditions are shown in Figures 4.1 - 4.4. All etching was carried out using 5g picric acid, 8g $CuCl_2$, 20ml HCl and 6ml HNO_3. The microstructure of 927 in the as-rolled condition (Figure 4.1) consists of a relatively high carbon, fine lath martensite. TEM studies[9] have revealed the existence of a thin, continuous layer of interlath retained austenite. An X-ray analysis of the material using a Phillips diffractometer yielded a retained austenite content of between 2 and 7% depending on finished rolled plate thickness. Thomas et al[117] in their investigation of the properties of Fc/Cr/C alloys with similar microstructures of heavily dislocated, autotempered lath martensite and thin films of interlath retained austenite attributed the good toughness of the material to the latter. The good toughness of 927 is attributed to the microalloying which has resulted in a fine grain size with the associated increase in volume of retained austenite. The tempering treatment has resulted in an increase in the size and volume of the carbide precipitates in the microstructure as shown in Figure 4.2. The bulk hardness has been reduced from $520HV_{30}$ to $275HV_{30}$. The microstructures of the welded and post weld heat treated materials of Figures 4.3 and 4.4 respectively reveal a similar microstructure of tempered 927 in the HAZ and a fully austenitic weld metal. The hardnesses of the parent material and weld metal of the as welded specimens was measured at $465HV_{30}$ and $320HV_{30}$ respectively. The PWHT specimens yielded hardnesses of $435HV_{30}$ and $342HV_{30}$ in the parent and weld metals respectively.

4.3 EXPERIMENTAL METHODS

4.3.1 Slow Strain Rate Testing

The slow strain rate technique for assessing SCC susceptibility comprises of straining a test specimen at a slow constant strain rate under controlled conditions. The advantages and limitations of this technique were outlined in section 3.9.3. The various experimental parameters in SSR testing include:

i) Strain Rate

Strain rate is probably the most important parameter in SSR testing. Strain rates of the order of $10^{-6}s^{-1}$ have been found to be effective in inducing SCC in many alloy/environment systems. In alignment with this observation a strain rate of $1.52 \times 10^{-6}s^{-1}$ was selected.

ii) Metal Composition and Structure

For the purposes of this investigation the material was tested in the four conditions outlined in Table 4.1.

iii) Environment

The specifity of environment and material in conjunction with a tensile stress in promoting SCC is embodied in any formal definition of SCC. Tests were conducted in four aqueous solutions viz. 1000ppm chloride, 1000ppm sulphate, 500ppm nitrate and a simulated mine water which is a combination of the above ionic concentrations. All solutions were prepared using analytical grade sodium salts in distilled water in order to avoid the additional complication in the interpretation of the SCC process of introducing different cations. The simulated mine water is based on the composition of an average mine water[118] and has a near neutral pH of 5.6 to 6.2. Tests were performed using the separate ionic solutions in addition to the real solution of interest viz. the simulted mine water, in a bid to identify those ions which exert an inhibitive or aggressive effect on the SCC process.

iv) Temperature

All tests were regulated at the typical mine water temperature of 25°C.

v) Potential

The majority of SCC tests were conducted at free corrosion potential which is the condition of practical interest in mining applications. It is however recognised that small changes in mine water composition can move the potential into and out of the critical potential range. For this reason tests were performed using potentiostatically applied anodic and cathodic potentials to determine the extent and location of the critical potential range for SCC susceptibility in the mine water solution as well as to provide insight as to the operative SCC mechanisms.

4.3.2 Slow Strain-rate Test Apparatus

4.3.2.1 Load Frame

The test rig used in this investigation is shown in Figure 4.5. The slow cross-head speeds necessary for SSR testing are achieved by means of a Reynold Croft direct current motor (0.18kW at 1300r.p.m) which is geared down using two preboxed, fixed ratio gear boxes. The drive is transmitted to the test frame using toothed belts via further speed reducing pulleys to a worm and screw gear. Crosshead speed has been adjusted by means of a ten turn potentiometer to a steady displacement of 4.2×10^{-5}mms^{-1}. With a specimen gauge length of 27.64mm this corresponds to an initial strain rate of 1.52×10^{-6}s^{-1}. The lower end of the specimen is coupled to a pull rod which projects down through the centre of the hollow screw gear and connects directly to the load frame via a load cell and a rose bearing. The top end of the specimen is joined to the moveable carriage via a specimen grip and an universal joint for alignment purposes.

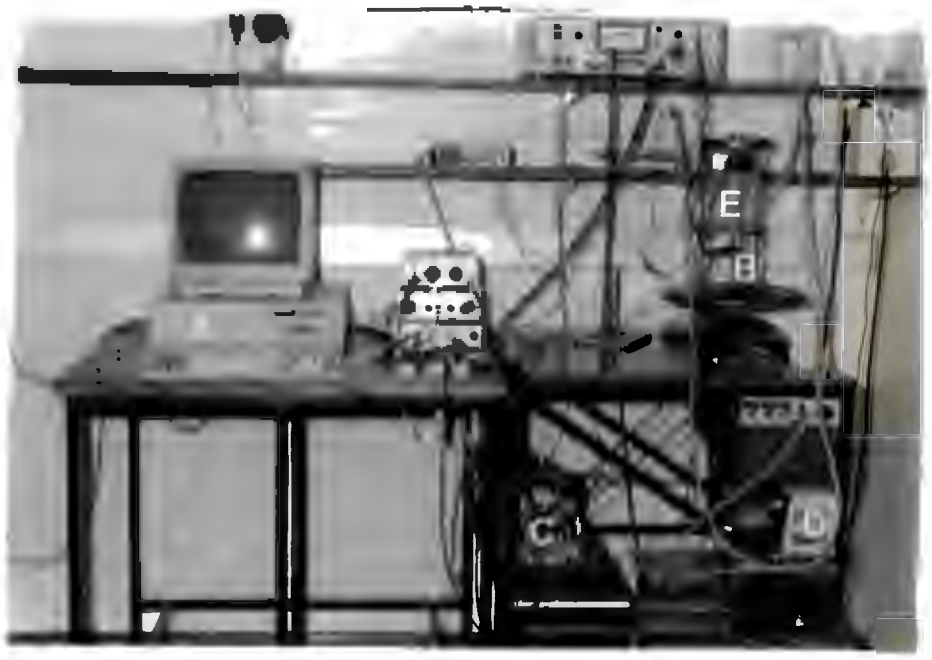

Figure 4.5: The slow strain rate apparatus and ancillary equipment; A - personal computer with controlling software and A/D card; B - load frame; C - electric motor; D - external environment conditioning unit; E - test cell; F - potentiostat; G - controlling electronics.

4.3.2.2 Test Cell and Environment Conditioning

The test cell is illustrated in Figure 4.6. It consists of a polymethyl methacrylate (PMMA) cylinder with a volume of 1300cm^3. An "O" ring seal is located in the bottom for the passage of the test specimen to the specimen grip. The cell is provided with a lid to minimise evaporation, to house the two high purity graphite counter electrode as well as the Saturated Calomel reference electrode (SCE) salt bridge.

Solution conditioning is performed externally in a 6 litre plastic bath using a thermo-regulating pump unit. This large volume of solution was selected in order to provide a buffering against evaporation, temperature and pH variations as well as the effect of anodic dissolution of the specimen. The solution is fully aerated in this bath using an aquarium pump and is circulated to the test cell using silicone rubber tubing. The flow rate was set at 400cm^3/min using a pipe clamp.

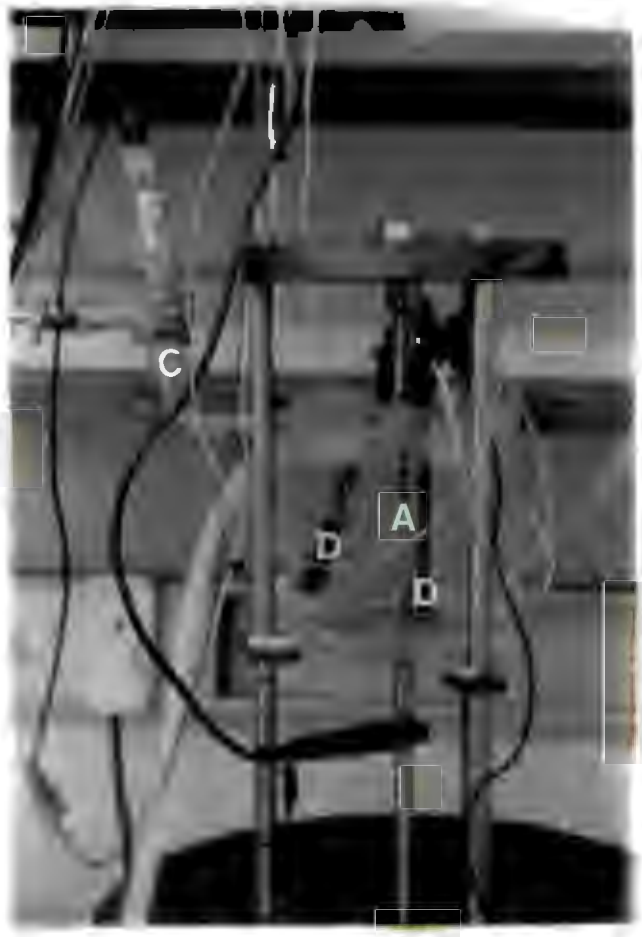

Figure 4.6: Details of the corrosion cell; A - coated specimen; B - saturated calomel reference electrode (SCE); C - SCE salt bridge; D - graphite counter electrodes

4.3.2.3 Ancillary Equipment

An essential requirement of the slow strain-rate apparatus is the ability to continuously monitor load and elongation for the duration of the test. For this purpose a 10kN load cell having a calibration factor of 0.492kg per microvolt output per volt activating input was fitted to the test rig in the manner described. The specimen extension was measured using a plunger type LVDT which monitors the motion of the cross-head. The LVDT has an output of $0.796 Vmm^{-1}$ over a displacement of ± 12.5mm.

Electrochemical control and monitoring were performed using a Wenking LT-78 potentiostat. The instrument is capable of monitoring Ecorr or controlling the specimen potential within a ± 2000mV range and monitoring the resultant current. A Saturated Calomel Electrode (SCE) was used as the reference electrode together with an ionic conductor bridge designed to fit into the test cell. The SCE electrode was the only reference electrode used in the testing

programme and hence forth references to electrochemical potential will not be accompanied by the abbreviation SCE.

4.3.2.4 Data Aquisition and Storage

Data capture is performed using an IBM compatible PC equipped with an Eagle Electric PC-30 analog multifunction board. The card has a resolution of 2.5mV over the 10V range for which it is configured. The board is accessed using Borland's Turbo Pascal.

In-house software was developed[120] using Turbo Pascal which obtains all the information relevant to the test via operator input, initialises all parameters, accesses subroutines to obtain data from the A to D, accesses the system timer, activates routines for data sampling, averages and then saves the data at one hourly intervals. Data that is saved during testing includes the voltages from the load cell, the LVDT, the potentiostat and the time. A second program reads the raw data saved during the test and converts it to conventional engineering units of stress, strain, current density and potential which are then stored in files which are compatible with the commercial spreadsheet package Lotus-123 for further manipulation.

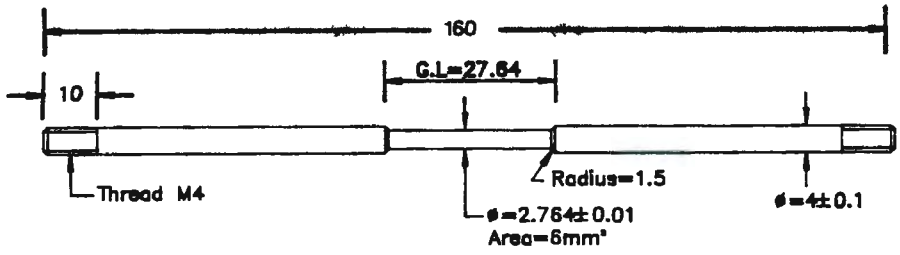

Figure 4.7: The dimensions of the plain tensile specimen used in the SSR test programme.

4.3.3 Test Specimens

Standard tension specimens as layed out in ASTM E8 "Standard Methods of Tension Testing of Metallic Materials" are generally recommended[21]. Generally speaking smooth specimens are preferred in SSR testing but notched or pre-cracked specimens can be used to restrict cracking

to a given location. In this test programme a smooth tension specimen having a gauge length of 27.6mm and a gauge diameter of 2.76mm was selected as illustrated in Figure 4.7. Two specimens were prepared with the gauge lengths transverse to the rolling direction, the remainder with the gauge lengths in the direction of rolling. The welded and PWHT specimens were prepared across a 30°V butt weld with the weld line and associated HAZ in the gauge length. All specimens were given a similar surface finish by polishing the gauge length with 1200 grit paper on the lathe.

4.3.4 Experimental Procedure

Firstly the gauge length and diameter of the specimen were measured using a vernier caliper. Thereafter the specimen was coated with a commercial laquer, leaving the gauge length exposed. This was done to limit the corrosion activity to the gauge length where SCC was likely to initiate. After drying, the specimen was placed in the test cell. A small preload was then applied to the specimen to remove any slackness in the system. The electronics were switched on and given time to stabilise and thereafter zeroed using the software. A 6 litre solution was then prepared and allowed to circulate via an external loop for half an hour until it had stabilised at 25°C. During this time it was aerated using an aquarium pump. The necessary electrical connections were then made from the potentiostat to the specimen, counter electrodes and reference electrode. The two specimen ends were connected during testing to ensure that the specimen halves remained at the same potential after fracture. The solution was then circulated to the test cell. Crosshead motion was only initiated after allowing the system equilibriate and stabilise for approximately half an hour. In the case of impressed potential testing, the potential was impressed on the specimen for ten minutes prior to starting the test. Upon completion of the tests, specimen halves were removed from the solution, cleaned in alcohol in an ultrasonic bath, dried and stored in a dessicator for evaluation.

4.3.5 Evaluation of SSR Test Results

4.3.5.1 Microscopy

On completion of all the SSR tests, the specimen fracture surfaces were examined under the Cambridge S-200 scanning election microscope (SEM) to characterise the fracture mode. Representative SEM micrographs were recorded of the relevant surface features. If EAC was identified as evidenced by the presence of less ductile fracture modes than those obtained in the air tests, the specimen was mounted and cross-section metallography performed using an optical microscope. This cross-section metallography was used to characterise the SCC cracks viz. trans or intergranular and also to examine surface features e.g. nature of the corrosion pits or small, non propagating SCC cracks.

4.3.5.2 Analysis of SCC Stress-Strain Curves

A quantitative representation of the extent of SCC severity was derived from the various SCC stress versus strain curves by comparing mechanical properties obtained from these curves for tests in ionic solutions to similar mechanical properties from a test performed in air. These results are expressed in the form of an SCC index which is the quotient of the results from the environment of interest and that from an air test. Indices which are commonly used include U.T.S. index, reduction in area index, % elongation index and time to failure index. An index of less than unity indicates EAC effects and greater than unity a degree of protection offered by the solution. It is always necessary to verify the presence of absence of SCC effects fractographically.

4.3.6. Electrochemical Tests

An EG and G Princeton Applied Research Model 173 potentiostat was used for the free corrosion potential scans and in conjunction with an external automatic baseline advance for the potentiodynamic scans. The test specimen for these electrochemical tests is in the form of a 15.7mm diameter disc which is polished to a 0.25μm finish and is held in a specifically designed specimen holder which avoids the problem of crevice corrosion. The test specimen, counter electrodes, luggin capillary and the gas inlet are all housed in a standard design corrosion flask. For the standard scans a slow scan rate of $0.14mVs^{-1}$ was used. Before commencing the testing programme, the accuracy of the equipment was verified by performing a scan of AISI 430 in 1N H_2SO_4 according to ASTM Standard G5-78 (ASTM-1980) and comparing it with the ASTM reference curve. Good reproduceability was obtained.

Parkins[119], outlines a method using anodic polarization curves to provide reasonably accurate predictions of the critical potential ranges for SCC cracking in a given system. This procedure involves first scanning a range of potentials in the anodic direction at a relatively high scan rate (1000mV/min) to determine regions with a high current density in which intense anodic dissolution is likely. This is followed by a relatively slow scan (20mV/min) which indicates the regions in which relative inactivity is likely.

This concept rests on the hypothesis that the rapid scan minimises film formation so that the observed currents relate to film free conditions, whereas the slow scan allows time for filming to occur. Comparison of the two curves then reveals any ranges of potential within which high anodic activity in the film free region reduces to insignificant activity when the time requirements for film formation are met. This then indicates the critical potential range in which SCC is likely to occur.

CHAPTER 5

RESULTS

5.1 AIR TESTS:

The results of the air tests performed on 927 in the four material conditions are presented in Figure 5.1 and summarised in Tables 5.1 and 5.2. It can be gleaned from Figure 5.1 that the four material conditions exhibit rather different mechanical properties. The as-rolled material has a UTS of 1500 MPa and a 0.2 % proof stress of 1100 MPa with a 13-15 % elongation. SEM examination of the fracture surface (Figure 5.2) reveals a classical cup and cone fracture of the as-rolled material with well developed shear lips and a fully dimpled, ductile fracture surface.

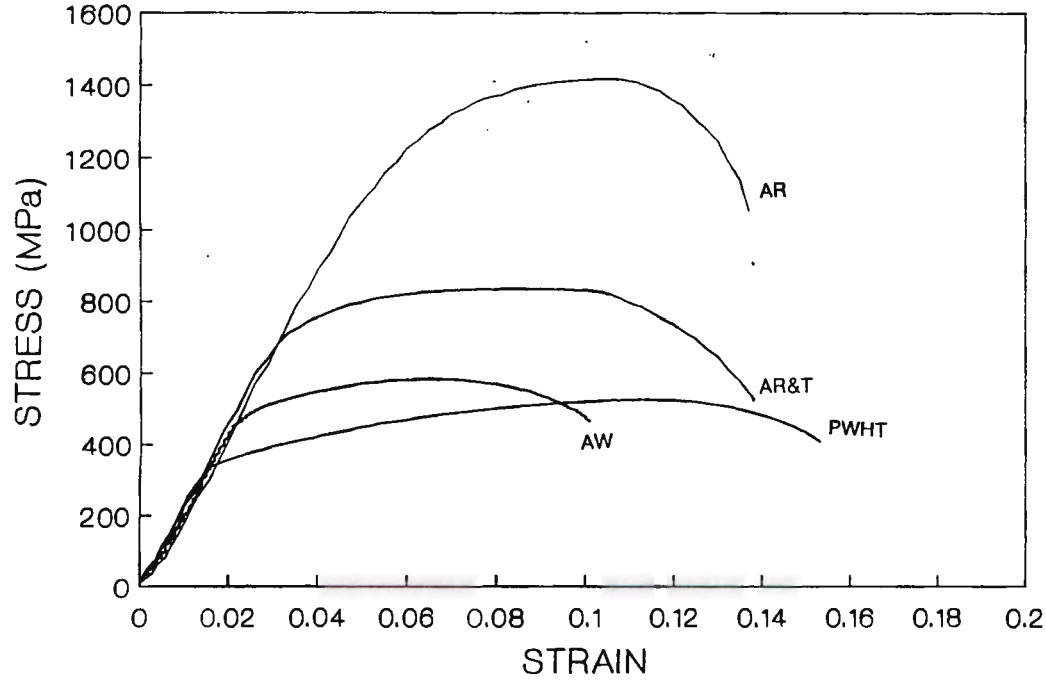

Figure 5.1: The SSR stress vs strain curves recorded in air for the as-rolled, tempered, welded and post weld heat treated materials.

Tempering of the material at 700°C for one hour has resulted in a reduction in the mechanical properties (UTS = 850 MPa, Y.S. = 700 MPa). SEM examination of the fracture surface (Figure 5.3) reveals a star-like fracture with secondary cracks radiating out from the specimen centre. Percentage elongation of the material however appears to be largely unaffected.

Test Condition	Time to failure (mins)	Strain at failure	Fracture Stress (MPa)	UTS (MPa)	Fractographical Evidence of SCC (YES/NO)
AS ROLLED					
AIR-T1	1526	0.124	989.1	1412	NO
AIR-T2	1643	0.140	944.6	1418	NO
Cl^--T1	1577	0.135	997.2	1454	NO
Cl^--T2	1589	0.138	971.8	1466	NO
SO_4^{-2}	1486	0.127	943.1	1425.5	NO
NO_3^-	1530	0.132	985.8	1451.6	NO
S.MINE-T1	1525	0.139	967.4	1470.7	NO
S.MINE-T2	1519	0.134	849.3	1391.7	NO
S.MINE-T1 (TRANS)	1507	0.135	994.9	1463.4	NO
S.MINE-T2 (TRANS)	1477	0.130	1062.8	1465.7	NO
-1200mV	788	0.059	1118.6	-	YES
-325mV	1596	0.129	927	1401.9	NO
+0 mV	1362	0.111	1044.3	1455.4	NO
+75 mV	853	0.065	1300.5	-	Y+N*
+150 mV	687	0.052	1090	1109.5	Y+N*
+230mV	457	0.033	320.9	474.1	NO
TEMPERED					
AIR-T1	1198	0.107	571.2	840.9	NO
AIR-T2	1683	0.138	531.8	847.7	NO
Cl^-	1484	0.136	536.3	846.2	NO
S.MINE-T1	1528	0.138	568.2	859.8	NO
S.MINE-T2	1452	0.129	518.5	836.4	NO
WELDED					
AIR-T1	1200	0.101	465	584	NO
AIR-T2	1547	0.132	532	603.2	NO
Cl^-	1295	0.116	484.6	562.8	NO
SO_4^{-2}	1220	0.103	496.9	561.8	NO
S.MINE-T1	1336	0.114	516.2	568.2	NO
S.MINE-T2	1485	0.133	496.9	561.8	NO
PWHT					
AIR-T1	1775	0.153	407.6	533.3	NO
AIR-T2	1982	0.166	457.5	547.2	NO
Cl^-	1542	0.136	469.7	537	NO
S.MINE-T1	1525	0.136	404	519.7	NO
S.MINE-T2	1455	0.129	408	536	NO

* Fractographical evidence of SCC in isolated areas on specimen fracture surface; gross reduction in mechanical properties is largely due to accelerated pitting corrosion at these anodic potentials and not to SCC mechanisms.

Table 5.1: The mechanical properties derived from the Stress vs Strain curves recorded during SSR testing.

Test Condition	Time to failure index	Strain at failure index	Fracture Stress index	UTS index	R in A index
AS ROLLED					
AIR-T1	1.00	1.00	1.00	1.00	1.00
AIR-T2	1.00	1.00	1.00	1.00	1.00
Cl^--T1	1.00	1.02	0.97	1.03	0.96
Cl^--T2	1.00	1.05	1.09	1.04	1.05
SO_4^{-2}	0.94	0.96	1.09	1.01	1.07
NO_3^-	0.97	1.00	1.08	1.03	1.04
S.MINE-T1	0.96	1.05	1.01	1.04	1.01
S.MINE-T2	0.96	1.02	0.91	0.98	1.03
S.MINE-T1 (TRANS)	0.95	1.00	1.03	1.03	*
S.MINE-T2 (TRANS)	0.93	0.99	1.10	1.04	*
-1200mV	0.50	0.45	0.63	-	0.44
-325mV	1.01	0.98	1.25	0.99	1.16
+0mV	0.86	0.84	1.08	1.03	*
+75mV	0.54	0.49	1.35	-	*
+150mV	0.43	0.39	1.13	0.78	*
+230mV	0.29	0.25	-	0.34	*
TEMPERED					
AIR-T1	1.00	1.00	1.00	1.00	1.00
AIR-T2	1.00	1.00	1.00	1.00	1.00
Cl^-	1.03	1.11	0.96	1.00	0.98
S.MINE-T1	1.06	1.13	0.91	1.02	0.93
S.MINE-T2	1.01	1.05	1.05	0.99	1.03
WELDED					
AIR-T1	1.00	1.00	1.00	1.00	1.00
AIR-T2	1.00	1.00	1.00	1.00	1.00
Cl^-	0.94	1.00	0.85	0.95	0.94
$S0_4^{-2}$	0.89	0.88	0.79	0.99	0.87
S.MINE-T1	0.97	0.98	-	0.96	*
S.MINE-T2	1.08	1.14	0.82	0.95	0.90
PWHT					
AIR-T1	1.00	1.00	1.00	1.00	1.00
AIR-T2	1.00	1.00	1.00	1.00	1.00
Cl^-	0.82	0.85	1.09	0.99	0.97
S.MINE-T1	0.81	0.85	1.19	0.96	1.09
S.MINE-T2	0.77	0.81	1.25	0.99	1.10

* Not measured

Table 5.2 : The SCC indices derived from the Stress vs Strain curves recorded during SSR testing.

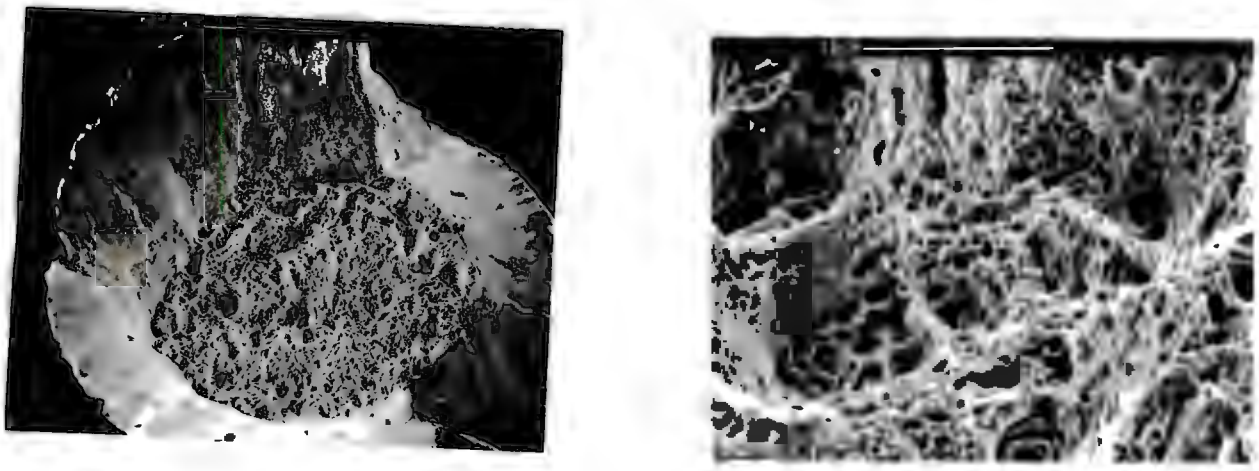

(a) (b)

Figure 5.2: The as-rolled material tested in laboratory air; (a) - general fracture surface illustrating the fully ductile cup and cone fracture; (b) - higher magnification showing the ductile, dimpled fracture surface.

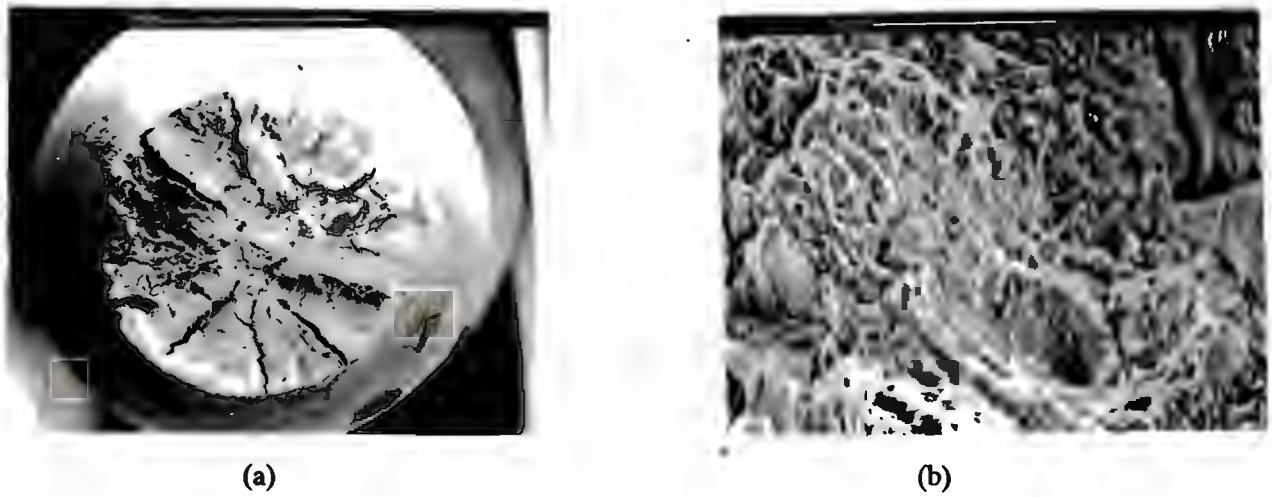

(a) (b)

Figure 5.3: The tempered material tested in laboratory air; (a) - overall fracture surface showing the star-like fracture morphology with the numerous radial secondary cracks; (b) - ductile trangranular fracture with reduced dimple size and the presence of secondary cracking.

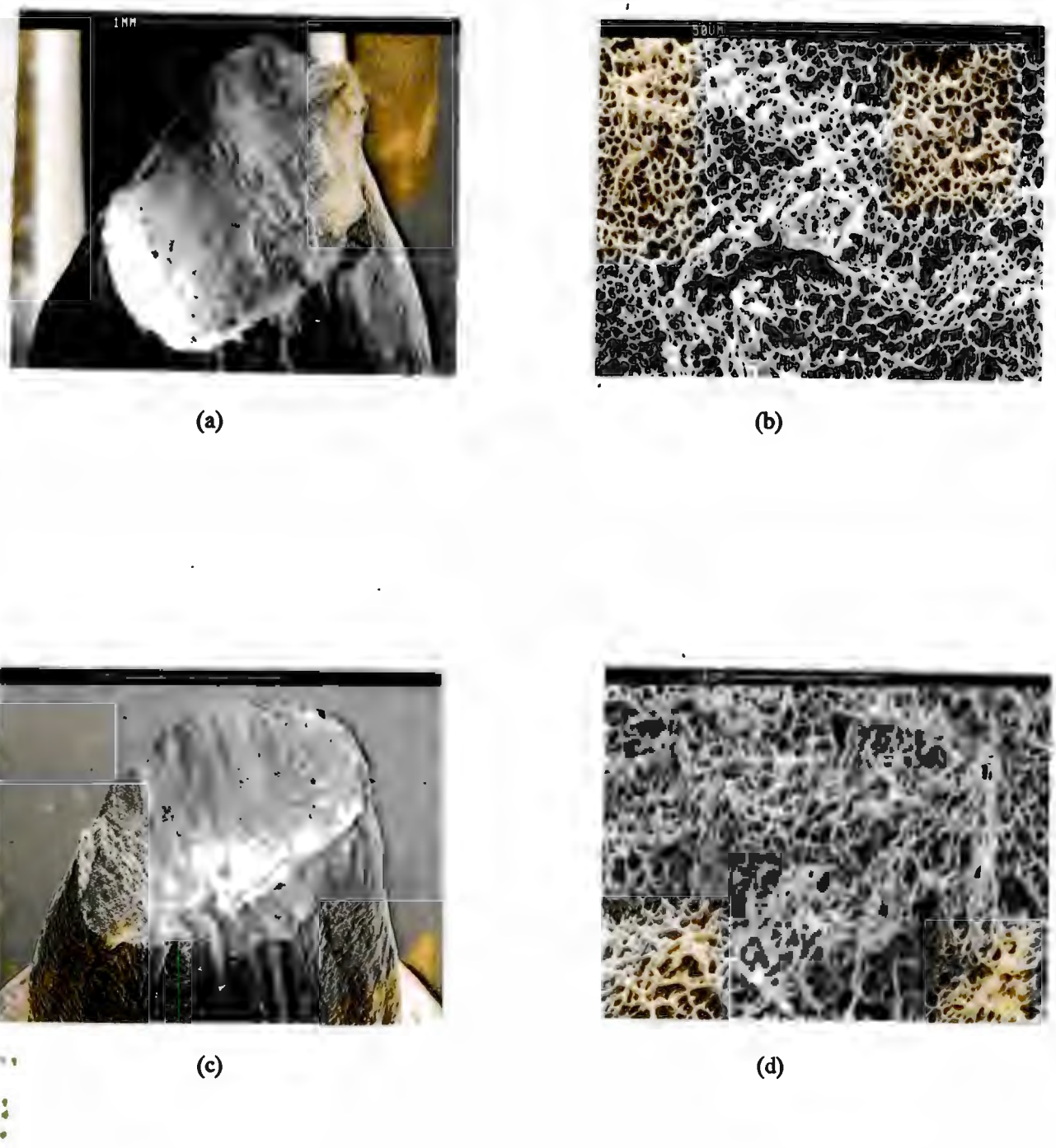

Figure 5.4: As welded and PWHT material tested in laboratory air; (a) - general fracture surface of the AW material; (b) - higher magnification showing fully ductile, dimpled fracture surface; (c) - general fracture surface of the PWHT material; (d) - ductile, dimpled morphology typical of the entire fracture surface.

The welded and post weld heat treated (PWHT) tensile specimens were machined with the weld line and associated HAZ in the gauge length. It is clear from Figure 5.1 that the welding and post weld heat treatment has led to a marked reduction in Y.S. and UTS, that of the PWHT material being lower than the welded material as would be expected. The ductility of the PWHT material has also been improved. The SEM micrographs of the fracture surfaces of the welded and PWHT samples are presented in Figure 5.4. It is evident from these micrographs that a large reduction in area has occurred and the fracture surfaces have a dimpled, ductile appearance without the well developed shear lip characteristic of the material in the as-rolled condition. Sectioning of the tensile specimens revealed that the fracture occurred in the softer, lower strength austenitic weld metal. Visible on the gauge length during testing for both the welded and PWHT material was a large plastic zone which extended along the entire area of weld metal in the gauge length as illustrated in Figure 5.5.

Figure 5.5: The large plastic zone that developed on the gauge length during straining of the AW and PWHT specimens.

5.2 EFFECT OF DIFFERENT IONS

5.2.1 As Rolled Material

5.2.1.1 Slow Strain Rate Test Results

Figure 5.6 shows the slow strain-rate stress vs. strain curves for the as rolled and quenched material tested in the various ionic aqueous solutions at free corrosion potential (Ecorr). The mechanical properties derived from these curves together with the associated SCC indices are given in

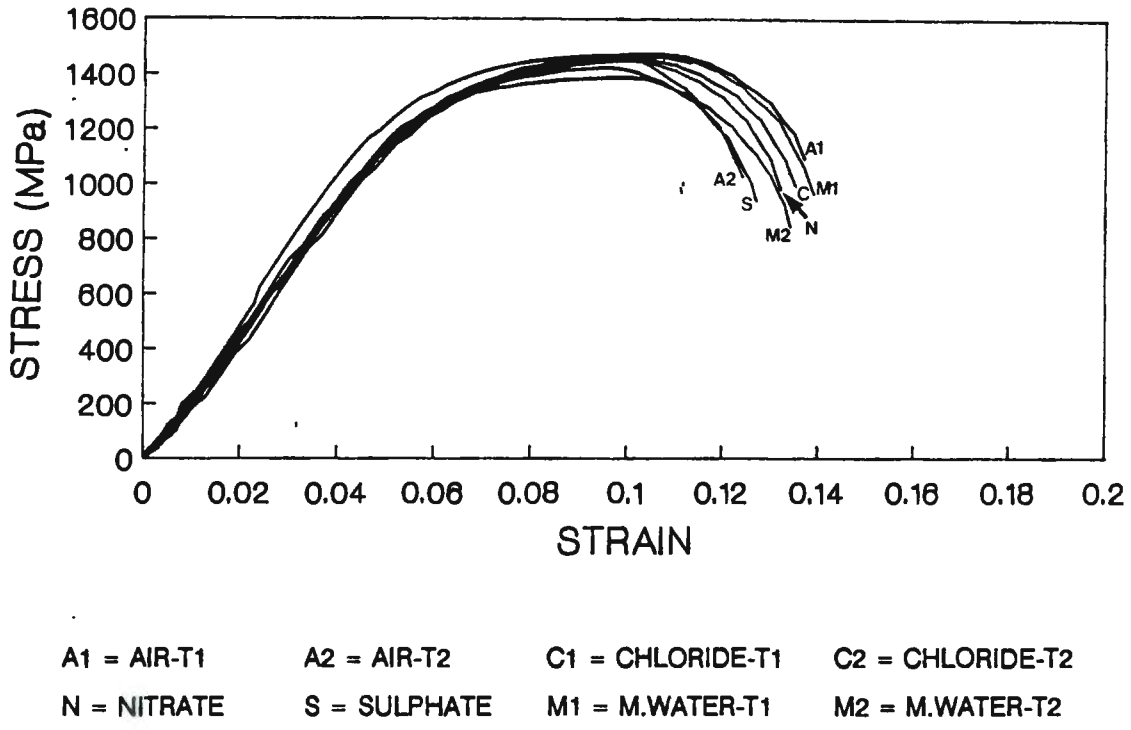

Figure 5.6: The SSR stress vs strain curves for the as-rolled material tested in the various aqueous environments at free corrosion potential.

Tables 5.1 and 5.2 respectively. It can be deduced from the indices in Table 5.2 that the material suffered no environmental embrittlement in the various solutions under the conditions of the test.

This is confirmed by the observation on Figure 5.6 that the slow strain-rate stress vs. strain curves for the two air tests embrace the results obtained for all the other environments. The apparent lack of SCC is further confirmed by SEM fractography. All the different ionic solutions yielded a similar fracture morphology of a well developed shear lip and a highly dimpled, ductile fracture surface.

The fractographs for the tests performed in the simulated mine water and the 1000 ppm chloride solutions are presented in Figure 5.7. Figure 5.7(c) shows a higher magnification of the ductile fracture surface illustrating the dimpled ductile nature of the surface and the spherical inclusions around which the dimpled have nucleated and grown during straining. There was no sign of environmentally assisted embrittlement which would have been manifested by a reduction in dimple size as compared with the air test. The relative sensitivity of the various SCC indices is shown in the form of a bar graph in Figure 5.8.

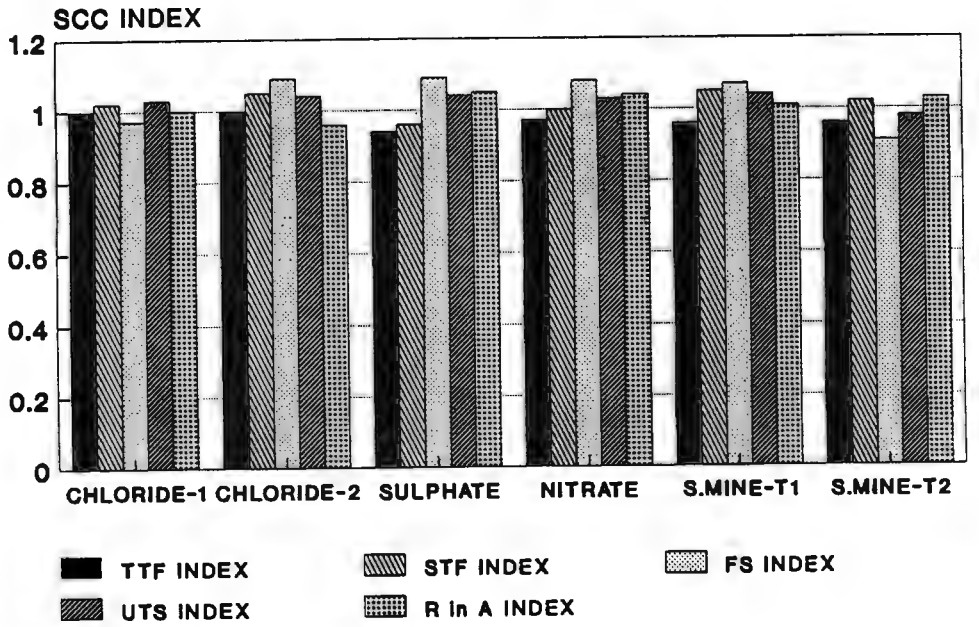

Figure 5.8: Bar graph showing the relative sensitivity of the various SCC indices.

5.2.1.2 Corrosion Data

The bulk surface free corrosion potentials were recorded during the slow strain-rate tests and are illustrated in Figure 5.9. The free corrosion potentials (Ecorr) for the 927 material in the mine

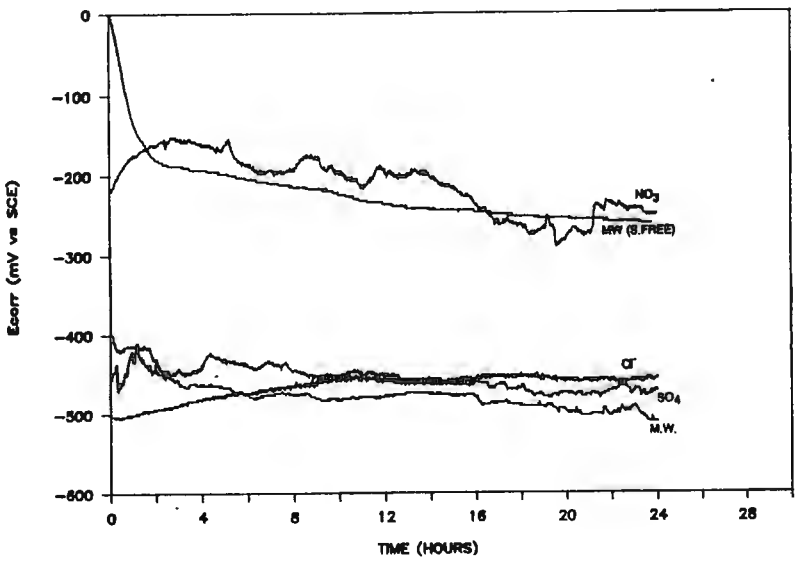

Figure 5.9: The fluctuation of the free corrosion potential with time as recorded during the SSR tests for the AR material. Also included for comparison purposes is the free corrosion potential in the simulated mine water recorded under strain free conditions.

water, sulphate and chloride solutions are similar, varying between -450 and -500 mV (vs. SCE). The Ecorr in the nitrate solution is somewhat more noble and less steady than that for the other solutions, varying between -180 and -280 mV. Also included on Figure 5.9 is the strain-free Ecorr time curve recorded for the material in the mine water by the method outlined in section 4.3.6. The straining appears to have pushed the bulk free corrosion potential in the active direction by about 300mV.

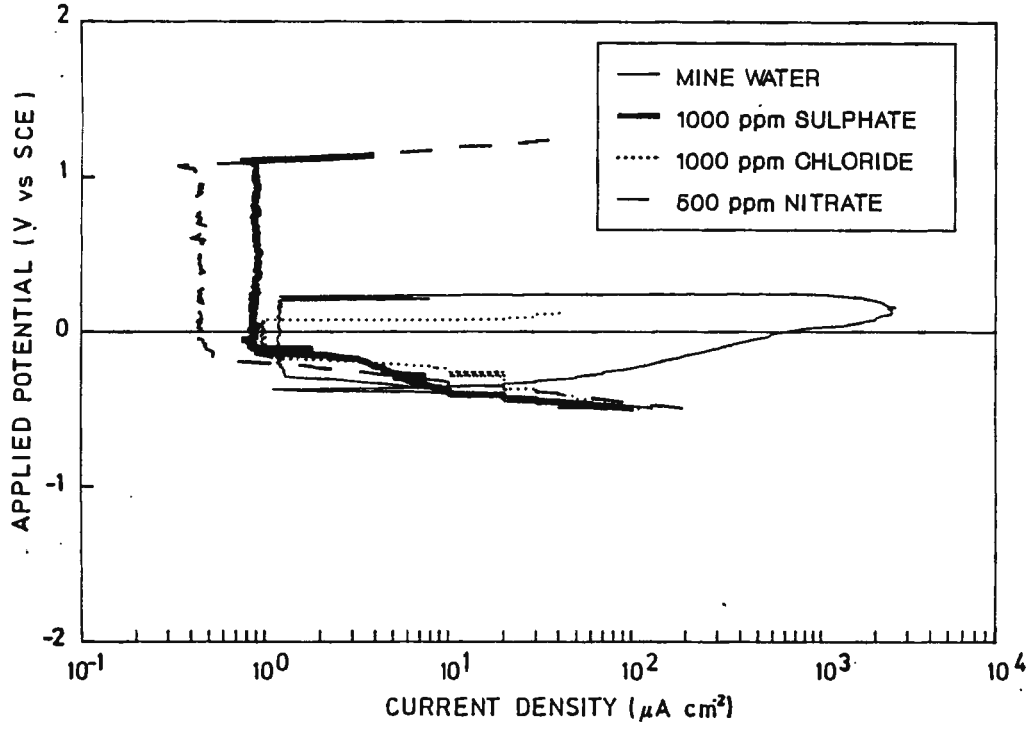

Figure 5.10: The potentiodynamic traces recorded for the as-rolled material in the various ionic solutions.

The results of potentiodynamic scans performed on 927 in the aqueous solutions of the ions of interest are presented in Figure 5.10. All the ions yielded traces which showed an absence of an active region and the associated Flade potential, the Ecorr value falling in the passive range of the material. Nitrate and sulphate were found to exert a strongly passivating influence on 927, producing similarly large passive potential ranges extending from -100 mV to +1100 mV. The passive current density of the nitrate solution is however slightly lower than that of the sulphate solution.

The detrimental influence of chloride ions on the passive oxide film in high chromium containing steels is illustrated by the much reduced passive potential range and the increased passive current density in this solution relative to the other solutions. The mine water, which is a combination of the above three solutions, exhibits the highest passive current density and a passive range which is a rough average of that for the other ions. The mine water scan has been reversed producing a hysteresis loop in what is termed a pitting scan. The scan is seen to close in the cathodic region

below Ecorr indicating the likelihood of pit growth and possible formation at free corrosion potential.

The pitted nature of the surface yielded by the scan in the mine water is illustrated in Figure 5.11. A relatively high density of 50 - 150 μm diameter pits is seen to uniformly cover the specimen surface.

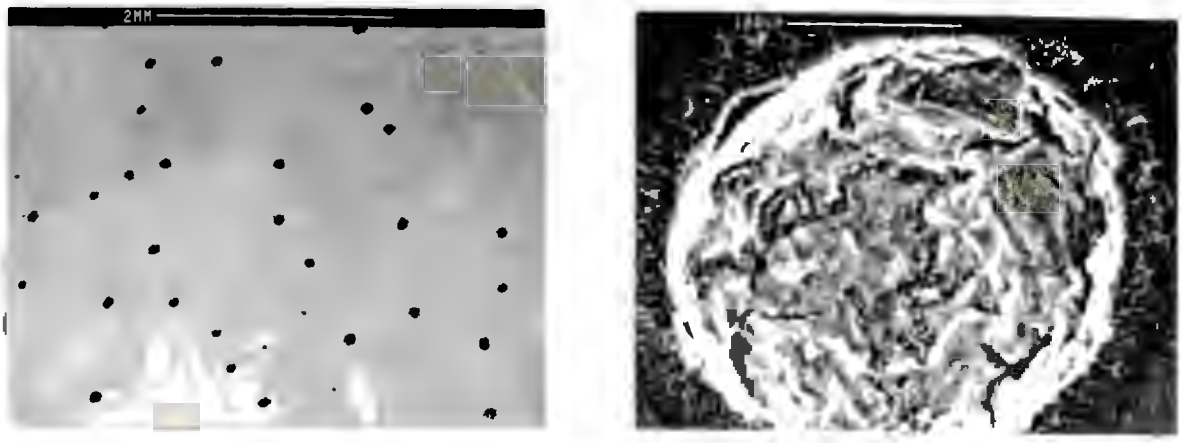

(a) (b)

Figure 5.11: The specimen surface of the as-rolled material after performance of a pitting scan in the simulated mine water solution; (a) - the general specimen surface showing the uniform pit distribution; (b) - higher magnification showing the pit morphology.

5.2.1.3 Impressed Potential Testing

The results of the fast scan (3.4 mVs^{-1}) and the slow scan (0.34 mVs^{-1}) performed on the material in the solution of primary interest viz. mine water are presented in Figure 5.12. From the figure it would appear as if the susceptible range is between 230 mV (Ebr) and -50 mV. Five tests were conducted spanning this potential range. In addition to this, two tests were undertaken at overpotentials of -1200 mV and -330 mV. The slow strain-rate stress strain curves for these tests are illustrated in Figure 5.13 and the mechanical properties are summarised in Tables 5.1 and 5.2.

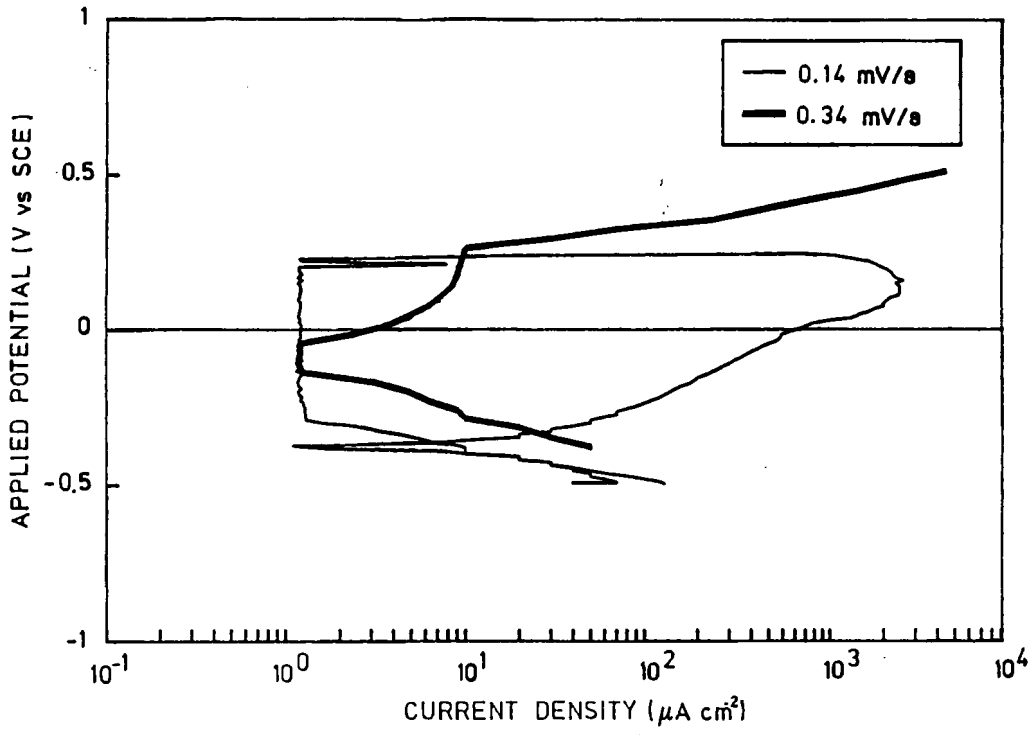

Figure 5.12: The fast and slow potentiodynamic scans performed in accordance with the method outlined by Parkins[119]. The potential ranges of SCC susceptibility are postulated to exist over those potentials where there is maximum separation between fast and slow traces.

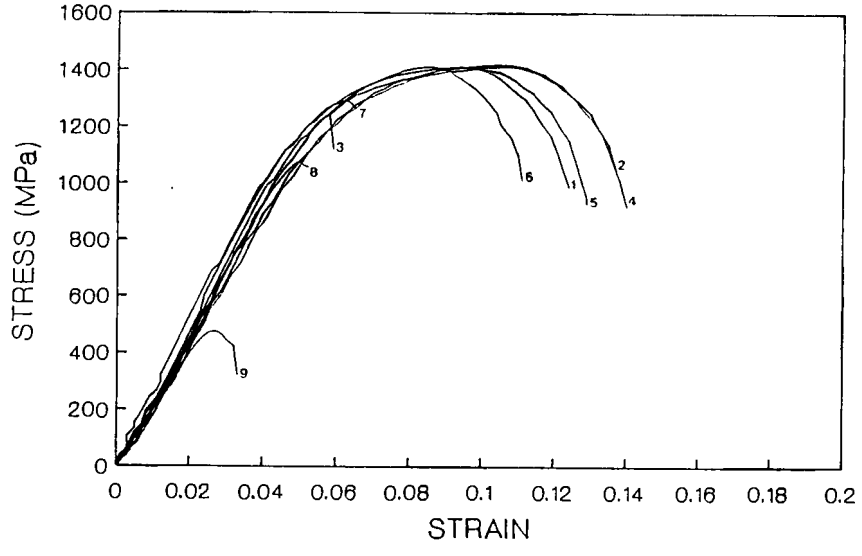

1 = AIR-T1 2 = AIR-T2 3 = -1200mV 4 = -480mV (Ecorr) 5 = -325mV
6 = 0mV 7 = 75mV 8 = 150mV 9 = 230mV

Figure 5.13: The SSR stress vs strain curves derived from the as-rolled material at impressed anodic and cathodic overpotentials.

i) +230 mV

This potential was selected because it is on the extreme position of the region of interest on Figure 5.12 and has the largest separation of current density between fast and slow scans. This potential proved to be too active however and extremely high anodic current densities (in the excess of 1A cm^{-2}) were recorded during the test. This resulted in the severe anodic dissolution of the specimen, the specimen ultimately failing because of reduction in load-bearing cross-section by large-scale pitting as shown by Figure 5.14. There appears to be a preferential corrosion of certain constituents producing a lineated morphology with possible orientation in the rolling direction (specimens were prepared with the gauge lengths in the direction of rolling).

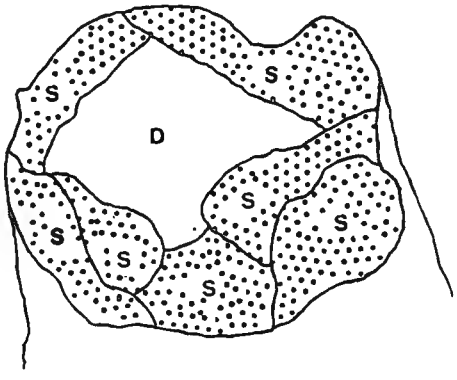

(a)

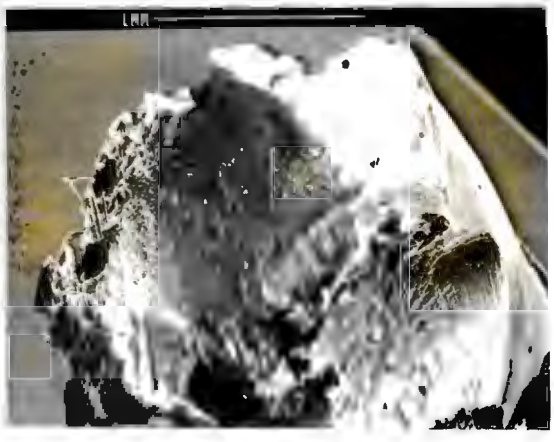

(b)

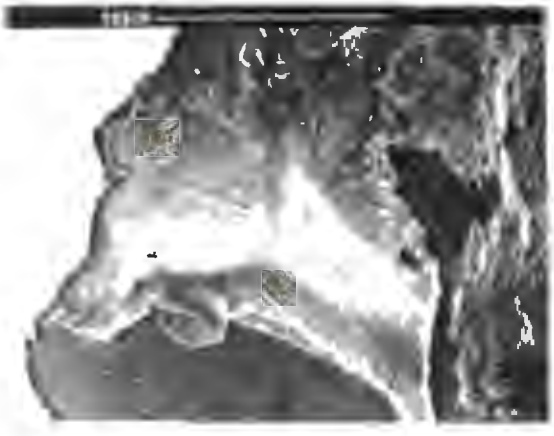

(c)

Figure 5.14: The specimen tested in the simulated mine water solution at the impressed anodic potential of +230mV; (a) - schematic of the fracture surface - D: dimples; S: striations; P: pit; (b) - general fracture surface showing ductile failure as a result of large scale pitting. A lineated morphology is evident in the pitted areas; (c) - higher magnification showing this lineated corrosion morphology.

ii) +150 mV

Testing at +150 mV yielded a large reduction in mechanical properties as shown in Figure 5.13 and Table 5.1. Numerous fine cracks were visible along the gauge length which upon examination proved to be corrosion pits with the same lineated preferential corrosion as the +230 mV sample. Again fracture was by reduction in load bearing capacity, in this case by the coalescence of three well developed corrosion pits as shown in Figure 5.15(b). The higher magnification of Figures 5.15(c) and (d) illustrate the existence of lower energy transgranular and intergranular fracture modes at the base of these two large pits. The intergranular fracture areas appear smooth and featureless other than for the occasional large dimple or tear ridge. The remainder of the pit surface is covered with the striated corrosion morphology. Numerous secondary cracks are also visible on the fracture surface.

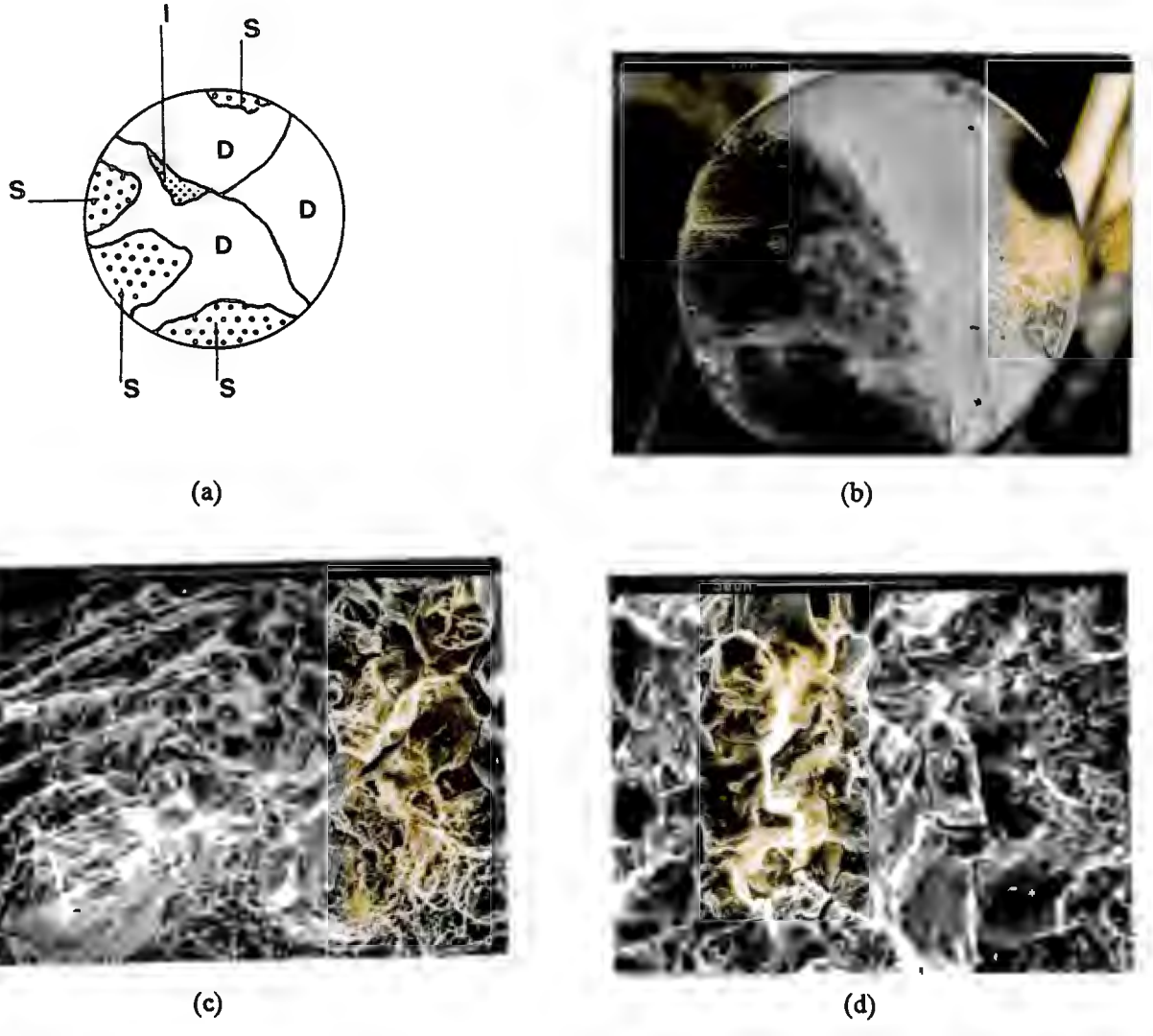

Figure 5.15: Specimen tested at +150mV in the simulated mine water solution; (a) - schematic of the general fracture surface - D: dimples; I: intergranular; T: transgranular; M: mixed trans and intergranular; S: striations (b) - general fracture surface. Lineated morphology again present on pit surfaces; (c) - mixed fracture mode at the base of the pit; (d) - higher magnification of this mixed fracture mode.

ii) +150 mV

Testing at +150 mV yielded a large reduction in mechanical properties as shown in Figure 5.13 and Table 5.1. Numerous fine cracks were visible along the gauge length which upon examination proved to be corrosion pits with the same lineated preferential corrosion as the +230 mV sample. Again fracture was by reduction in load bearing capacity, in this case by the coalescence of three well developed corrosion pits as shown in Figure 5.15(b). The higher magnification of Figures 5.15(c) and (d) illustrate the existence of lower energy transgranular and intergranular fracture modes at the base of these two large pits. The intergranular fracture areas appear smooth and featureless other than for the occasional large dimple or tear ridge. The remainder of the pit surface is covered with the striated corrosion morphology. Numerous secondary cracks are also visible on the fracture surface.

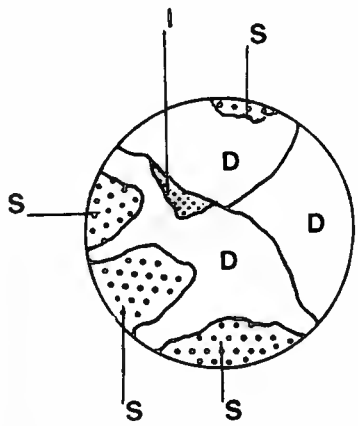

(a)

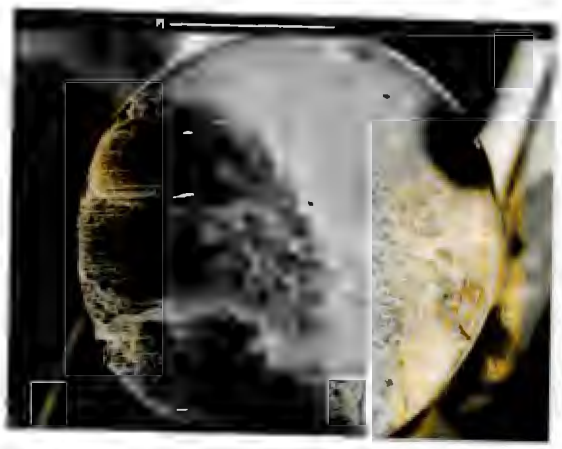

(b)

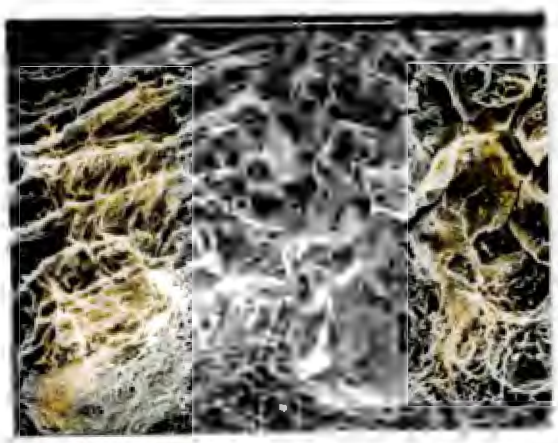

(c)

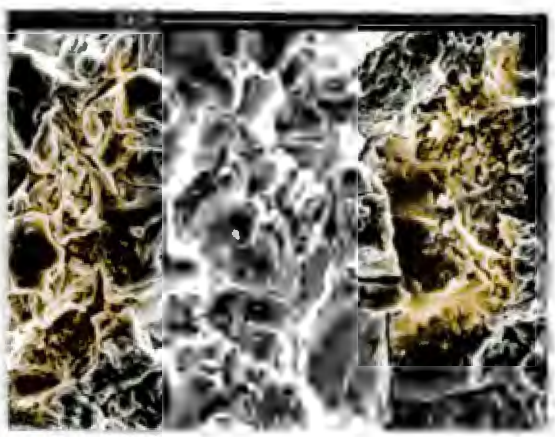

(d)

Figure 5.15: Specimen tested at +150mV in the simulated mine water solution; (a) - schematic of the general fracture surface - D: dimples; I: intergranular; T: transgranular; M: mixed trans and intergranular; S: striations (b) - general fracture surface. Lineated morphology again present on pit surfaces; (c) - mixed fracture mode at the base of the pit; (d) - higher magnification of this mixed fracture mode.

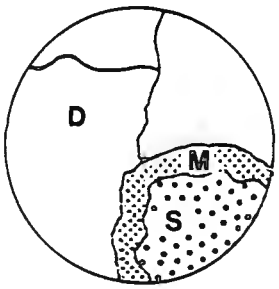

(a)

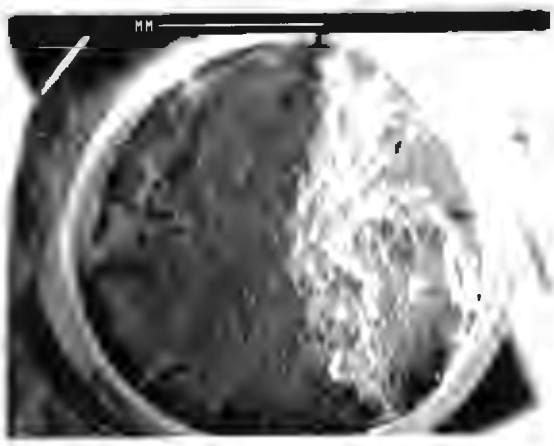

(b)

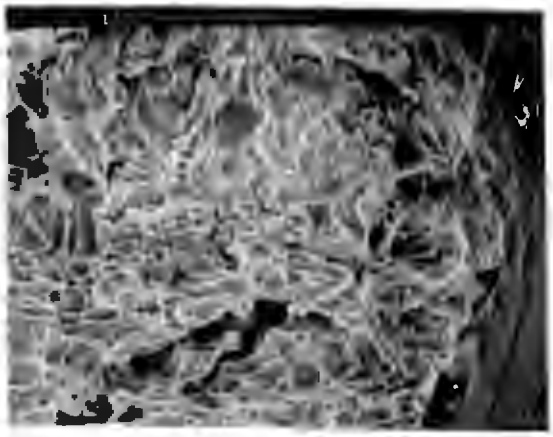

(c)

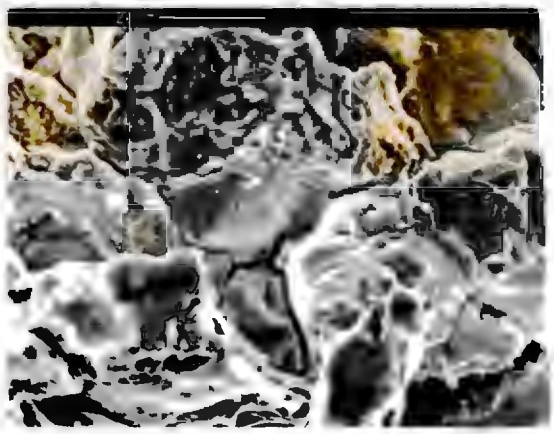

(d)

Figure 5.16: Specimen tested at +75mV in the simulated mine water solution; (a) - schematic of the fracture surface illustrating the relative positions of the various fracture modes; (b) - general view of the fracture surface illustrating the striated pit morphology; (c) and (d) - showing increasing magnification of this mixed fracture mode at the base of the pit.

iii) +75 mV

Testing at 75mV produced much the same results as polarisation at 150mV viz. several well develped pits propagating across the greater part of the cross-section with localised mixed transgranular fracture and intergranular separation at the base of these pits. A schematic of the overall fracture surface illustrating the relative positions of the various fracture modes is presented in Figure 5.16(a) and the mixed fracture modes evident at the base of the pits are shown in

Figures 5.16(c) and (d). The pitted areas of the fracture surface are distinguishable by the lineated corrosion morphology previously described. The existence of fewer small pits on the gauge length after testing indicates that the material is less vulnerable to localised corrosion and hence SCC initiation at this lower anodic potential. The results are reflected by the lower "SCC" indices at 150mV as opposed to 75mV.

(a) (b)

Figure 5.17: Specimens tested in the simulated mine water at impressed potentials of; (a) - 0mV; (b) - 325mV. Both fractures are fully ductile cup and cone.

iv) 0 mV

Testing at 0 mV produced perfectly ductile cup and cone fracture with a well developed shear similar to the air tests as illustrated in the SEM micrograph of Figure 5.17(a). There was no reduction in mechanical properties. The entire gauge length was however, covered with a thin layer of reddish brown oxide, probably haematite.

v) -330 mV

Testing at -330mV also resulted in a fully ductile cup and cone fracture as shown in Figure 5.17(b). No corrosion products were visible on the gauge length.

vi) -1200 mV

As might be anticipated cathodic polarization of this high strength alloy to extreme potentials in the order of -1200mV (SCE) resulted in severe hydrogen embrittlement. During testing bubbles of

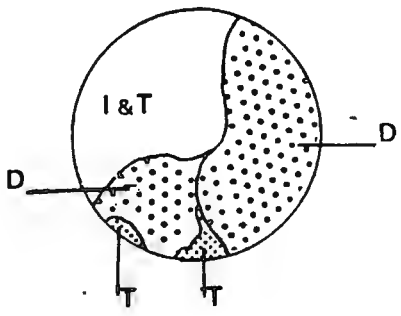

(a)

(b)

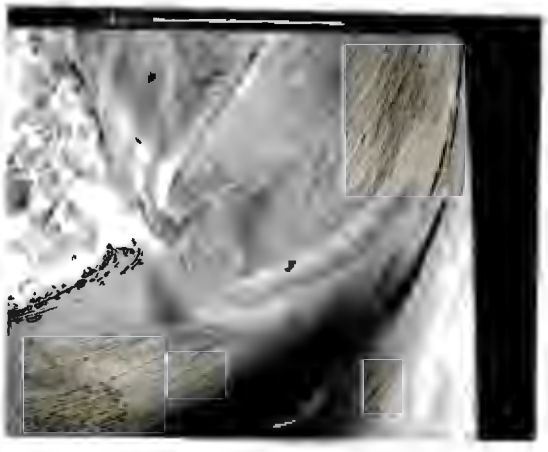

(c)

Figure 5.18: Specimen tested at -1200mV in the simulated mine water solution; (a) - schematic of the fracture surface mapping the locations of the various fracture modes; T: transgranular; I: intergranular; M: mixed; D: dimples; (b) - SEM micrograph of the general fracture surface showing the reduced ductility. Marked on the micrograph are the locations of the various fracture modes illustrated overleaf; (c) - secondary cracks extending along the gauge length.

what was probably hydrogen gas was observed to be slowly forming on and evolving from the specimen surface. This extreme polarization resulted in approximately a 50% reduction in mechanical properties as shown in Table 5.7. SEM examination (Figure 5.18(b)) revealed that the HAC initiated on several fronts simultaneously and propagated inwards to reduce the load bearing area before final fast fracture of the remaining cross-section. Fig 5.18(c) shows the existence of numerous secondary cracks extending from the fracture surface for appreciable distances along the gauge length. Numerous partially propagated cracks were also visible along the gauge length indicating marked reductions in ductility along the greater part of the gauge length.

SEM fractography revealed no consistent hydrogen fracture mode. Fracture modes observed included transgranular interlath fracture, intergranular separation and dimpled ductile failure with reduced dimple size as illustrated in Figure 5.19. Intergranular separation along prior austenite grain boundaries appeared to be the dominant fracture mode.

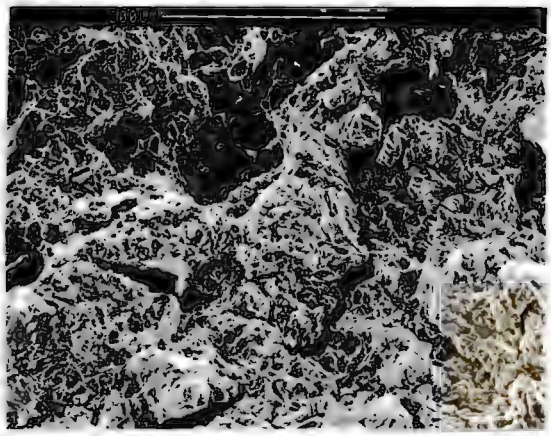

(a)

(b)

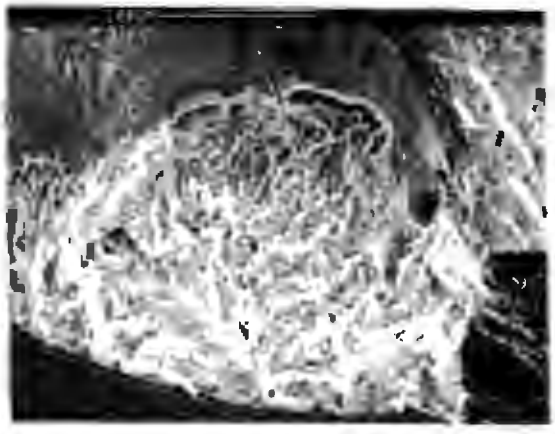

(c)

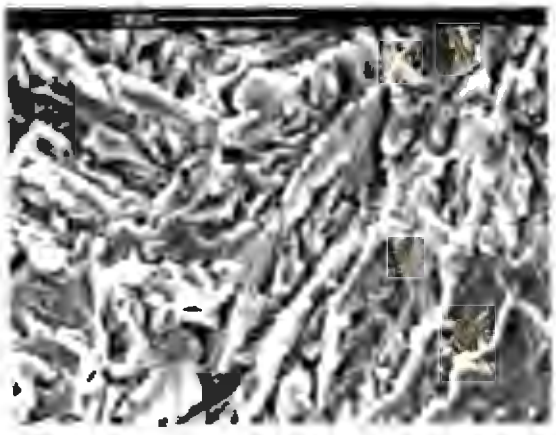

(d)

Figure 5.19: Mixed fracture modes exhibited by the specimen tested at -1200mV in the mine water solution. The locations of the fractographs on the specimen fracture surface are illustrated in Figure 5.18(b); (a) - general view showing mixed fracture mode with numerous secondary cracks; (b) - HE in the form of reduced dimple size; (c) - transgranular interlath crack propagation; (d) - higher magnification of the interlath fracture mode. This fracture mode is rather typical of high strength martensitic steels exposed to a hydrogen environment.

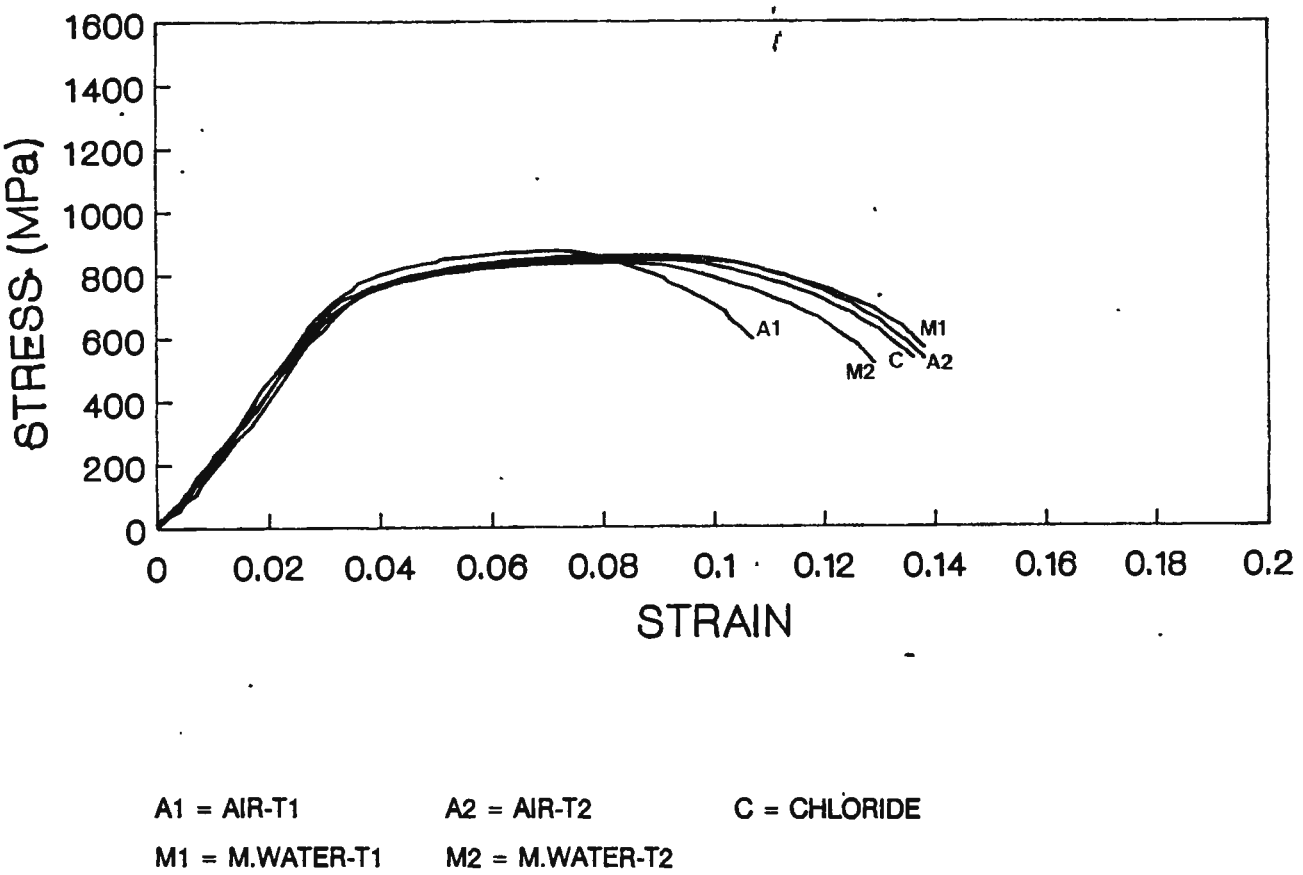

Figure 5.20: SSR stress vs strain curves for the tempered material in the various aqueous environments.

5.2.2 Tempered (700 °C - 1 Hour)

5.2.2.1 Slow-Strain Rate Test Results

The slow strain-rate stress vs. strain curves of Figure 5.20 indicate an absence of SCC effects in the various ionic solutions used in the investigation. Tables 5.1 and 5.2 give the mechanical properties derived from these curves together with the related SCC indices. The small variation in indices reflects the lack of SCC quantitatively. SEM examination of the fracture surfaces failed to show any signs of environmentally assisted embrittlement over and above the embrittlement introduced by the tempering heat treatment. All the fracture surfaces of the tempered material exhibited the star-like morphology with numerous secondary crack parallel to the tensile direction. The fracture surfaces of the tests conducted in 1000 ppm chloride and the simulated mine water are illustrated in Figure 5.21.

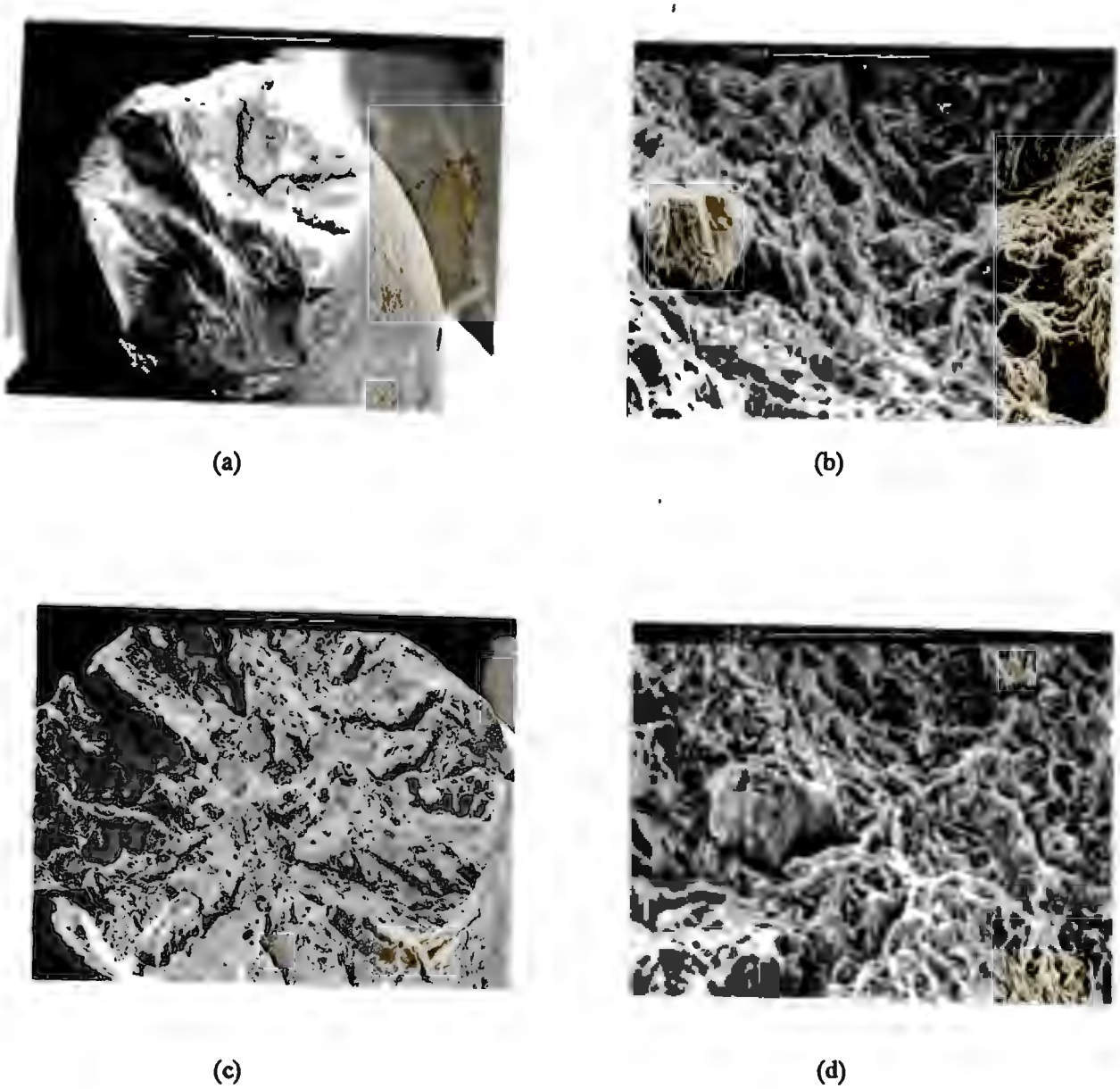

Figure 5.21: Fracture surfaces of the tempered material tested in the aqueous environments at rest potential; (a) - 1000ppm Cl^- ; - general fracture surface; (b) - higher magnification showing reduced dimple size; (c) - simulated mine water - general fracture surface; (d) - higher magnification showing transgranular, ductile failure.

5.2.2.2 Corrosion Data

Figure 5.22 shows that the free corrosion potential recorded during the slow strain rate test appears to be more noble in the chloride solution (-450 mV) than in the mine water (-560 mV). Also included on Figure 5.22 is the strain free Ecorr vs. time plot for the mine water solution which is again more noble than the strained Ecorr-time plot. Comparison of the Ecorr-time

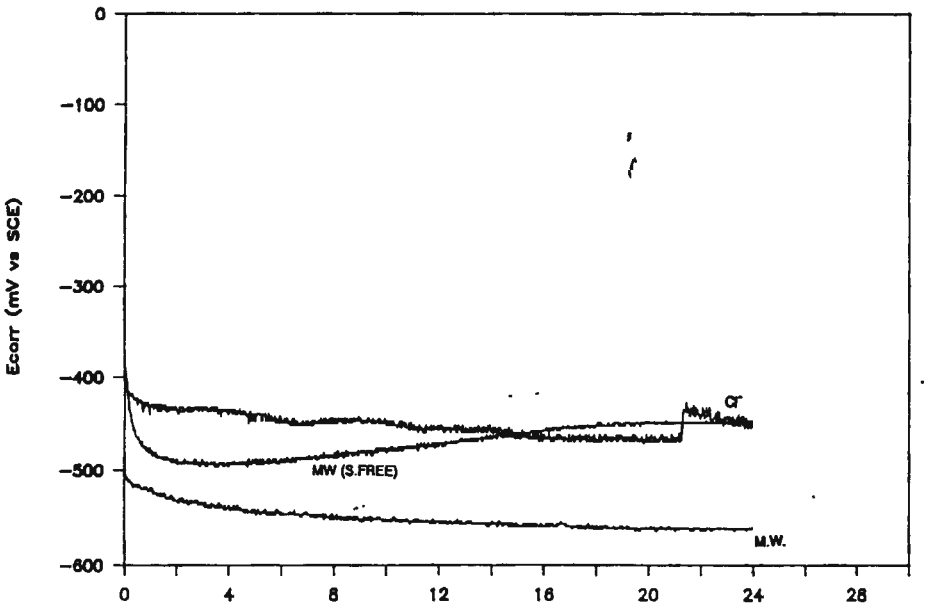

Figure 5.22: Free corrosion potential recorded during the SSR test for the tempered material. Included on the diagram is the strain free Ecorr scan recorded in the simulated mine water solution.

recorded during SSR testing for the as-rolled material (Figure 5.9) and the tempered material (Figure 5.22) reveals a similarity in the stabilised Ecorr-time values for the common test environments. Figure 5.23 shows graphically the free corrosion potential as a function of time recorded in the simulated mine water solution for the AR and the AR&T material conditions. Both the free corrosion potentials recorded during SSR testing (strained Ecorr) and those recorded under strain free conditions are presented for purposes of comparison. From the graph it can be seen that the tempering treatment has led to a reduction in Ecorr under both strain and strain free conditions as might be anticipated. In both material conditions however, the straining action has resulted in a shifting of the free corrosion potential in the active direction relative to strain-free conditions.

The form of the potentiodynamic polarization curves of the tempered material in the various environments (Figure 5.24) closely resembles that of the as-rolled material (Figure 5.10), other than for slightly reduced passive potential ranges in all the environments, especially the nitrate and sulphate solutions. The tempering treatment has not led to marked deteriorations in the corrosion properties of the material.

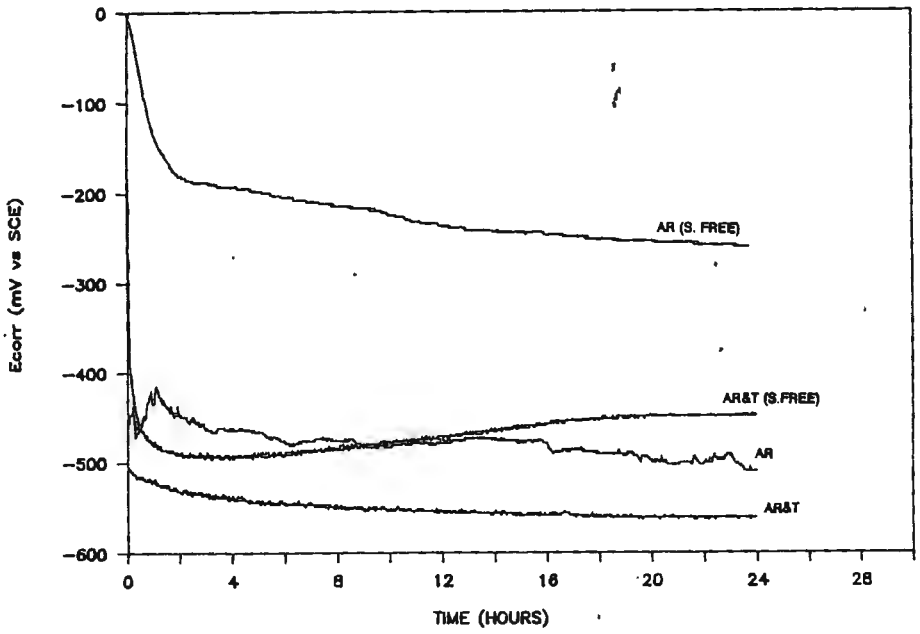

Figure 5.23: The free corrosion potential recorded during SSR testing (Ecorr strained) and that recorded under strain-free conditions for the AR and AR&T material conditions in the simulated mine water solution.

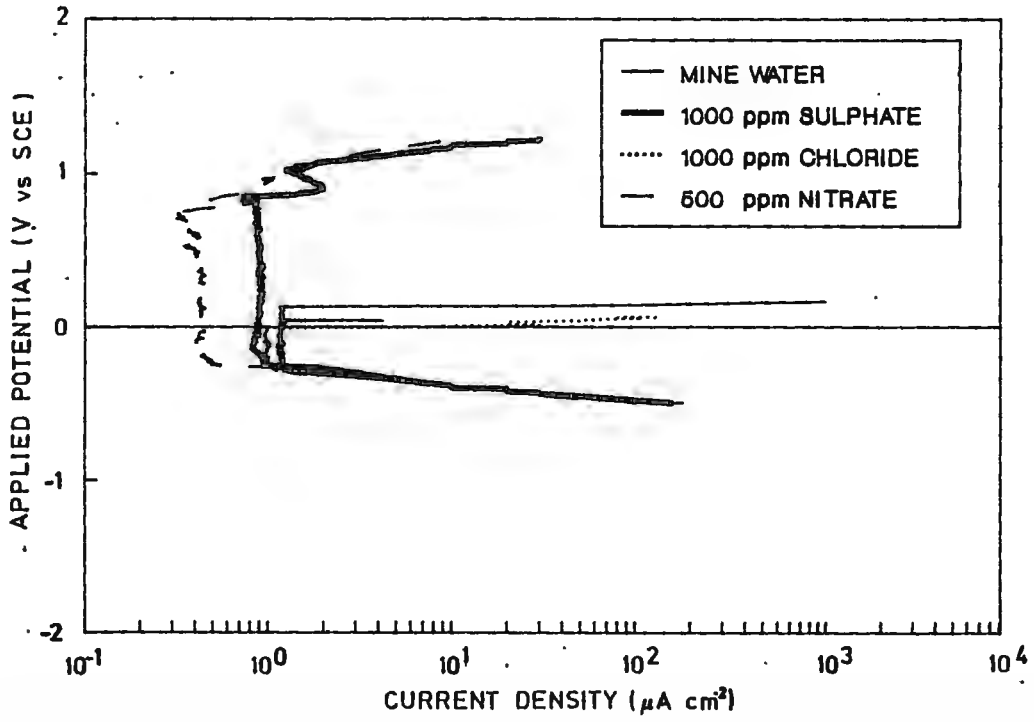

Figure 5.24: The potentiodynamic traces of the tempered material in the various aqueous environments.

5.2.3 Welded Material

5.2.3.1 Slow Strain Rate Test Results

The slow strain-rate stress vs. strain curves derived during testing are presented in Figure 5.25. The absence of environmentally assisted cracking is evident from the small fluctuation in mechanical properties of the stress strain curves of Figure 5.25. Similarly to the as-rolled material, the results for the different environments are enclosed by the results for the two air tests, indicating the lack of SCC. The mechanical properties from these curves together with the SCC indices derived from these properties are presented in Tables 5.1 and 5.2. The extremely high ductility and softness of the weld metal is responsible for the high strain to failure, reduction in area and the low UTS in comparison to the as-rolled material. In all the tests final fracture occurred in the weld metal in a fully ductile manner as confirmed by SEM examination which revealed fully ductile, dimpled fracture surfaces. Micrographs of the fracture surfaces of the tests in simulated mine water and 1000ppm chloride are illustrated in Figure 5.26.

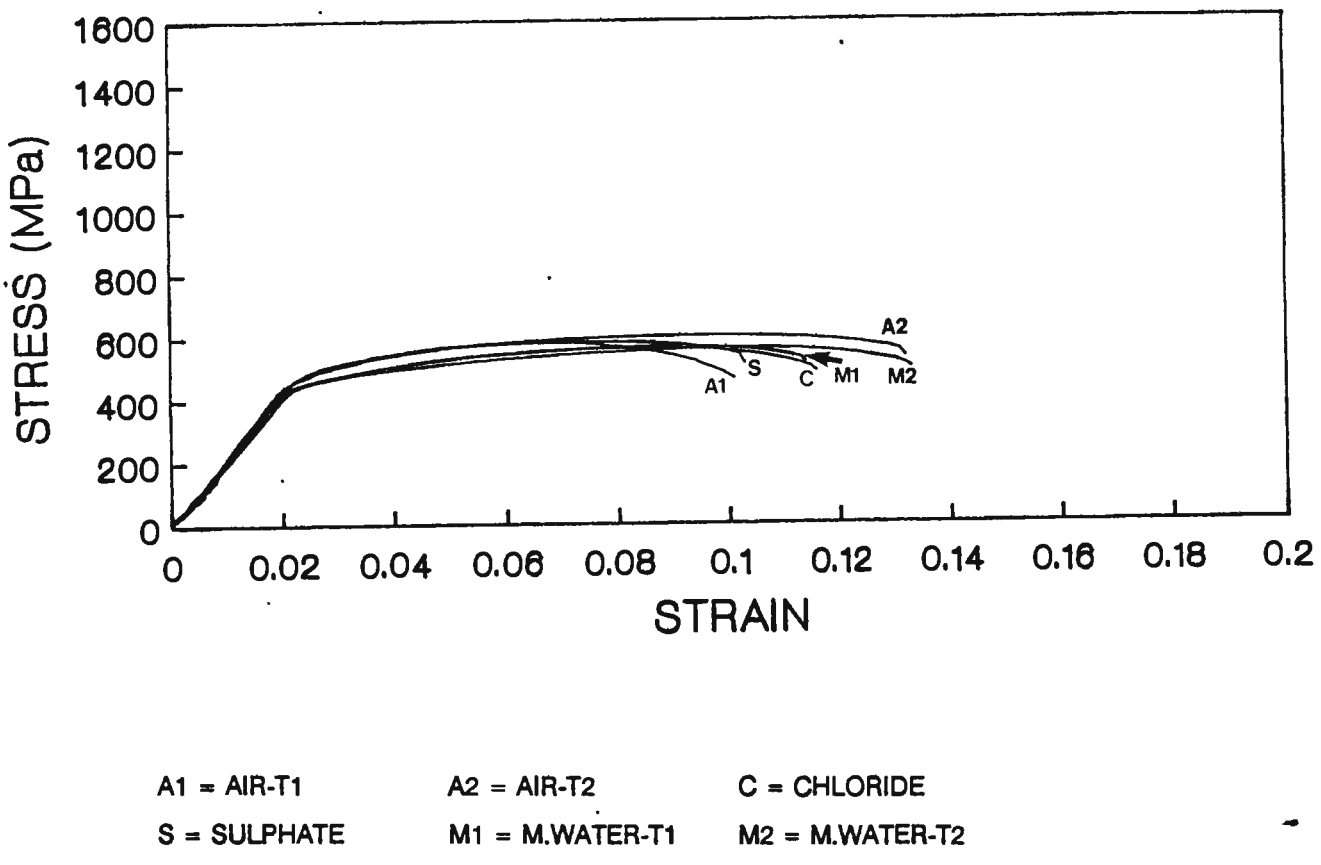

Figure 5.25: The SSR stress vs strain curves for the as welded material in the various aqueous environments at free corrosion potential.

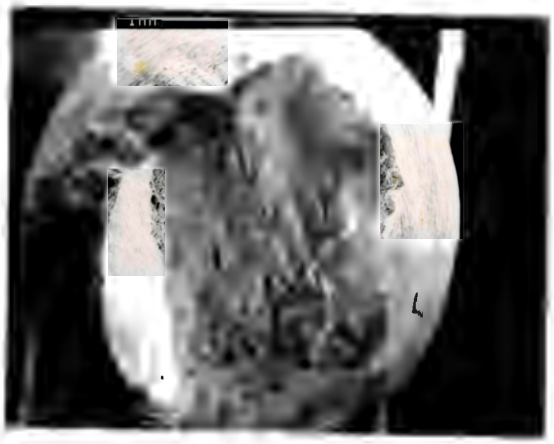

(a)

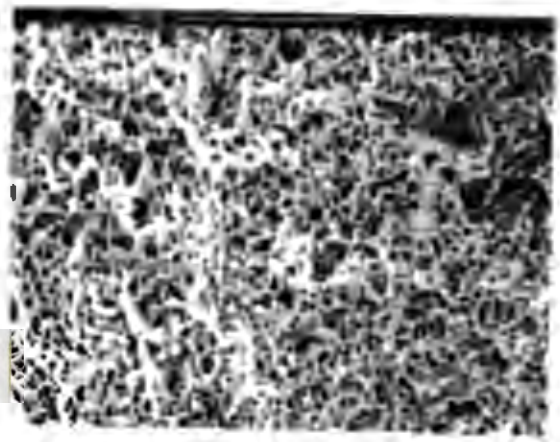

(b)

(c)

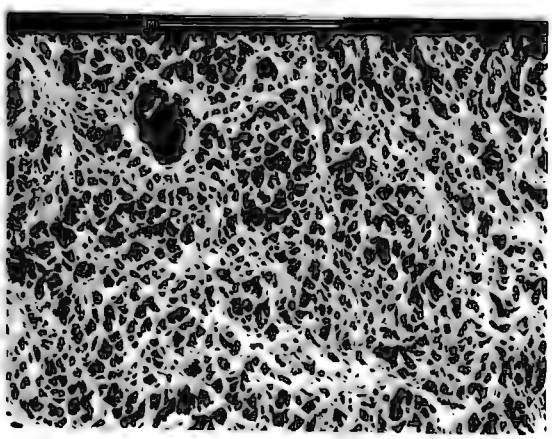

(d)

Figure 5.26: The fractographs of the as welded material tested at rest potential; (a) - 1000ppm Cl^- - general fracture surface, (b) - higher magnification showing ductile nature; (c) - simulated mine water - general fracture surface; (d) - higher magnification showing the ductile voids characteristic of the entire fracture surface.

5.2.3.2 Corrosion Data

Figure 5.27 shows the Ecorr-time curves for the welded material in the different solutions recorded during the slow strain rate tests. The welded material appears to become more active with time in all the solutions, stabilising after about twelve hours. The free corrosion potential varies from an active potential of -550 mV in the sulphate solution to a more noble potential of -400 mV in the chloride solution, the Ecorr in mine water being between these two values at -480 mV. The strain free Ecorr-time plot of the pure weld metal and the fusion zone (weld metal and parent metal combination) is also shown on the diagram for comparitive purposes. Again the dynamic straining has resulted in a reduction in the free corrosion potential by approximately 300mV relative to the strain free Ecorr value. As might be anticipated, the AISI 304 weld metal exhibits a more noble Ecorr than the combination by virtue of its higher chromium content. This is important from the point of view that most of the dynamic straining during SSR testing is seen to be concentrated in the softer austenitic weld metal and hence the corrosion properties of the weld metal will be of paramount importance in the SCC behaviour of the material in the as-welded condition.

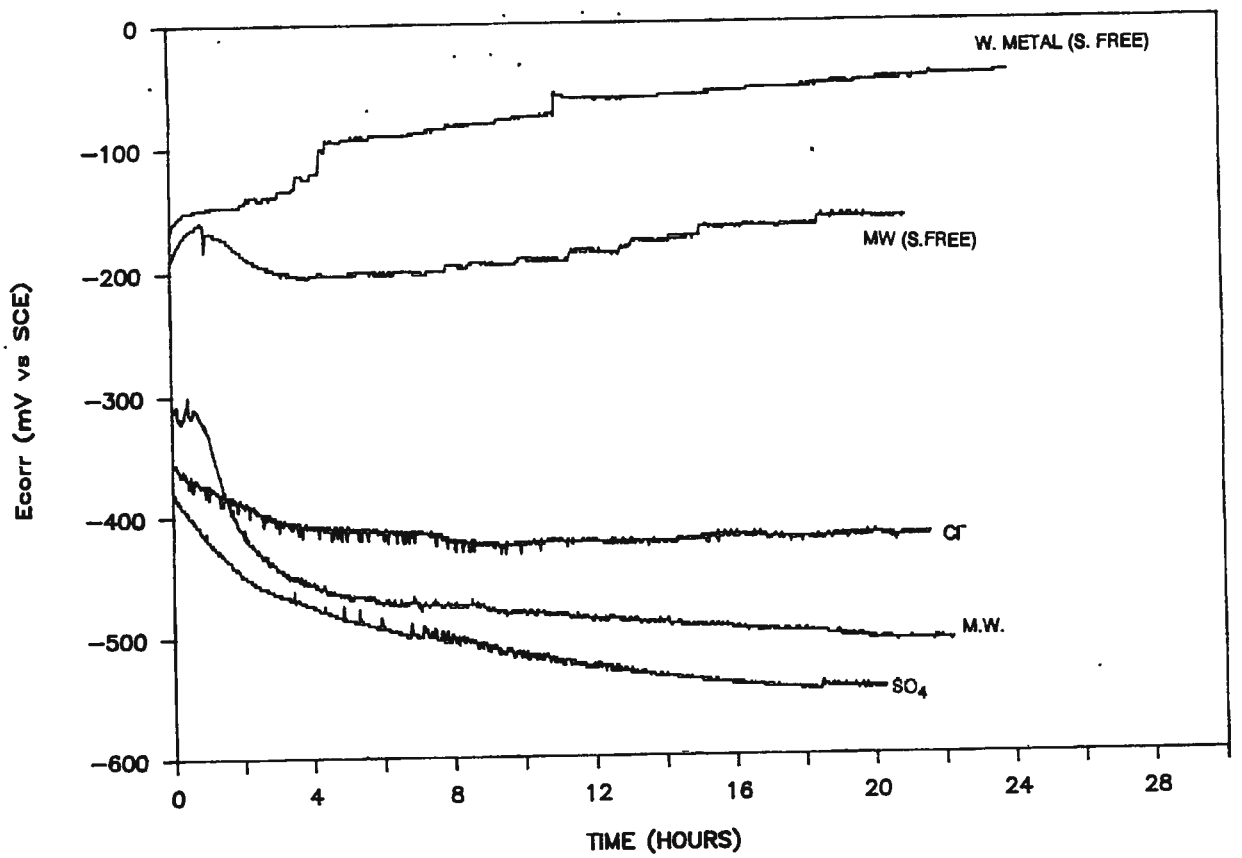

Figure 5.27: Free corrosion potential recorded during SSR testing for the as-welded material in the aqueous environments. Included on the graph are the strain-free free corrosion potentials recorded for the fusion zone (parent material and weld metal combination) and the pure weld metal.

5.2.4 Post Weld Heat Treated Material

5.2.4.1 SSR Results

The slow strain-rate tensile curves for the PWHT material are shown in Figure 5.28 and the mechanical properties derived from these curves together with the associated indices are given in Tables 5.1 and 5.2. Again an absence of environmentally assisted cracking is evidenced by the small variation in the SSR stress vs. strain curves for the different environments as compared to the air tests.

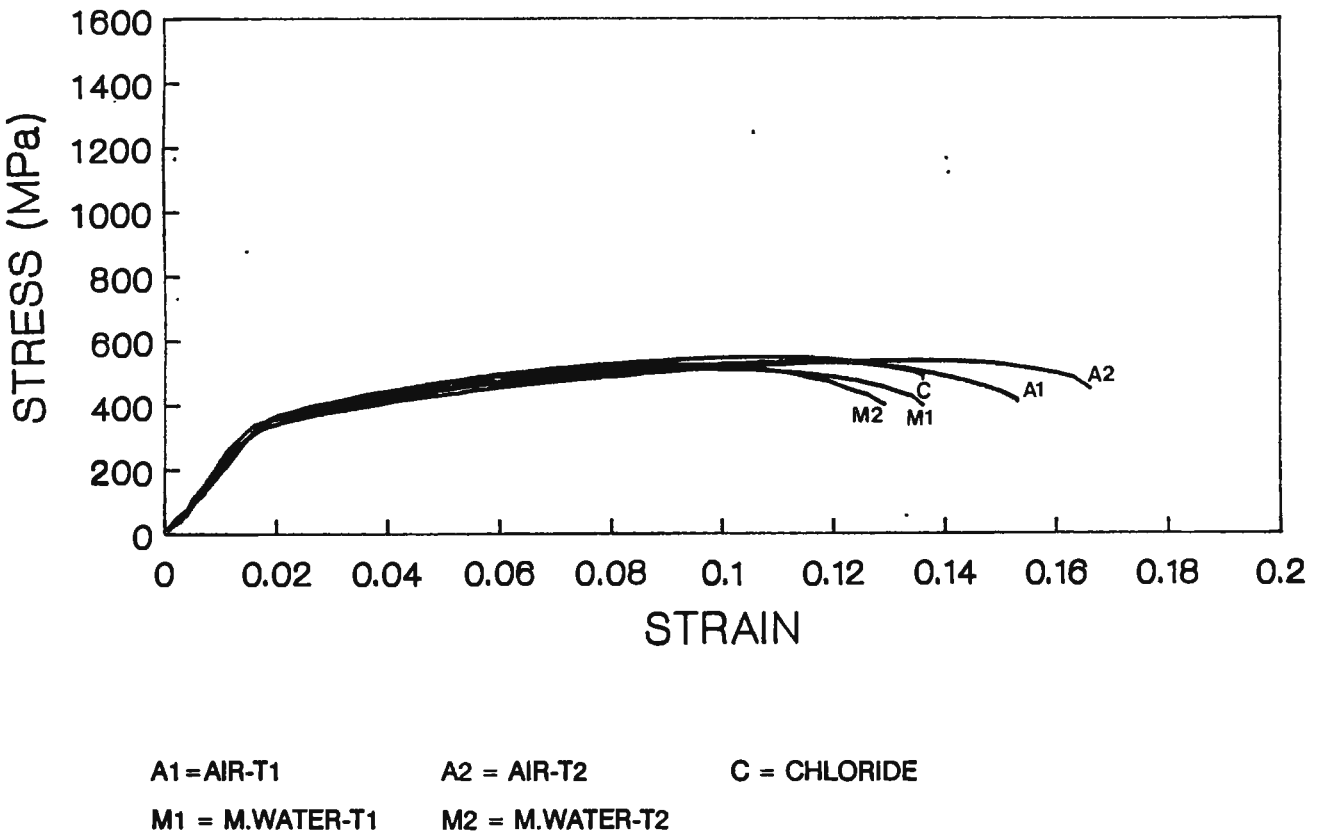

Figure 5.28: The stress vs strain curves derived from the SSR tests of the PWHT material in the various aqueous environments at open circuit potential.

This absence of SCC is confirmed by SEM examination which reveals a fully dimpled, ductile fracture surface for all the specimens. Figure 5.29 shows the fracture surfaces for the tests conducted in the chloride and mine water solutions respectively. All the specimens fractured, as in the case of the as-welded material, in the softer, lower strength austenitic weld metal after having undergone a large reduction in area.

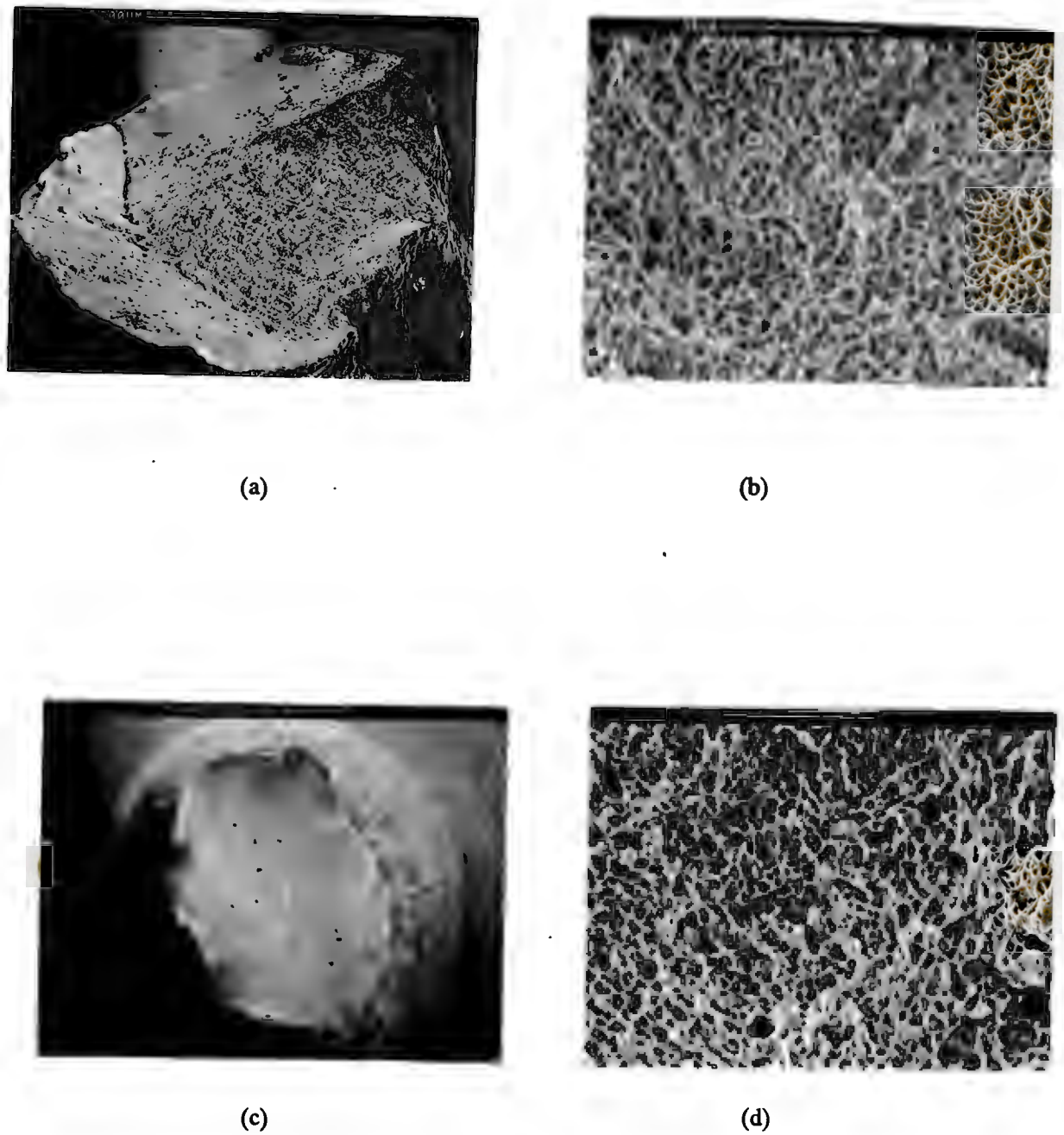

Figure 5.29: SEM fractographs of the PWHT material tested at free corrosion potential; (a) - general fracture surface in 1000ppm Cl^-; (b) - higher magnification showing the ductile, dimpled fracture surface; (c) - simulated mine water-general fracture surface; (d) - higher magnification of the dimpled morphology characteristic of the entire fracture surface.

5.2.4.2 Corrosion Data

The Ecorr vs. time plots recorded in the different environments during the slow strain-rate tests for both the welded and PWHT material are presented in Figure 5.30 for comparison purposes. It can be seen that the stabilised free corrosion potential behaviour of the PWHT material is essentially the same as that of the welded material in the common environments. Figure 5.31 shows the free corrosion potential recorded during straining as a function of time for all the material conditions in the simulated mine water solution. The graph indicates that the stabilised Ecorr value for all the material conditions other than AR&T is similar viz. -480mV, whereas the tempering treatment has led to a reduction in the Ecorr value by about 70mV. It would appear that the tempered material condition has the least corrosion resistance as might be anticipated.

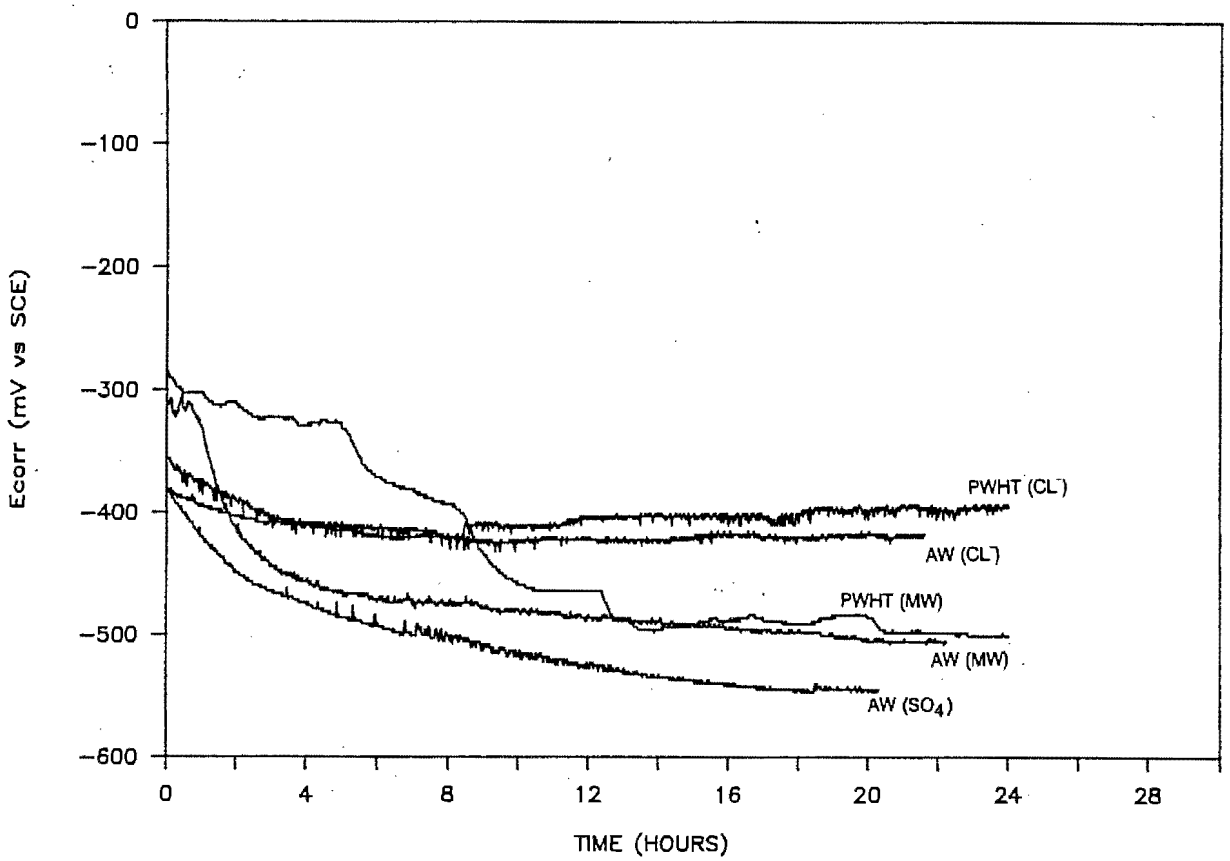

Figure 5.30: Free corrosion potential recorded during the SSR tests for the AW and PWHT material in the various aqueous environments.

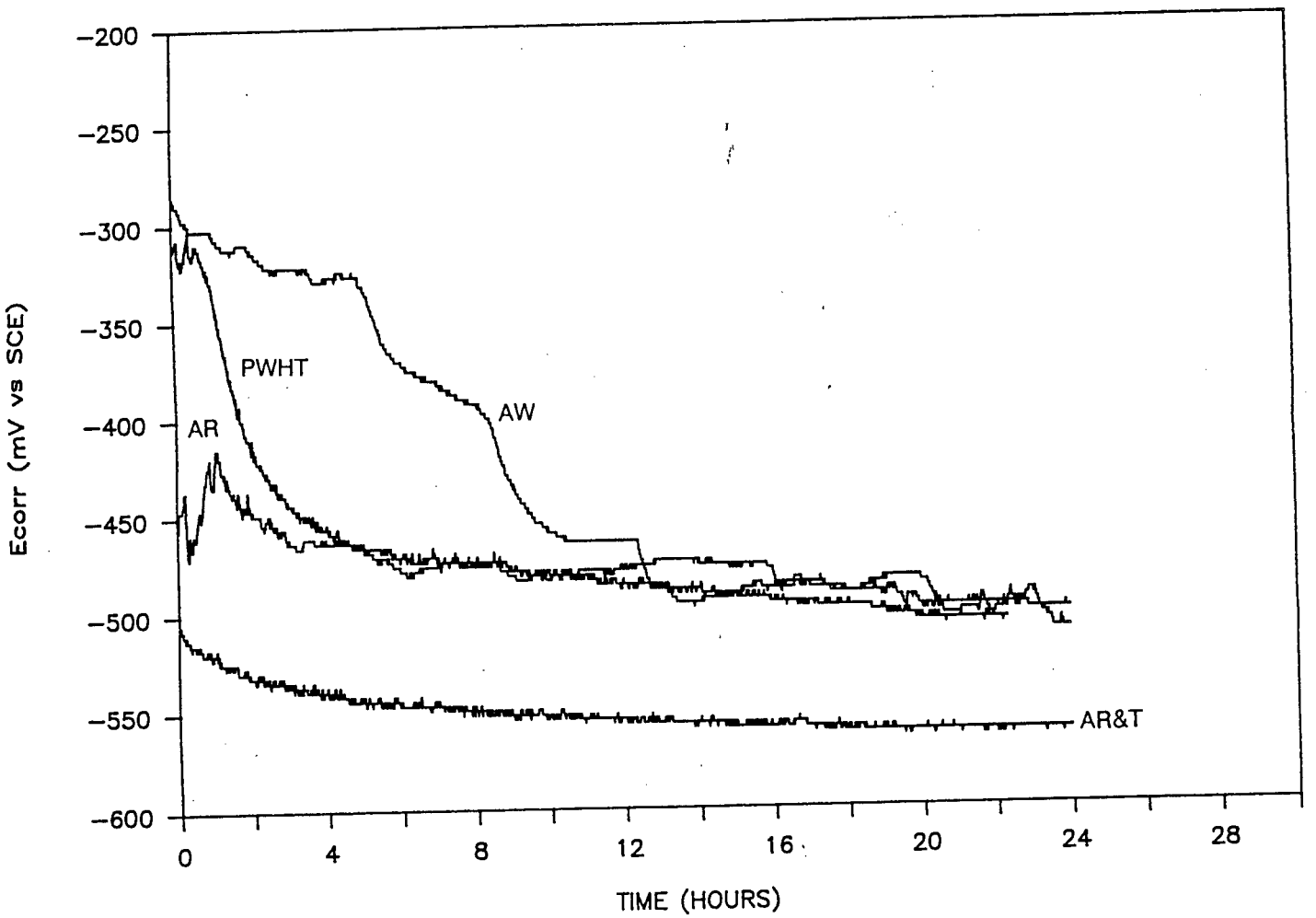

Figure 5.31: The free corrosion potential as a function of time recorded during SSR testing in the simulated mine water solution for all the material conditions.

CHAPTER 6

DISCUSSION

6.1 AS ROLLED 927 IN AQUEOUS ENVIRONMENTS

6.1.1 Free Corrosion Potential Testing

6.1.1.1 Electrochemical Observations

i) Ecorr Time

The potential transients or "noise" evident on the Ecorr-time curves recorded during the tests are indicative of passive film rupture during the SSR test. The corrosion potential becomes more active upon rupture owing to the exposure of fresh metal. This is followed by passivation. This occurs repetatively throughout the duration of the test owing to the constantly induced localised creep at the surface or crack tip characteristic of the SSR test. Mom et-al[121] cited a drop in the electrode potential during the SSR test which was observed to correspond with the onset of plastic deformation. They attributed this electrode potential drop to film rupture processes and the resultant creation of active surfaces at slip steps. A more or less constant value of electrode potential was noted over the following stage of the test. This was explained in terms of the effect of newly formed film free surface being compensated for by the repassivation of earlier formed active surfaces. A large drop in potential was observed which was found to correspond to crack initiation in specimens that exhibit SCC or in the case of specimens that are immune it corresponded to ductile rupture during the final stages of the test. The electrode potential reached a minimum when the specimen broke and a maximum of active surface area was exposed to the test solution. As this newly exposed area became passivated, the electrode potential returned to its value before the test. The trend of the free corrosion potential recorded during SSR testing of 927 largely follows that described by Mom et al.

The stabilised free corrosion potential recorded under strain free conditions can be seen to be 300 mV more noble than that recorded during the SSR test as shown by Figure 5.9. This might be expected on account of the reasoning adopted above viz. an electrode potential drop as a result of film rupture processes and the creation of active surfaces during the SSR test, a situation which is absent during the strain free rest potential testing.

ii) Potentiodynamic Polarisation Curves

The potentiodynamic polarisation curves of Figure 5.10 derived for 927 in the various ionic solutions used in the testing programme exhibit the same general morphology viz. an absence of an active loop with the free corrosion potential located in the passive potential range. It is well known that the Ecorr value is dependent on the oxidising species concentration, an increase causing the Ecorr value to move in the noble direction. It is for this reason that most polarisation scans run on stainless steels in aerated solutions do not show an active to passive transition since the cathodic curve intersects the anodic curve in passive region above the active to passive transition.

It is evident from the figure that the passive potential range in the sulphate and nitrate solutions (both are 1200mV) is far larger than that in the chloride (260mV). The passive potential range in the simulated mine water appear to be a compromise between that for the three constituting ionic concentrations viz. 520mV. The simulated mine water however exhibits a higher passive current density than any of the constituting ionic solutions. Cotterrel et al[122] investigated the pitting resistance of various corrosion resistant steels, including AISI 431, in synthetic mine waters consisting of permutations of chloride, sulphate and nitrate ions at pH values of 3.8 - 9.4. The authors showed that the addition of both sulphate and nitrate to chloride solutions increases the pitting resistance of AISI 431 steel. The authors, however, proceeded to demonstrate that the interactive effects of various types of ions on pitting corrosion differ from alloy to alloy and cautioned against predicting the pitting behaviour of another alloy without experimental verification.

The inhibitive effect of sulphate and nitrate ions as well as the aggressive effect of the chloride ion on stainless steels have been extensively documented by Leckie and Uhlig[123]. These effects have been explained in terms of the so-called adsorbed ion displacement models[124]. In terms of the model anionic species eg. Cl^-, SO_4^{-2}, NO_3^- are adsorbed onto the passive film either singly or in groups and compete with the oxygen in the passive film. At a sufficient concentration, corresponding to the critical pitting potential, these ions destroy the passive layer at favoured sites by displacing the adsorbed oxygen ions. The competitive adsorption theory explains the inhibitive influence of OH^-, SO_4^{-2} and NO_3^- ions in terms of these ions adsorbing into the passive layer displacing chloride. For pitting to initiate, the anodic overvoltage then has to be increased beyond the value which is required to induce pitting prior to the addition of the inhibitive ions i.e. the passive potential range is increased. This explains the larger passive potential range in the mine water relative to the 1000ppm chloride solution. The large passive potential ranges for the nitrate and sulphate solutions without the addition of the chloride ion is explained in terms of these ions being far less aggressive to the passive film when adsorbed in preference to oxygen, thus requiring far larger overpotentials to initiate pitting.

It is important to consider the electrochemical tendencies of the material to pit as the development of an occluded cell via pitting is the most likely method of SCC initiation on these smooth specimens in the absence of bulk embrittlement by hydrogen charging. It is clear from an examination of the the Ecorr vs time curves of Figure 5.9 and the potentiodynamic polarisation curves of Figure 5.10 that both the strain and strain free stabilised Ecorr values are remote from the breakdown or pitting potential. In general it is true to say that the larger the potential range between Ep and Ecorr, the higher the resistance of an alloy to pitting corrosion[125]. Therefore if Ecorr is close to Ep, pitting may occur owing to small increases in the oxidising power of the solution raising the free corrosion potential above Ep. In the case of 927 this is unlikely in all solutions other than the chloride solution.

The result of a pitting scan in the main solution of interest viz. the simulated mine water is illustrated in Figure 5.10. The scan closes in the cathodic region which means that any pits that are generated at Ecorr by local concentrations in anodic activity pushing Ecorr in the noble direction, are likely to continue to grow irrespective of the potential. This is important from the point of view of SCC initiation on the smooth tensile specimens used in the investigation. Examination of the surfaces of the specimens after conducting the polarization scans to breakdown revealed that all the ionic solutions, other than the nitrate solution, induced breakdown by localized pitting. The alloy broke down transpassively in the nitrate solution. The pitting was most well developed in the simulated mine water solution, the surface being uniformly covered with large well developed pits having a size ranging between 100 and 150μm as illusrated in Figure 5.11. Polarisation in the sulphate solution induced similar, but smaller pits having a size range of 5-40μm. The chloride solution in contrast resulted in large sparsely distributed pits.

The resistance to pitting of 927 is partially as a result of the molybdenum content of the alloy (0.7 wt %). It is well known that for a given chromium content of an alloy, the addition of molybdenum has a strong beneficial influence on passivity[125]. Molybdenum moves the pitting potential in the noble direction thereby extending the passive potential range. Marshall and Burstein[126] investigated the effect of molybdenum on repassivation kinetics by comparing the repassivation behaviour of AISI 304 and 316. They found that molybdenum aided the dissolution of the iron component of the oxide film during repassivation causing the oxide film to become chromium enriched more rapidly than in its absence. The authors then concluded that the constructive dissolution process accelerates the onset of passivity and improves the resistance to chloride induced pitting corrosion. Grobler et al[9] when evaluating several experimental melts during the development of 927 in a $FeCl_3$ immersion pitting test found molybdenum to exert a marked influence on the resistance to pitting corrosion. They concluded that a decrease in chromium content from 12% to 9% could be favourably compensated for by nickel and molybdenum additions. The validity of this conclusion is borne out by the good electrochemical

test results obtained for 927 in this investigation.

From the results of the corrosion tests it can be said that the likelihood of pitting at free corrosion potential is remote in all the test solutions over the short duration of the SSR test. This is on account of the appreciable separation between Ecorr and Ebr in all the solutions. The chances of pitting are highest in the chloride and simulated mine water solutions. However, should pits initiate in the simulated mine water solution, they are likely to propagate.

6.1.1.2 Slow Strain Rate Test Results

Examination of the slow-strain rate stress vs strain curves of Figure 5.6 shows that the results for the various ionic solutions are enclosed by the results for the two air tests. This serves to illustrate rather unambiguously the immunity of the material to SCC under the conditions of the test. All the test results lie within the realms of material scatter. Sprowls[127] in his review on the evaluation of SCC data points out the importance of recognizing the presence of a great deal of inherent variability in the results of SCC tests and the hazards associated with trying to base comparisons upon small differences in SCC susceptibility criteria.

The results of the SEM fractography are consistent with the previous findings viz. an absence of any environmentally reduced ductility. All the specimens displayed similar fracture surfaces consisting of large dimples surrounded by well developed shear lips i.e. classical cup and cone failure. The fracture surfaces were closely examined for variations in average dimple size as a possible indication of embrittlement, but none were detected.

It is reasoned that the apparent immunity of the as-rolled material to SCC under the test conditions is strongly related to the difficulty in initiating SCC at free corrosion potential on these smooth, plain test specimens over the relatively short duration of the SSR test for the reasons outlined in 6.1.1.1. This was confirmed by examination of the specimen gauge lengths after testing which failed to reveal any well developed pits.

The excellent mechanical properties of the as-rolled 927 are also thought to contribute to the difficulty in the initiation and propagation of SCC cracks in the material. The as-rolled 927 exhibits TL-charpy impact values of 60-80J at 20°C[9]. Thomas et al[10] when investigating a martensitic material with a similarly fine grain size and microstructure of martensite with thin films of interlath retained austenite, attributed the good impact properties to the latter. The inhibiting effect of small grain size on SCC initiation and propagation by virtue of its effect on deformation properties is outlined in the literature review. It is not possible to ascertain the extent of the influence of this thin layer of interlath retained austenite on the mechanical and/or electrochemical processes at the tip of an advancing SCC microcrack, but it is likely to lead to

electrochemical processes at the tip of an advancing SCC microcrack, but it is likely to lead to crack energy consumption as witnessed by its effect on the impact properties.

A co-worker[128] conducting SCC tests on 927 utilising the rising load technique with fatigue pre-cracked compact tension specimens also reports difficulty in initiating SCC. The plain strain fracture toughness (K_{IC}) is reported as 142 MPa√m and K_{ISCC} in 1000ppm chloride and 1000ppm sulphate at free corrosion potential as 28.21 MPa√m and 31.25 MPa√m respectively. SCC was initiated with difficulty at the tip of a fatigue pre-crack in these two solutions which implies that initiation from a smooth surface or a blunt pit is highly unlikely. The SCC fracture morphology obtained is described as mixed trans and intergranular. Parkins[24] demonstrates that for a maraging steel exposed to a chloride environment EAC is promoted in pre-cracked specimens by solutions not amenable to initiation of cracking in plain tensile SSR test specimens. Parkins goes on to suggest that such a result may be indicative of the importance of stress concentration in cracking, although the fact that initially plain specimens can be stressed beyond the UTS without SCC seems to suggest otherwise. In that case the precracks are thought to be important in relation to environmental effects such as changes in pH, oxygen concentration or potential variations within the crack enclave.

6.1.2 Impressed Potential Testing

The existence of bath tub shaped curve of SCC severity vs applied potential extending over the range of SCC susceptibility has been demonstrated for many systems[129-131]. Much published literature indicates that this potential range of SCC susceptibility, if it exists, is only of the order of a few hundred millivolts in most systems[28]. All impressed potentials other than for the extreme cathodic potential of -1200mV were selected from the fast and slow scans of Figure 5.12 in accordance with the method outlined by Parkins[119]. The results of these tests as a function of impressed potential are presented graphically in Figure 6.1 with the SCC severity expressed in terms of the time to failure index (TTF). Examination of Figure 6.1 reveals a sharp decrease in TTF with polarization above 0mV and a steady decrease in properties with polarization in the active direction.

Polarization at -480mV (strained Ecorr), -325mV (point of maximum separation between fast and slow scans in the cathodic region) and 0mV (point of maximum separation of curves in the anodic region) failed to produce any sign of embrittlement. The fracture surfaces of all three specimens displayed well developed cup and cone failure comparable with the air tests. In the case of the -325mV and -480mV tests it appears that insufficient hydrogen is generated by the corrosion processes at these potentials to be able to cause embrittlement or initiate cracking from the smooth surfaces of the test specimens. Examination after completion of the tests revealed the

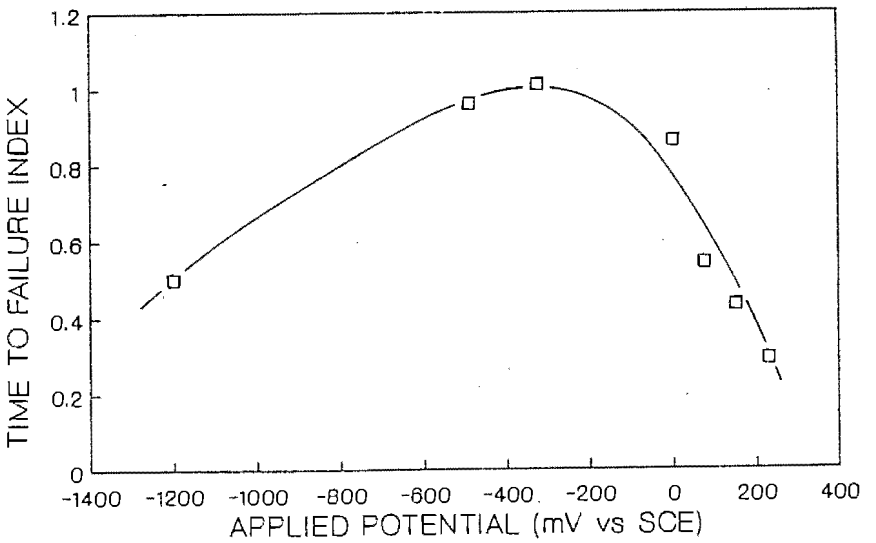

Figure 6.1: SCC susceptibility of 927 as a function of impressed potential as measured by the time to failure index (TTF).

specimen gauge lengths to be free of pits or any visible corrosion films. On completion ofthe SSR test on the anodically polarised 0mV test, the entire gauge length was observed to be pit free and covered with a reddish-brown, strongly adherent oxide film. Again the lack of SCC in this test is thought to be related to the inability to initiate SCC on the smooth specimen surfaces over the relatively short duration of the SSR tests. This material is sufficiently corrosion resistant at this potential to avoid localised break down of the oxide film as shown by Figure 5.10, the surface undergoing a more general corrosion.

Polarisation in the anodic range of 75-150mV yielded interesting results. Table 5.1 in conjunction with the various indices of Table 5.2 imply an associated increase in SCC susceptibility over this potential range. These deductions were partially supported by the SEM fractography which revealed that the fractures were largely the product of large corrosion pits which reduced the load bearing cross-section of the specimens, resulting in ductile overload of the remaining cross-section. As might be anticipated, the more noble potential of 150mV resulted in a higher proportion of pitting on the fracture surface than at 75mV as a result of the increased anodic activity. In both instances the pitted area of the specimen fracture surface was clearly discernible by a striated morphology as illustrated in Figures 5.15(b) and 5.16(b).

These striations are further illustrated in Figure 6.2. The striations are reasoned to be corrosion related as they do not feature on the fracture surfaces of the specimens that were polarised at potentials lower than or equal to 0mV (-480mV is the Ecorr during straining). All these specimens exhibited fully ductile, dimpled fracture morphologies. These striations also featured prominently on the specimen tested at 230mV (Figure 5.14). The fast and slow potentiodynamic curves of Figure 5.12 predict film instability above 0mV under straining conditions at crack tips.

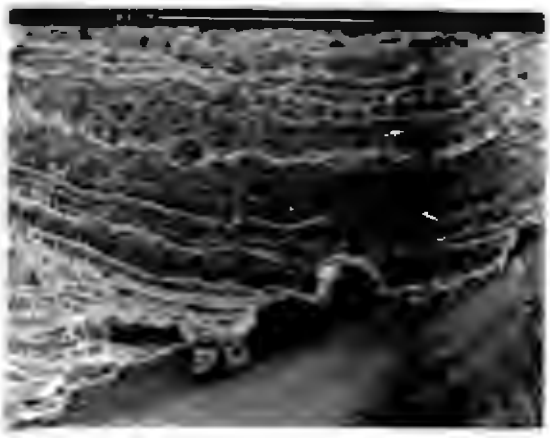

(a)

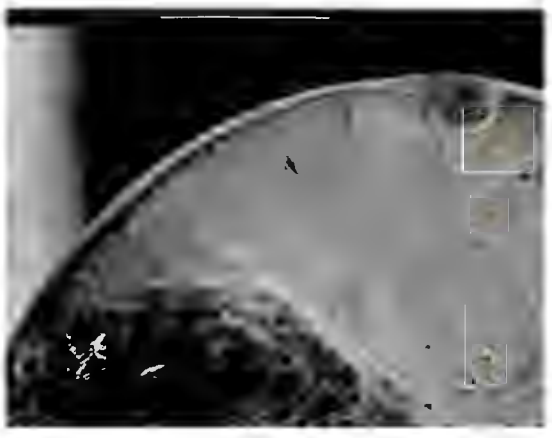

(b)

(c)

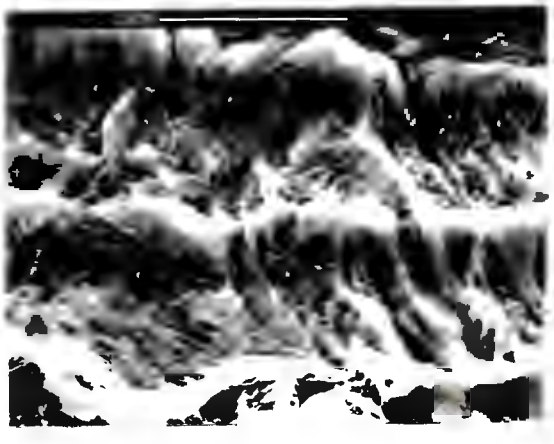

(d)

Figure 6.2: The striated pit surfaces; (a) - the striations on the specimen tested at +75mV; (b) - the fracture surface of the specimen tested at +150mV. Notice the consistency of the orientation of the striations in the two independent dissolution (pitting) events; (c) - striations parallel to the gauge length on the specimen tested at +150mV; (d) - high magnification of the striations in the +230mV specimen.

It is also noticed (Figure 6.2(b)) that irrespective of the point of origin of the pits, the striations assume the same orientation on the specimen surface. It is difficult to imagine crack or pit fronts originating at different points on the circumference of the specimen gauge and propagating with exactly the same orientations over such extensive distances. The separation between these striations is approximately 6μm as shown in Figure 6.2(d) and appears to be largely unaffected by pit or crack depth. One would have expected, if these were arrest markings, the separation to increase with increasing crack size or stress intensity. The latter observations point to these striations as being a microstructural effect on the anodic dissolution process at high anodic overpotentials as opposed to some macro "slip-dissolution" or discontinuous type crack or pit propagation mechanism. This conclusion is reinforced by Figure 6.2(c) which shows a pit on the gauge length of the specimen tested at 150mV. The striations are parallel to the gauge length (direction of principle stress) and are thus not related to the pit or crack propagation perpendicular to the gauge length.

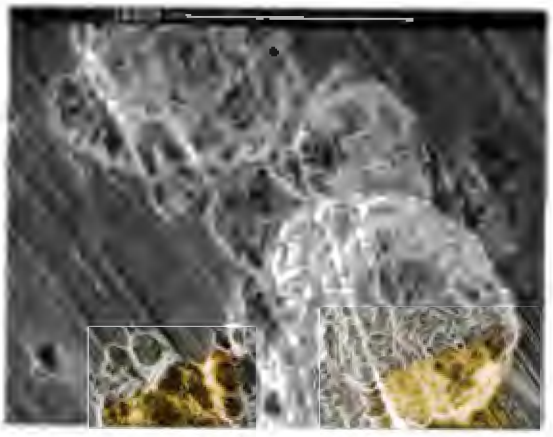

Figure 6.3: The striated corrosion morphology of the pit surfaces obtained after anodic polarisation to 200mV under conditions of zero dynamic strain i.e. stress free.

An experiment to verify the absence of a stress (or dynamic strain) contribution to the striated corrosion morphology was conducted. This involved the removal of an undeformed section (below the shoulder) of the specimen tested at +150mV and its immersion for a period of time in the simulated mine water at an impressed potential of +200mV. SEM examination of the resulting corrosion pits (Figure 6.3) revealed an identical striated corrosion morphology to that obtained during SSR testing at similar impressed anodic potentials. A comparison of the orientation of the

striations on the two specimens (strained and unstrained) relative to a previously marked datum line revealed them to be identical.

The determination of the orientation of these striations relative to the rolling direction was not possible due to the symmetrical (cylindrical) cross-section ot the SSR tensile specimens (specimens were machined with the gauge length in the rolling direction). Cross-section metallography was also unsuccessful in resolving the problem owing to the cleanliness of the steel microstructure and the equiaxed prior austenite grain morphology resulting from the high finish rolling temperature (1250°C). However, the straightness, extent and consistency of the orientation of the striations indicate it to be the product of a microstructural condition induced by the hot rolling process.

The origin of the striated corrosion morphology is explained in terms of the hot rolling procedure giving rise to microchemical partioning of alloying elements. The rolling results in the elongation of these alloy partitions into macroscopically linear morphologies or bands. The anodic polarisation results in the accelerated dissolution of the less noble linear distributions resulting in series of parallel tunnels. The existence of these corrosion tunnels was confirmed by cross-section metallography carried out on several of the partially propagated pits on the specimen gauge lengths. It is not clear as to whether the remaining ligaments (tunnel walls) of more noble material eventually corrode through or undergo ductile failure as a result of the increasing stress during SSR testing. The absence of ductile voids or necking in these areas as shown in Figure 6.2(d) seems to indicate the former. This hypothesis will, however, have to be verified using EDAX or some other chemical analytical technique.

Higher magnification revealed the existence of lower energy transgranular and intergranular fracture features at the bases of these striated pitted areas (Figures 5.15 and 5.16). The intergranular fracture areas exhibit numerous dimples and tear ridges. The transgranular fracture facets closely resemble those derived at -1200mV owing to hydrogen embrittlement viz. interlath fracture. Examination of the gauge lengths after testing revealed the existence of numerous small pits on the specimen tested at 150mV and only one other well developed pit on that tested at 75mV. This might be anticipated upon examination of the potentiodynamic polarization curve of Figure 5.12. The material is thus more vulnerable to localised corrosion and hence SCC initiation at this more noble potential.

This manifestation of EAC at the base of these well developed pits supports the hypothesis that the resistance of the material to SCC under the conditions of the test is linked to the difficulty in initiating SCC on the smooth specimen surface. It appears that the development of these large pits provided the necessary occluded cell at the base with the associated changes in pH, oxygen concentration etc. resulting in the localised EAC of the metal. The fast-slow potentiodynamic scan

of Figure 5.12 indicates the electrochemical likelihood of SCC over this potential range of 0 - 200mV, provided initiation is accomplished within the time frame of the test.

The initiation of SCC at the base of the pit may be for mechanical as opposed to electrochemical reasons. The dependence of SCC upon strain rate displays the typical bath-tub shape. It is possible that the macro strain rate employed during testing is outside the critical strain rate for SCC and the development of a pit with the associated increase in stress concentration at the base resulted in a localised strain rate falling into the regime for SCC. This critical strain rate coupled with the development of the SCC conducive electrochemical conditions at the base of the pit then resulted in localised SCC cracking. However, this hypothesis will have to be confirmed by SSR testing at various applied strain rates.

A test conducted at +230mV resulted in almost complete dissolution of the specimen, the specimen failing by ductile overload as a result of section reduction by gross pitting. It is evident from the results of the test that the anodic dissolution rate at this potential is far too great to sustain the delicate balance of film formation/film rupture that is essential for SCC. This example illustrates the necessity of verifying the role of SCC in the reduction of the mechanical properties as may be indicated by the stress-strain curve or the SCC indices.

6.1.3 Mechanistic Arguments

It is clear that accelerated cracking and gross reduction of mechanical properties at the cathodic potential of -1200mV can only be attributed to hydrogen assisted cracking. The mixed fracture mode is an indication that both prior austenite grain boundaries and interlath boundaries are acting as strong hydrogen traps and thereby facilitating decohesion at these locations.

Phelps[132] pointed out that the effect of electrochemical polarisation on the time to failure could provide a diagnostic criterion showing whether failure is due to hydrogen embrittlement or active path corrosion. Thus if SCC is caused by localized corrosion along an active path through the steel, the application of a cathodic current would be expected to suppress the corrosion reaction and result in longer time to failure, while the application of an anodic current would be expected to increase the amount of corrosion. However, if hydrogen generated by general corrosion is the cause of SCC, the application of a cathodic current would be expected to generate more hydrogen and shorten the time to failure. Parkins[38] logically points out that at intermediate potentials for both systems ambiguity exists as to which mechanism of crack growth is operative and it is quite possible that both hydrogen induced and dissolution controlled cracking can occur in these circumstances.

The graph of TTF vs applied potential of Figure 6.1 shows that at extreme cathodic potentials (-1200mV) hydrogen embrittlement is prevalent. The SCC indices improve with increasing polarisation in the active direction upto -100mV. As mentioned previously, this trend is indicative of HAC rather than an active path SCC mechanism over this potential range. The decrease in TTF with a further increase in potential is the result of a reduction in specimen cross-section owing to large scale pitting rather than an active path SCC mechanism. However, the predominantly intergranular fracture at the base of the pit is thought to be due to hydrogen embrittlement, the source of hydrogen provided by hydrolysis and anodic reactions in this occluded cell arrangement. Raising the potential in order to stimulate anodic dissolution can decrease the pH at the crack tip so that a decrease in the time to failure under these conditions may be diagnostic of hydrogen embrittlement rather than active path cracking[57]. It is well known that the specifity to environment of a material that suffers from some form of hydrogen embrittlement eg. high strength steels, is far less than those which suffer from anodic dissolution mechanism. The predominance of intergranular cracking at the base of pits at anodic potentials and the absence of the transgranular mode displayed at extreme cathodic potentials is reasoned in terms of the prior austenite grain boundaries acting as stronger hydrogen traps than lath boundaries. At anodic potentials the hydrogen available at crack tips is less than at cathodic potentials and the prior austenite grain bounderies are preferentially embrittled, not sufficient hydrogen being available for gross embrittlement of the lath boundaries.

6.2 TEMPERED MATERIAL

6.2.1 Air Tests

The tempering treatment (1 hour at 700°C) has resulted in a marked reduction in U.T.S. (1500MPa to 800MPa); the reduction in area and percentage elongation remaining virtually unchanged. The temper curve established by Grobler et al[86] is illustrated in Figure 6.4. The curve shows that secondary hardening occurs at about 500°C after which the hardness and associated mechanical properties drop off rapidly with further increases in tempering temperature.

The fracture surfaces exhibit evidence of reduced ductility with a star-like morphology displaying numerous radial secondary cracks as shown by Figure 5.3. Higher magnification however, reveals that the fracture mode is fully ductile and predominantly transgranular with reduced dimple size. These microvoids are thought to have nucleated on the lath precipitates (produced by the tempering process) thus producing the range of microvoid diameters observed.

The reduction in mechanical properties and the resultant fracture morphology are the products of temper embrittlement (TE) and tempered martensite embrittlement (TME). TE is intergranular with respect to prior austenite grain boundaries and it usually occurs by the segregation of residual

impurities such as phosphorous to prior austenite grain boundaries in what are otherwise relatively stable microstructures[100,101]. TME is transgranular and occurs when the thin layers of interlath retained austenite become unstable following tempering and decompose into interlath cementite

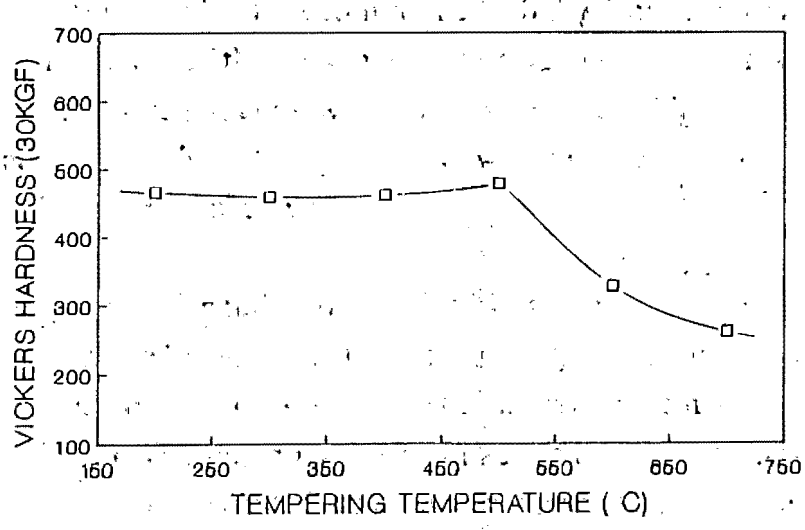

Figure 6.4: The temper curve for 927[86].

with a resulting reduction in mechanical properties[117]. The molybdenum content has the effect of temper resistance and may account for the postponent of TE and TME to the 600-700°C range in 927. The fractographs presented by Hippsley and Haworth for a 9Cr-1Mo steel tempered at 750°C for 1 hour are strikingly similar to those obtained in this investigation for 927 tempered at 700°C for 1 hour. Wall and co-workers[133] identified the main precipitates present in this 9Cr-1Mo alloy under the same tempering conditions as used in this investigation viz. 1 hour at 700°C, as $M_{23}C_6$ carbides on the grain and lath boundaries. The grain boundaries were found to be more densely populated. The authors attributed the brittle fracture morphology to these grain and lath boundary carbide precipitates in conjuntion with segregated impurity atoms. The same reasoning is believed to apply to the brittle fracture behaviour of the tempered 927.

6.2.2 Effect of Aqueous Environments

The various ionic solutions failed to induce any further reduction in mechanical properties up and above that induced by the tempering process as illustrated by Figure 5.21 and Table 5.1. Again this lack of SCC is attributed to the difficulty in initiating SCC on these smooth specimen surfaces owing to the resistance to pitting under the test conditions. Examination of the gauge lengths after testing failed to reveal the existence of any corrosion pits.

Grobler et al[86] using salt-spray and potentiodynamic testing in simulated mild and aggressive mine waters on tempered 927 material established that tempering above 600°C for 1 hour resulted in a marked reduction in corrosion resistance. The results of extensive electron microscope studies

6.3 WELDED AND PWHT 927 IN AQUEOUS ENVIRONMENTS

As previously mentioned the test specimens were prepared across the 30°V butt weld with the weld line and associated HAZ in the gauge length. The 309L electrodes were presumably selected on account of the ability of the soft, ductile austenitic weld metal to absorb most of the welding stresses by plastic deformation and thereby reduce the residual stress in the joint. This will naturally assist in reducing suseptibility to SCC. The low carbon grade was selected to avoid sensitisation in the HAZ. Plotting of the 927 and the 309 electrode compositions on the Schaeffler diagram and assuming a 50% dilution for a V joint yields a fully austenitic weld metal structure.

The test results for the as welded and the PWHT specimens of Figures 5.24 and 5.27 respectively both indicate an absence of EAC. Table 5.2 reflects this lack of EAC quantitatively. This absence of EAC was confirmed fractographically with all the specimens exibiting fully ductile, dimpled fracture surfaces with well developed shear lips as shown by Figures 5.25 and 5.28. Cross-section metallography revealed that the majority of plastic strain during testing and all the fractures were restricted to the lower strength, ductile austenitic weld metal. The mechanical properties measured during SSR testing viz. UTS, reduction in area etc. correspond to that for AISI 309. As might be expected, the PWHT material exhibited reduced yield and tensile strengths and increased elongation in comparison with the as-welded material.

The restriction of the majority of the dynamic straining to the softer 309 weld metal resulted in these SSR tests being essentially a SCC test on the weld metal. The ductile and highly corrosion resistant austenitic weld metal appears to be immune to SCC under the test conditions and in the solutions used. It was initially anticipated that the less corrosion resistant HAZ would be susceptible to SCC via an active path dissolution mechanism. Grobler et al[86] reported that salt spray and immersion corrosion testing in simulated minewater on specimens prepared from welds produced localised attack in the HAZ. TEM studies showed that the increase in susceptibility was associated with chromium rich $M_{23}C_6$ carbide precipitation. The PWHT of 1 hour at 1050°C followed by an air quench was reasoned to eliminate this sensitisation in the HAZ.

It appears that the relatively short SSR test duration (20-34 hours) resulted in the absence of preferential corrosion attack in the HAZ. Examination of the gauge lengths upon completion of SSR tests showed them to be pit free. In retrospect, it would have been beneficial to have precracked the material in the area of interest viz. the HAZ in order to have concentrated the dynamic strain in this region. This practice would have yielded a more accurate estimation of the susceptibility of the HAZ to SCC.

CHAPTER 7

FINDINGS AND CONCLUSIONS

1. The good dry abrasion resistance exibited by alloy 927 is credited to the favourable combination of strength and toughness imparted to the alloy by its micro-duplex microstructure of low carbon lath martensite and thin layer of retained austenite.

2. The highly favourable abrasion-corrosion properties are attributed to the good corrosion resistance imparted to the alloy by the chromium, nickel and molybdenum additions acting in combination with the good abrasion resistance of the material. The alloy is seen to develop a particularly mechanically robust and chemically stable oxide film relative to other similar alloys in the simulated mine water solution. This is considered to be a strong contributor to the good abrasion-corrosion performance of the alloy.

3. The production variables of plate thickness and prior cold working exert negligible influence on the mechanical and corrosion properties of the material and hence on abrasion-corrosion performance.

4. The alloy 927 in the as-rolled condition exhibits good corrosion properties with a well defined passive potential range in all the solutions used in the investigation. The 1000ppm sulphate and 500ppm nitrate solutions exert a strong passivating influence, extending the passive potential range over 1200mV. The 1000ppm chloride solution is the most aggressive (passive potential range is 260mV) while the simulated mine water results in an intermediate passive potential range of 560mV.

5. The free corrosion potential recorded during straining for all the materials is more active than that derived under strain free conditions. This is a result of the continuous rupture of the protective oxide film and the exposure of fresh metal during straining.

6. Tempering at 700°C for 1 hour has resulted in the sensitisation of the microstructure with the attendant reductions in the passive potential ranges recorded during polarisation scans and the free corrosion potential recorded during straining.

7. The as-rolled 927 is immune to SCC at open circuit potential under the conditions of the test and in all the solutions. This apparent immunity is strongly linked to the difficulty in initiating SCC on the smooth plain specimen surfaces.

8. The high strength as-rolled 927 is highly susceptible to hydrogen embrittlement at extreme cathodic potentials. The hydrogen assisted cracking propagates in a predominantly interganular mode along prior austenite grain boundaries.

9. 927 in the as-rolled condition is immune to SCC at impressed potentials in the potential range of -500 to 0mV under the test conditions. This is again related to the difficulty in initiating SCC on the smooth specimen surface over the relatively short test durations.

10. SSR testing at +75mV and 150mV results in pitting of the material. Localised mixed transgranular fracture and intergranular separation are seen to occur at the base of the pits as a result of the development of the occluded conditions necessary for EAC within the pit confines. This occurrence is cited as evidence of EAC initiation difficulty on the smooth specimen surfaces.

11. At potentials at and above 230mV, the rate of anodic dissolution is too great to sustain the delicate balance of film and film free conditions necessary for EAC.

12. At anodic potentials of 75mV and above a lineated morphology is seen to develop on corrosion (pit) surfaces. This is believed to be a microstructural effect introduced during the rolling process on account of the straightness, extent and preferred orientation of these striations.

13. The tempered material is immune to EAC at free corrosion potential under the test conditions. This is also attributed to the difficulty in initiating SCC over the relatively short test durations.

14. The slow strain rate technique using smooth tensile specimens is not suitable for testing the material welded with 309 electrodes as the dynamic strain is concentrated in the softer austenitic weld metal and not in the area of interest viz. the HAZ.

REFERENCES

1. Allen, C, Prothroe, B.E. and Ball, A, J.S. Afr. Inst. Min. Metall., Oct 1981, pp. 289-302.

2. Metcalfe B, Whitaker W.M. and Lenel U.R., Stainless Steels 87, Institute of Metals, 1988, pp. 300-306.

3. Prothroe, B.E., Ball A and Heathcock C.J., Speciality Steels and Hard Materials, Eds N.R. Comins and JB Clark, Oxford: Permagon Press 1983, pp. 289-298.

4. Lenel U.R. and Knott B.R., Metall. Trans., 1987, 18A, pp. 767-775.

5. Allen C, Prothroe B.E., Ball A, Wear, 1981-1982, Vol 74, pp. 287-305.

6. Roa, B.V.N. and Thomas G, Metall. Trans., 1980, 11A, pp. 441-453-453.

7. Bee, J.V., J. S. Afr. Ins. Min. Metall., Vol 87, No 1, 1987, pp. 1-6.

8. Allen C, Ball A and Noël, R.E.J., Johannesburg, 1984, Middeburg Steel and Alloy (Pty) Ltd, pp. 433-453.

9. Grobler, P.E. and Mostert R.J., Wear of Materials 1989, Ed K.C. Ludema, ASME, 1989, pp. 289-295.

10. Sarikaya, M, Steinberg, B.G. and Thomas, G, Metall. Trans., Vol 13A, Dec 1982, pp. 2227-2237.

11. Kwok, C.K. and Thomas G, Wear of Materials 1983, Ed KC Ludema, ASME, 1983, pp. 140-147.

12. Salesby, W.J. and Thomas G, Wear, Vol. 75, 1982, pp. 21-40.

13. Barker, K.C., The development of abrasive-corrosive wear resistance of steels by microstructural control, PhD Thesis, University of Cape Town, February 1988.

14. Allen, C, Prothroe, B.E. and Ball A, J.S. Afr. Inst. Min. Metall., 1981, Vol. 10, pp. 289-297.

15. Zum-Gahr, K.H., Wear, Vol. 74, pp. 353-373.

16. Honeycombe, R.W.K., Steels - metallurgy and microstructure, Edward Arnold, London.

17. Ball, A,, Wear, Vol. 91, pp. 201-207.

18. Hubackova, J, Cehal, V and Mazanec K, Br. Corros. J., Vol. 19, No. 2, 1984, pp. 77-81.

19. Barker, K.C. and Ball A, Br. Corros. J., 1989, Vol. 24, No. 3, pp. 222-228.

20. Mutton, P.J.and Watson, J.D., Wear, 1978, Vol. 48, pp. 385-398.

21. Sprowls, D.O., in Metals Handbook, Ninth Edition, Volume 8, Mechanical Testing, ASM, pp. 495 - 536.

22. Heheman, R.F., Met. Trans. A, Vol. 16A, November 1985, pp. 1909 - 1923.

23. Brown, B.F., Corrosion, Vol. 26, No. 8, August 1970, pp. 249 - 250.

24. Parkins, R.N., Mat. Sci. and Tech., June 1985, Vol. 1, pp. 480-486.

25. Carter, C.S., Corrosion, Vol. 27, No 11, November 1971, pp. 471-477.

26. Newman, R.C. and Procter, R.P.M., Br. Corros. J., 1990, Vol. 25, No. 4, pp. 259-269.

27. Bursle, A.J. and Pugh, E.N., in Environment sensitive fracture of engineering materials, Foroulis, Z.A., Ed., Met. Soc. AIME, New York, 1979, pp.18-47.

28. Parkins, R.N., Br. Corros. J., 1979, Vol. 14, No. 1, pp. 5-14.

29. Stress Corrosion Cracking - The Slow Strain Rate Technique, ASTM STP 665, Ugianski, G.M. and Payer Eds., 1979.

30. Parkins, R.N., Corrosion, Vol. 46, No. 3, March 1990, pp. 178 - 189.

31. Evans, J.T. and Parkins, R.N., Acta Metall., 1976, p. 5.

32. Holroyd, N.J.H. and Hardie, D., Corros. Sci., 1983, Vol. 23, p. 527.

33. Jones, D.A., Met. Trans. A., Vol. 16A, June 1985, pp. 1133 - 1141.

34. Parkins, R.A., Corrosion Science, Vol. 20, 1980. pp. 147 - 166.

35. Staehle, R.W., in Mechanisms of Environment Sensitive Cracking of Materials, Swann et al Eds., Metal Society, London, 1977, pp. 574 - 602

36. Staehle, R.W., The Theory of Stress Corrosion Cracking, p. 223, NATO, Brussels, 1971.

37. Chu, H.C. and Wei, R.P., Corrosion, Vol. 46, No. 6, June 1990, pp. 468 - 476.

38. Parkins, R.N. and Craig, I.H., in Mechanisms of environmental sensitive cracking of materials, The Metals Soc., London, 1977, pp.32 - 52.

39. Hoar, T.P., and West, J.M., Proc. R. Soc., Vol. A268, 1962, p. 304.

40. Hoar, T.P., in Fundamental aspects of stress corrosion cracking, 1969, Houston, TX, NACE. Staehle, R.W., Forty, A.J. and van Rooyen, D., Eds.

41. Turnbull, A., Corrosion Science, Vol. 23, No. 8, 1983, pp. 833 - 870.

42. Parkins, R.N., J. of Strain Analysis, Vol. 10, No. 4, 1975, pp. 251 - 258.

43. Vermilyea, D.A. and Tedmon, C.S., J. Electrochem. Soc., Vol. 117, 1970, p. 437.

44. Doig, P. and Flewitt, P.E.J., Met. Trans. A, 9A, 1978, p. 387.

45. Karlberg, G. and Wranglen, G., Corrosion Science, Vol. 11, 1971, pp. 499 - 510.

46. France, W.D. and Wranglen, G., Corrosion Science, Vol. 11, 1971, pp. 499 - 510.

47. Alavi, A. and Cottis, R.A., Corrosion Science, Vol. 27, 1987, No. 5, pp. 443-451.

48. Turnbull, A., in Embrittlement by the Localized Crack Environment, Ed. Gangloff, R.P., Metallurgical Society of AIME, 1984, pp. 3 - 31.

49. Brown, B.F., in The Theory of Stress Corrosion Cracking in Alloys, NATO, Brussels, 1971, p. 167.

50. Turnbull, A., Corrosion Sci., 1987, Vol. 27, p. 1323.

51. Sedriks, A.J., Slattery, P.W. and Pugh, E.N., in Fundamental aspects of stress corrosion cracking, 1960, Houston, TX, NACE, Staehle, R.W., Forty, A.J. and van Rooyen, D., Eds.

52. Ateya, B.G. and Pickering, H.W., in Hydrogen in Metals, ASM, Metals Park, U.S.A., 1974, p.207.

53. Kowaka, M., Metal corrosion damage and protection technology, 1990, Allerton Press Inc., pp.347-440.

54. Alavi, A. and Cottis, R.A., in Embrittlement by the localized crack environment [Proc. conf.], Philadelphia, Pa. USA, 4-5 Oct, 1983, Metallurgical Soc/AIME.

55. Fessler, R.R., Markworth, A.J. and Parkins, R.N., Corrosion, Vol. 39. No 1, 1983, pp. 20 - 35.

56. Copson, H.R., in Physical metallurgy of stress corrosion fracture, Rhodin, T.N., Ed., 1959, New York, Interscience.

57. Shreir, Vol. 1, Metal Environment Reactions, Second Edition, Chapter 8, p. 8.1

58. Moriya, S., Matsui H and Kimura, H, Mater. Sci. Eng., 1979, Vol. 40, p. 217.

59. Snape, E., Corrosion, Vol. 24, 1968, p. 261.

60. Sandoz, G., Met. Trans., Vol. 3, 1972, p. 1169.

61. Bade, J and Dodd, R.A., in Fundamental aspects of stress corrosion cracking, 1969, Houston, TX, NACE.Staehle, R.W., Forty, A.J. and van Rooyen, D., Eds.

62. Harrison, R.P., Jones, D.G. and Newman, J.F., in Stress corrosion cracking and hydrogen embrittlement of iron base alloys, 1977, Houston, TX., Staehle, R.W., Hochman, J., McCright,R.D. and Slater, J.E., Eds.

63. Parkins, R.N., Slattery, P.W. and Poulson, B.S., Corrosion, 1981, Vol. 37, p.650.

64. Burns, D.S., Materials Performance, Vol. 15, 1976, p. 21.

65. Smith, G.C., in Hydrogen in Metals, ASM, Metals Park, 1974, p. 485.

66. Paes de Oliveria, C., Aucouturier, M. and Lacombe, P., Corrosion, Vol. 36, 1980, pp. 53 - 59.

67. Asoaka, T. Lapasset, G., Aucouturier, M and Lacombe, P., Corrosion, Vol. 34, 1978, pp. 39 - 47.

68. Bernstein, I.M. and Thompson, A.W., in Mechanisms of Environment Sensitive Cracking of Materials, Swann et al Eds., Metals Society, London, 1977, pp. 412 - 425.

69. Thompson, A.W., in Environment Sensitive Fracture of Engineering Materials, Foroulis Ed., Metallurgical Society of AIME, 1979, pp. 379 - 410.

70. Proctor, R.P.M. and Paxton, H.W., Trans. Am. Soc., Vol. 62, 1969, p. 989.

71. Lynch, S.P., Metallography, Vol. 23, 1989, pp. 147 - 171.

72. Lynch, S.P., Acta Met., Vol. 36, No. 10, 1988, pp. 2639 - 2661.

73. Beachem. C.D., Metall. Trans., Vol. 3, 1972, p.437.

74. Liu, R., Narita, N., Altstetter, C., Birnbaum, H.K. and Pugh, E.N., Metall. Trans., 1980, Vol. 11A, p.1563.

75. Meletis, E.I. and Hochman, R.F., Corros. Sci., 1984, Vol. 24, p.843.

76. Pugh, E.N., Corrosion, 1985, Vol. 41, p.517

77. Speidel, M.O., Corrosion, 1977 Vol. 33, p.199.

78. West, J.M., Met. Sci. J.,1973, Vol. 7, p.169

79. Dix, E.H., Trans. Amer. Inst. Min. Met. Engrs., Vol. 137, 1940, p. 11.

80. Silverman, D.C., Corrosion, Vol. 39, No. 12, December 1983, pp. 488 - 490.

81. Jones, D.A., Met. Trans. A, Vol. 16A, June 1985, pp. 1133 - 1141.

82. Bursle, A.J. and Pugh, E.N., in Mechanisms of Environment Sensitive Cracking of Materials, The Metals Soc., London, 1977, pp. 471 - 481.

83. Rath, B.B. and Bernstein, I.M., Met. Trans., 1971, Vol. 2, pp. 373.

84. Pickering, H.W. and Swann, P.R., Corrosion, 1963, Vol. 19, p. 373.

85. Sieradski, K and Newman, R.C., J. Phys. Chem. Solids, Vol. 48, No. 11, 1987, pp. 1101 - 1113.

86. Hirth, J.P., in Hydrogen Embrittlement and Stress Corrosion Cracking, Eds. Gibala, R. and Heheman, R.E., ASM, pp. 29 - 41.

87. Beachem. C.D., Metall. Trans., Vol. 3, 1972, p.437.

88. Thompson, A.W. and Bernstein, I.M., Adv. Corrosion Sci. Tech., Vol. 7, 1973, p. 169.

89. Zapffe, C and Sims, C, Trans. AIME, Vol. 145, 1962, p. 775.

90. Tetelman, A.S. and Robertson, W.D., Trans. AIME, Vol. 224, 1962, p. 775.

91. Kerns, G.E. and Staehle, R.W., Scripta Met., Vol. 6, 1972, p. 631.

92. Morlet, J.G., Johnson, H.H. and Troiano, A.R., J. Iron Steel Inst., Vol 189, 1958, p. 37.

93. Oriani, R.A. and Josephic, P.H., Acta Met., Vol. 22, 1974, p. 1065.

94. Tetelman, A.S., in Fund. Aspects of Stress Corr. Cracking, NACE, Houston, 1969, p. 446.

95. Beachem, C., in Stress Corrosion Cracking and Hydrogen Embrittlement of Iron Base Alloys, NACE, Houston, TX, 1977, p. 326.

96. Failure Analysis and Prevention, Volume 11, Metals Handbook, Ninth Edition, A.S.M.

97. Carter, C.S., Corrosion, Vol. 27, No. 11, November, 1971, pp. 471 - 477.

98. Chu, H.C. and Wei, R.P., Corrosion, Vol. 46, No. 6, June 1990, pp.468-476.

99. Barth, C.F., Steigerwald, E.A. and Troiano, A.R., Corrosion, Vol. 25, No 1, September, 1969, pp. 353 - 358.

100 Briant, C.L. and Banerji, S.K., Int. Met. Rev., 1978, Vol. 23, No. 4, p. 164.

101 McMahon, C.J., Mat. Sci. Eng., 1976, Vol 25, p. 233.

102 Thomas, C.J., Edyvean, R.G.J., Brook, R and Ferguson, W.G., Mat. Sci. Eng., Vol. 78, 1986, pp. 55 - 63.

103 Yoshino, K and McMahon, C.J., Metall. Trans., 1974, Vol. 5A, p. 363.

104 Bandyopadhyay, N, Kameda, J and McMahon, C.J., Metall. Trans., 1983, Vol. 14A, p.7.

105 Hippsley, C.A., Mater. Sci. Technol., 1987, Vol. 3, pp. 912 - 922.

106 Laurent, J.P., Lapasset, G., Aucouturier, M. and Lacombe, P., in Hydrogen in Metals, Eds. Bernstein, I.M. and Thompson, A.W., 1974, Metals Park, ASM, p. 559.

107. Latanision, R.M. and Opperhauser, H., Metall. Trans., 1975, Vol 6A, p. 223.

108. Briant, C.L., Feng, H.C. and McMahon, C.J., Metall. Trans., Vol. 9A, 1978, p. 625.

109. Truman, J.E., Perry, R. and Chapman, G,N., J. of Iron and Steel Institute, Sept. 1964, pp. 745 - 756.

110. Lynch, S.P., Acta Metall., Vol. 32, No. 1, 1984, pp. 79 - 90.

111. Parkins, R,N., Mazza, F., Royuela, J.J. and Scully, J.C., Br. Corros. J., Vol. 7, July, 1972, pp. 154 - 167.

112. Parkins, R.N., in Stress Corrosion Cracking - The Slow Strain-Rate Technique, ASTM STP 665, G.M. Ugianski and J.H. Payer, Eds.,American Society for Testing and Materials, 1979, pp. 5 - 25.

113. Kim, C.D. and Wilde, B.E., in Stress Corrosion Cracking - The Slow Strain-Rate Technique, ASTM STP 665, G.M. Ugianski and J.H. Payer, Eds., ASTM, 1979, pp. 97 - 112.

114. Scully, J.C., in Mechanisms of environment sensitive cracking of materials, the Metals Soc., London, 1977, pp.1-18.

115. Buhl, H., in Stress Corrosion Cracking - The Slow Strain-Rate Technique, ASTM STP 665, G.M. Ugianski and J.H. Payer, Eds., ASTM, 1979, pp. 333 - 346.

116. Daniels, A.D., in Stress Corrosion Cracking - The Slow Strain-Rate Technique, ASTM STP 665, G.M. Ugianski and J.H. Payer, Eds., ASTM, 1979, pp.347-362.

117. Sarikaya, M., Steinberg, B.G. and Thomas, G., Met. Trans. A, Vol. 13A, Dec. 1982, pp. 2227 - 2237.

118. Capendale A.E., The influence of water composition on the pitting behaviour of a stainless steel, MSc thesis, Materials Engineering Department, University of Cape Town.

119. Parkins, R.N., Corrosion Science, Vol. 20, 1980, pp.147-166.

120. Bechet, M., MSc. Thesis Pending, Department of Materials Eng., University of Cape Town, South Africa.

121. Mom, A.J.A., Dencher, R.T., vd. Wekker, C.J. and Schultze, W.A., in Stress Corrosion Cracking - The Slow Strain-Rate Technique, ASTM STP 665, G.M. Ugianski and J.H. Payer, Eds., ASTM, 1979, pp. 305 - 319.

122. Cotterrel, M.H., Noel, R.E.J. and Allen, C., Br. Corros. J., 1990, Vol. 25, No. 1, pp.60-72.

123. Leckie, H.P. and Uhlig, H.H., J. of Electrochem. Soc., 1966, Vol. 113, p. 1262.

124. Oldfield, J.W., Lee, T.S. and Kain, R.M., in Proc. Stainless Steel 84, Chalmers University of Technology, The Institute of Metals, 1985, p. 205.

125. Sedriks, A.J., in Proc. Stainless Steel 84, Chalmers University of Technology, The Institute of Metals, 1985, p. 125.

126. Marshall, P.I. and Burstein, G.T., Corrosion Science, Vol. 24, 1984, p. 463.

127. Sprowls, D.O., in Stress Corrosion Testing, ASTM STP 425, Am. Soc. Testing Mats., 1967, pp. 292 - 301.

128. Thompson, R.S., Private Communication, MSc Student, Materials Engineering Dept., University of Cape Town, 1989.

129. Diegle, R.B. and Boyd, W.K., in Stress Corrosion Cracking - The Slow Strain-Rate Technique, ASTM STP 665, G.M. Ugianski and J.H. Payer, Eds., ASTM, 1979, pp. 26 - 46.

130. Hishida, M., Begley, J.A., McCright, R.D. and Staehle, R.W., in Stress Corrosion Cracking - The Slow Strain-Rate Technique, ASTM STP 665, G.M. Ugianski and J.H. Payer, Eds., ASTM, 1979, pp.47-60.

131. Payer, J.H., Berry, W.E. and Boyd, W.K., in Stress Corrosion Cracking - The Slow Strain -Rate Technique, ASTM STP 665, G.M. Ugianski and J.H. Payer, Eds., ASTM, 1979, pp. 61 - 77.

132. Phelps, E.H., in Proceedings of Conference on Fundamental Aspects of Stress Corrosion Cracking, NACE, 1969, p. 398.

133. Wall, M., in A Review of Thermal Ageing Effects in High Chromium Ferritic Steels, UICAEA Report R-12812, Harwell Laboratory, 1987.

134. Yoshino, Y., Corrosion, Vol. 42, No. 10, October 1986, pp. 592 - 600.

135. Hippsley, C.A. and Haworth, N.P., Mat. Sci. and Tech., Sept. 1988, Vol. 4, pp. 791 - 802.